E.O. Paton Electric Welding Institute of the National Academy of Science of Ukraine
International Association “Welding”

The Paton Welding Journal

02
2025

International Scientific-Technical and Production Journal ♦ Founded in January 2000 (12 Issues Per Year)

Address of Editorial Office
E.O. Paton Electric Welding Institute, 11 Kazymyr Malevych Str., 03150, Kyiv, Ukraine
Tel.: (38044) 205 23 90, E-mail: patonpublishinghouse@gmail.com; journal@paton.kiev.ua
https://patonpublishinghouse.com/eng/journals/tpwj

The Journal was registered by the National Council of Ukraine on Television and Radio Broadcasting on 09.05.2024, carrier identifier R30-04569. ISSN 0957-798X (Print), ISSN 3041-2293 (Online). DOI: http://dx.doi.org/10.37434/tpwj

Subscriptions, 12 issues per year:
348 Euro — annual subscription for the printed (hard copy) version, air postage and packaging included;
288 Euro — annual subscription for the electronic version (sending issues in pdf format or providing access to IP addresses).

Representative Offices of “The Paton Welding Journal”:

BRAZIL, Arc Dynamics
Address: Nova Iguacu, Rio de Janeiro, Brazil
Daniel Adolpho, Tel.: +55 21 9 6419 5703, E-mail: dadolpho@arcdynamics.com.br

BULGARIA, Bulgarian Welding Society
Address: Blvd. Asen Yordanov No.10, Sofia 1592, Bulgaria
Pavel Popgeorgiev, Tel.: +359 899 96 22 20, E-mail: office@bws-bg.org

CHINA, China-Ukraine Institute of Welding, Guangdong Academy of Sciences
Address: Room 210, No. 363 Changxing Road, Tianhe, Guangzhou, 510650, China
Zhang Yupeng, Tel.: +86-20-61086791, E-mail: patonjournal@gwi.gd.cn

POLAND, PATON EUROPE Sp. z o. o.
Address: ul. Kapitałowa 4, 35-213, Rzeszów, Poland
Anton Stepakhno, Tel.: +38067 509 95 67, E-mail: Anton.Stepakhno@paton.ua

The content of the Journal includes articles received from authors from around the world in the field of welding, cutting, cladding, soldering, brazing, coating, 3D additive technologies, electrometallurgy, material science, NDT and selectively includes translations into English of articles from the following journals, published in Ukrainian:

- «Avtomatychne Zvaryuvannya» (Automatic Welding), https://patonpublishinghouse.com/eng/journals/as;
- «Suchasna Elektrometalurhiya» (Electrometallurgy Today), https://patonpublishinghouse.com/eng/journals/sem;
- «Tekhnichna Diahnostyka ta Neruinivnyi Kontrol» (Technical Diagnostics & Nondestructive Testing), https://patonpublishinghouse.com/eng/journals/tdnk.

CONTENTS

ORIGINAL ARTICLES

S.V. Adjamskiy, G.A. Kononenko, R.V. Podolskyi, O.A. Safronova
STUDY OF THE INFLUENCE OF ROUGHNESS ON THE MECHANICAL PROPERTIES OF STAINLESS STEEL SAMPLES MADE BY THE LPBF TECHNOLOGY* 3

N.V. Piskun, O.R. Bulatsev, V.A. Kryukov, Zeng Ruchuan, Ye.H. Ternovy
WORKPLACE OF A COSMONAUT-WELDER FOR WELDING OF OBJECTS ON THE SURFACE OF THE MOON* 8

S.V. Akhonin, V.Yu. Bilous, E.L. Vrzhyzhevskyi, R.V. Selin, I.K. Petrychenko, S.L. Schwab, S.L. Antonyuk
STRUCTURE AND PROPERTIES OF WELDED JOINTS OF HEAT-RESISTANT TITANIUM ALLOY OF Ti–Al–Zr–Sn–Mo–Nb–Si SYSTEM PRODUCED BY ELECTRON BEAM WELDING** 13

V.O. Shapovalov, V.G. Mogylatenko, M.V. Karpets, R.V. Kozin
PRODUCING A WÜSTITE MELT BY THERMAL DECOMPOSITION OF HEMATITE PELLETS WITH ARGON PLASMA*** 24

G.G. Didikin, V.O. Osokin, Ya.A. Stelmakh
REFINING METALLURGICAL SILICON*** 30

L.M. Lobanov, O.P. Shutkevych, I.V. Kyyanets, I.L. Shkurat, K.V. Shyyan, V.V. Savitsky
DETECTION OF INTERNAL ULTRA-SMALL DEFECTS IN ALUMINIUM WELDED JOINTS BY THE SHEAROGRAPHY METHOD**** 38

O.M. Sharabura, L.I. Muravsky, O.G. Kuts
DETECTION OF CIRCULAR SUBSURFACE DEFECTS IN LAMINATED COMPOSITES USING OPTICAL-ACOUSTIC NONDESTRUCTIVE TESTING SYSTEM**** 42

INFORMATION

50 YEARS OF THE ARAKS EXPERIMENT: PROBING THE EARTH'S IONOSPHERE AND MAGNETOSPHERE WITH A POWERFUL ELECTRON BEAM**** 47

*Translated Article(s) from "Avtomatychne Zvaryuvannya" (Automatic Welding), No. 1, 2025.

**Translated Article(s) from "Suchasna Elektrometalurhiya" (Electrometallurgy Today), No. 4, 2024.

***Translated Article(s) from "Suchasna Elektrometalurhiya" (Electrometallurgy Today), No. 1, 2025.

****Translated Article(s) from "Tekhnichna Diahnostyka ta Neruinivnyi Kontrol" (Technical Diagnostics & Nondestructive Testing), No. 4, 2024.

Indexing: The electronic edition of the Journal is stored in the V.I. Vernadsky National Library of Ukraine (eVerLib), included in the OPEN UKRAINIAN CITATION INDEX database and international databases: CROSSREF, EBSCO, Google Scholar, INDEX COPERNICUS, IET Inspec, ULRICHSWEB.

DOI: https://doi.org/10.37434/tpwj2025.02.01

STUDY OF THE INFLUENCE OF ROUGHNESS ON THE MECHANICAL PROPERTIES OF STAINLESS STEEL SAMPLES MADE BY THE LPBF TECHNOLOGY

S.V. Adjamskiy[1,2], **G.A. Kononenko**[1,3,4], **R.V. Podolskyi**[1,3], **O.A. Safronova**[3]

[1]LLC "Additive Laser Technology of Ukraine"
31 v Serhiy Podolynskyi Str., 49000, Dnipro, Ukraine
[2]Institute of Transport Systems and Technologies of the NASU
5 Pysarzhevsky Str., 49000, Dnipro, Ukraine
[3]Z.I. Nekrasov Iron and Steel Institute of the NASU
1 Acad. Starodubov Sq., 49000, Dnipro, Ukraine
[4]Dnipro University of Technology
19 D Yavornytskyi Prosp., 49005, Dnipro, Ukraine

ABSTRACT

In the modern additive manufacturing of parts, the LPBF method has become widespread, which implies the technology of laser melting of a metal powder layer, that significantly expands the possibilities for optimizing the geometry of products. For parts manufactured using the traditional method (casting, deformation), it is known that the surface roughness can significantly affect the level of mechanical properties, since protrusions and depressions are stress concentrators. Parts manufactured using additive manufacturing technologies have an increased roughness, but their structural state after manufacturing is significantly different from traditional metal. It is often necessary to operate without subsequent mechanical surface treatment of products manufactured by the LPBF method. In the work the effect of roughness, the presence or absence of mechanical treatment of the working area of the samples on the mechanical properties under static tension conditions was determined. From the analysis of the profilometric curve and microstructure, it was found that samples without mechanical treatment have periodic protrusions, which is related to the texture formed during the manufacture. The average values of the mechanical properties do not differ significantly (less than 6.6 % for various characteristics) depending on the presence or absence of mechanical treatment, but deviations from the average within the sample regarding the values of tensile strength and reduction in area for samples without mechanical treatment are many times larger compared to the interval of value fluctuations within the sample for samples with mechanical treatment.

KEYWORDS: LPBF technology, roughness, stainless steel, mechanical properties

INTRODUCTION

As manufacturing processes continue to improve and develop, the demand for more rapid and less expensive manufacturing processes has led to the development of a number of rapid prototyping (RP) processes. Using additive manufacturing, almost any geometry with variations in size and complexity can be produced with a high degree of accuracy [1, 2]. The main limitation for the manufacture of parts with the methodology of topological optimization applied to them, which may contain internal channels of complex configuration, technological holes and removal of non-working elements to reduce weight, is the complexity of their final mechanical treatment due to their small size (e.g., holes, channels), geometric design features and the inability to bring the tool to a part. These complications necessitate designing of a CAD-model that takes into account and predicts manufacturing processes and features to prevent surface geometry defects in the finished product (e.g., incomplete fusion of holes) that cause their impassability during the process of manufacturing, etc.

Many researchers have considered the issue of final surface treatment of a part [2–5], the so-called post-treatment of parts by chemical, electrochemical and physical effects, which allows achieving the required surface roughness or cleaning as an alternative to mechanical treatment or as an intermediate one before further mechanical treatment. However, it should be noted that achieving the required surface roughness by these methods has a number of disadvantages, which were mentioned in [6–10], namely: loss of geometric parameters in the areas of a part with protruding edges, which is associated with more intensive electrochemical polishing processes in this area [10–11]; the presence of intergranular corrosion formation in the Down-skin areas; insufficient cleaning due to sintering of powder particles in the melting processes in the zone of metal-powder interaction during manufacturing.

Table 1. Actual chemical composition of 316L steel powder, wt.% [13]

C	Mn	Si	S	P	Cr	Ni	Cu	Mo
0.016	0.78	0.64	0.005	0.008	17.79	12.63	0.04	2.35

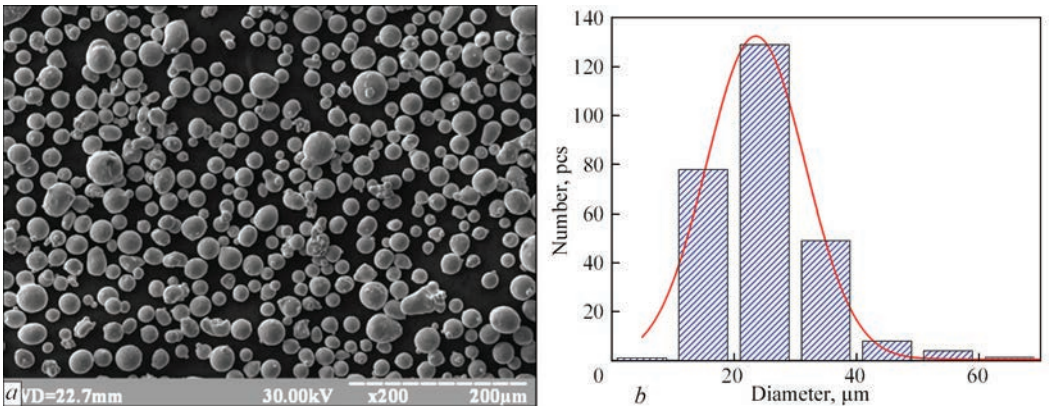

Figure 1. Particles of the source material of 316L powder at ×200 magnification (*a*) and the results of granulometric analysis (*b*) [13]

The results of studies [7–11] indicate that the roughness level of standard testing samples significantly affects the values of the final mechanical properties. This is even reflected in the standard technical documentation as requirements for the maximum allowable roughness of testing samples. However, it should be noted that this conclusion was made in relation to testing samples made by the traditional manufacturing method. This is mainly associated with the fact that in the technological processes of manufacturing testing samples using the traditional manufacturing method, there may be defects in the form of inconsistencies and inclusions: pores, cracks, carbides, nitrides, intermetallic phases, Laves phases, etc. that have a negative impact on the final mechanical properties, in addition to surface roughness. But, as is known from studies [12], mainly due to the rather high density of samples manufactured by the LPBF technology, namely 99.7–99.9 %, and taking into account the peculiarities of the processes of crystallization and the formation of an unbalanced highly dispersed structural state at high cooling rates, it was found that the conditions of the required roughness can be neglected, since the presence of elevated roughness may not have a significant effect on the final mechanical properties without the presence of a high rate of defects or deviations from the typical structure for parts made by the LPBF technology.

Based on the above, the study of the influence of roughness on the final mechanical properties is an important issue of materials science in additive manufacturing, since service properties can determine the final operational properties and the life of a part.

THE AIM

of this work is to study the effect of roughness of 316L stainless steel samples made by the LPBF technology on mechanical properties under static tensile conditions.

MATERIAL AND RESEARCH METHODS

In this work, tensile testing samples in the working area without and with mechanical treatment were investigated, fabricated in the Alfa-150D 3D printing machine manufactured by ALT Ukraine LLC with a 150×150 mm printing area equipped with an ytterbium laser with a wavelength of 1064 nm, the protective medium is argon gas circulating in the working chamber.

The samples were manufactured in the vertical direction with a working zone diameter of 5 and 6 mm (with an allowance for subsequent mechanical treatment) and a working zone of 25 mm length. The rational printing parameters that allowed obtaining a density of the finished product of 99.9 % were as follows: thickness of the deposited layer 40 µm, distance between tracks 0.1 mm, power 220 W, beam speed 1070 mm/s, scanning strategy — staggered fields 2.5×2.5 with a rotation angle of 67° relative to the previous layer [13] from metal powder of 316L austenitic steel with the actual chemical composition presented in Table 1, whose particle size analysis is shown in Figure 1. The selected material mainly consists of austenite and is not prone to the formation of

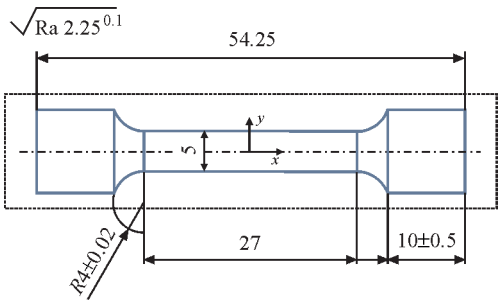

Figure 2. Geometric parameters of testing samples

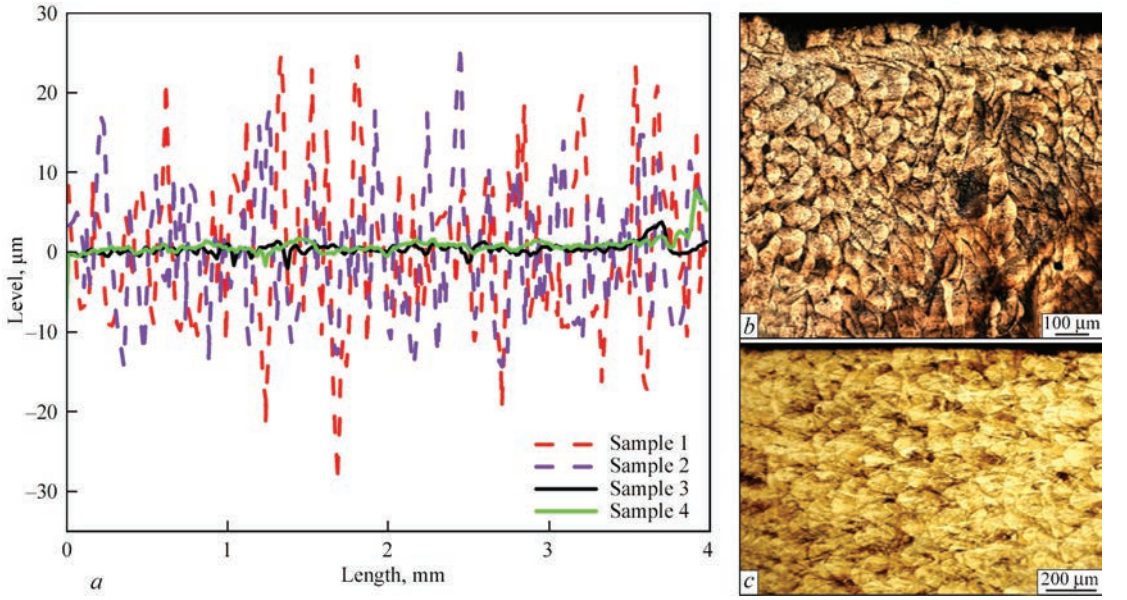

Figure 3. Profilometric surface curves of testing samples (*a*) and microstructure of testing samples 1 (*b*) and 3 (*c*) before tensile tests: 1, 2 — without mechanical treatment; 3, 4 — with mechanical treatment

an intermetallic phase as a result of short-term heating and cooling during heat treatment.

The samples were machined to final dimensions (Figure 2) using a HAAS ST10 lathe; five passes were made in the working area with a tool feed rate of 0.1 mm and a speed of 400 rpm.

Mechanical properties were determined by tensile testing using a standard method in an INSTRON machine. Roughness control was performed by two methods: using a DANA-260 roughness gauge and microstructural analysis in an AxioVert 200MMat optical microscope using specialized software ImageJ.

RESEARCH RESULTS

As a result of evaluating the surface condition of testing samples, it was found that the roughness of samples 1 and 2 without mechanical treatment in the working area was 24.41 μm (R_z) — 6.76 μm (R_a) and 24.56 μm (R_z) — 6.78 μm (R_a), respectively, the roughness of samples 3 and 4 after mechanical treatment was 2.28 μm (R_z) — 0.50 μm (R_a) and 2.26 μm (R_z) — 0.56 μm (R_a), respectively. Figure 3 shows the profilometric curves of the reference surface of 4 mm long testing samples and the surface microstructure of samples before testing.

From the analysis of the profilometric curve and microstructure (Figure 3, *a*, *b*), it was found that samples 1 and 2 without mechanical treatment have peaks at approximately equal distances from each other, which is associated with the texture formed during the crystallization of the base metal and local cyclic heating on the surface. These peaks and areas are the main stress concentrators during loading, which can lead to premature failure. Based on the results of the analysis of the curves of testing samples 3 and 4 (Figure 3, *a*, *c*), it was found that the roughness of these samples is insignificant, the range of fluctuations does not exceed the value of 4 μm. It can be assumed that the mechanical treatment properly levelled the surface of a testing sample without the presence of areas that could be stress concentrators during loading.

As a result of the tensile tests, stress-strain curves were obtained and the main mechanical properties were determined, which are shown in Table 2 and Figure 4.

From the analysis of the determined mechanical properties, it was found that in terms of average val-

Table 2. Results of determining the mechanical properties of samples made of 316 L stainless steel by the LPBF technology with different surface conditions of the working zone

Sample number	Condition	σ_t, MPa	Δ_{av}, σ_t, %*	$\sigma_{0.2}$, MPa	Δ_{av}, $\sigma_{0.2}$, %*	δ, %	Δ_{av}, δ, %*	ψ, %	Δ_{av}, ψ, %*
1	Without mechanical treatment	626.9	–2.3	561.6	–2.8	46.0	–1	66.3	+4,52
2		657.0	+2.29	594.0	+2.72	47.0	+1	60.4	–4,5
Medium		641,9	–	577.8	–	46.5	–	63.3	–
3	Mechanical treatment	677.9	+1.26	587.6	–1.56	43.9	+0.9	65.1	–0,07
4		660.7	–1.28	569.3	+1.57	43.0	–0.9	65.2	+0,07
Medium		669,3	–	578.4	–	43.4	–	65.15	–

Notes. Δ_{av}, $\sigma_t/\sigma_{0.2}/\delta/\psi$ is the deviation (%) from the average value within the sample.

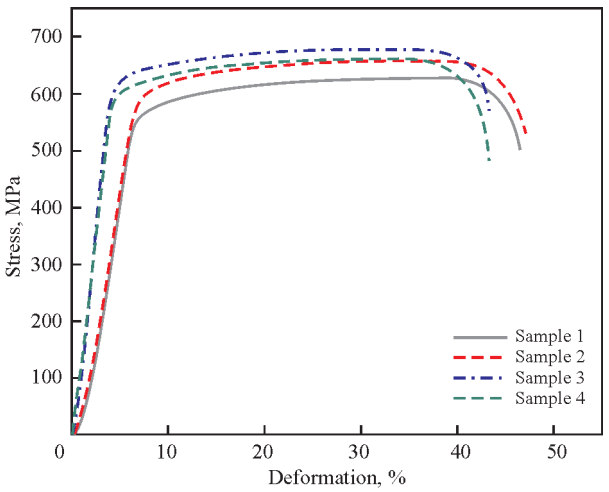

Figure 4. Stress-strain curves of 316 L stainless steel testing samples made by the LPBF technology with different surface conditions of the working zone: 1, 2 — without mechanical treatment; 3, 4 — with mechanical treatment

ues of samples 1 and 2, which were tested without preliminary mechanical treatment of the working zone, they have lower values of strength characteristics, namely: tensile strength — 641.9 MPa and yield strength 577.8 MPa, i.e. by 4.09 and 0.1 %, respectively, compared to samples with mechanical treatment of the working zone, namely: 669.3 and 578.4 MPa, respectively. However, it should be noted that the average values of the ductility indices varied in different directions: the average values of relative elongation (46.5 %) of testing samples 1 and 2 are 6.6 % higher, and the average values of reduction in area (63.3 %) are 2.8 % lower than the average values for samples 3 and 4, namely, relative elongation — 43.4 % and reduction in area — 65.15 %. These results for the ductility characteristics, namely: relative elongation and reduction in area are mainly associated with the opening and elongation of high roughness zones, as noted in [14–16].

The comparative analysis of the mechanical properties of testing samples 1 and 2 showed that samples which did not undergo the stage of mechanical treatment after manufacturing, have a deviation from the average value of ±2.5 % of the tensile strength and yield strength within the sample, and testing samples 3 and 4 have a deviation from the average value of ±1.4 %. From the analysis of deviations in the ductility characteristics, namely relative elongation from the average by groups, it was found that testing samples 1 and 2 without mechanical treatment have a spread of values in the range of ±1 %, while testing samples 3 and 4 have a spread of values in the range of ±0.9 %. As for the reduction in area, it was found that samples 1 and 2 have a range of deviations from the average of ±4.51 %, and samples 3 and 4 — ±0.07 %. Thus, it can be concluded that the average values of mechanical properties do not change significantly depending on the presence or absence of mechanical treatment, but it should be noted that the deviations from the average values of tensile strength and reduction in area for samples without mechanical treatment (1 and 2) in the middle of the sample are much larger compared to the range of fluctuations within the sample for samples with mechanical treatment (3 and 4).

CONCLUSIONS

1. It has been found that samples of 316 L steel made by the LPBF technology using rational technological parameters at a powder working layer thickness of 40 μm have a roughness of 24.41–24.56 μm (R_z); 6.76–6.78 μm (R_a); the surface profile has peaks at approximately equal distances from each other, which is associated with the texture formed during the crystallization process and local cyclic heating of the surface.

2. A comparative analysis of the mechanical properties determined on 316 L steel samples made by the LPBF technology revealed that the strength characteristics of samples with a working zone without mechanical treatment in the state after manufacturing have lower average values (tensile strength and yield strength are 4.09 and 0.1 % lower, respectively) compared to the average values of these characteristics determined on similar samples with mechanical treatment of the working zone. The average values of the ductility indices changed in opposite directions: the values of relative elongation of samples without mechanical treatment were 6.6 % higher, and the values of reduction in area were 2.8 % lower than the average values for similar samples with mechanical treatment.

3. The analysis of the mechanical properties of 316 L steel samples determined after tensile tests, which were manufactured by the LPBF technology, revealed that the spread of values within the sample relative to the average value of the yield strength and reduction in area is insignificant (1.0–2.5 %) regardless of the presence or absence of mechanical treatment. However, the deviations from the average values of the tensile strength and reduction in area for samples without mechanical treatment within the sample are many times greater compared to the range of fluctuations within the sample for samples with mechanical treatment.

REFERENCES

1. Khakbiz, M., Simchi, A. (2019) Optimization of powder injection molding process parameter for production SS316/TiC composite for biomedical application. *J. of Advanced Materials and Technologies*, 7(**4**), 1–10. DOI: https://doi.org/10.30501/jamt.2019.84282
2. Adjamskiy, S., Kononenko, G., Podolskyi, R., Badyuk, S. (2022) *Implementation of selective laser melting technology in Ukraine* [in Ukrainian]. Kyiv, Naukova Dumka. DOI: https://doi.org/10.15407/978-966-00-1856-3

3. Gu, D., Meiners, W., Wissenbach, K., Poprawe, R. (2012) Laser additive manufacturing of metallic components: Materials, processes and mechanisms. *Int. Mat. Rev*., **57**, 133–164. DOI: https://doi.org/10.1179/1743280411Y.0000000014
4. Wong, K.V., Hernandez, A. (2012) A review of additive manufacturing. *ISRN Mech. Eng*., **4**, 1–10. DOI: https://doi.org/10.5402/2012/208760
5. Brackett, D., Ashcroft, I., Hague, R. (2011) Topology optimization for additive manufacturing racket. http://utw10945.utweb.utexas.edu/Manuscripts/2011/2011-27-Brackett.pdf.
6. Gong, H., Rafi, K., Gu, H. et al. (2015) Influence of defects on mechanical properties of Ti–6Al–4V components produced by selective laser melting and electron beam melting. *Mater. Des*., **86**, 545–554. DOI: https://doi.org/10.1016/j.matdes.2015.07.147
7. Ashby, M., Mehl Medalist, R.F. (1983) Mechanical properties of cellular solids. *Metal. Transact. A*, **14**, 1755–1769. DOI: https://doi.org/10.1007/BF02645546
8. Lu, T.J., Stone, H., Ashby, M. (1998) Heat transfer in open-cell metal foams. *Acta Mater*., 46(**10**), 3619–3635. DOI: https://doi.org/10.1016/S1359-6454(98)00031-7
9. Evans, A.G., Hutchinson, J., Ashby, M. (1998) Multifunctionality of cellular metal systems. *Progr. Mater. Sci*., 43(**3**), 171–121. DOI: https://doi.org/10.1016/S0079-6425(98)00004-8
10. Adjamskyi, S.V., Kononenko, G.A., Podolskyi, R.V., Badyuk, S.I. (2023) Prospects for the application of electrochemical polishing of scaffold samples manufactured by additive technology. *Aviaciino-Kosmichna Tehnika i Tehnologiya*, **4sp2**, 76–81 [in Ukrainian]. DOI: https://doi.org/10.32620/aktt.2023.4sup2.10
11. Adjamskyi, S.V., Kononenko, G.A., Podolskyi, R.V., Badyuk, S.I. (2021) Study of electrochemical polishing efficiency of variable section samples with different roughness of steel AISI 316L, manufactured by technology of selective laser melting. *Aviaciino-Kosmichna Tehnika i Tehnologiya*, **2**, 66–73 [in Ukrainian]. DOI: https://doi.org/10.32620/aktt.2021.2.08
12. Herzog, D., Seyda, V., Wycisk, E., Emmelmann, C. (2016) Additive manufacturing of metals, *Acta Mater*., **117**, 371–392. DOI: https://doi.org/10.1016/j.actamat.2016.07.019
13. Adjamsky, S.V., Kononenko, G.A., Podolskyi, R.V. et al. (2023) Mechanical properties and microstructure of the 316L steel produced by different methods. *Powder Metallurgy and Metal Ceramics*, 62(**7–8**), 436–444. DOI: https://doi.org/10.1007/s11106-024-00405-9
14. Ronneberg, T., Davies, C.M., Hooper, P.A. (2020) Revealing relationships between porosity, microstructure and mechanical properties of laser powder bed fusion 316L stainless steel through heat treatment. *Mater. Des*., **189**, 108481. DOI: https://doi.org/10.1016/j.matdes.2020.108481
15. Yu, C.-H. (2022) *Anisotropic mechanical behaviours and thin-wall effects of additively manufactured austenitic alloys*. Linköping: Linköping University Electronic Press. DOI: https://doi.org/10.3384/9789179293154
16. Yu, C.-H., Peng, R.L., Lee, T.L. et al. (2022) Anisotropic behaviours of LPBF Hastelloy X under slow strain rate tensile testing at elevated temperature. *Materials Sci. and Eng.: A*, **844**, 143174. DOI: https://doi.org/10.1016/j.msea.2022.143174

ORCID
S.V. Adjamskiy: 0000-0002-6095-8646,
G.A. Kononenko: 0000-0001-7446-4105,
R.V. Podolskyi: 0000-0002-0288-0641,
O.A. Safronova: 0000-0002-4032-4275

CONFLICT OF INTEREST
The Authors declare no conflict of interest

CORRESPONDING AUTHOR
S.V. Adjamskiy
LLC "Additive Laser Technology of Ukraine"
31 v Serhiy Podolynskyi Str., 49000, Dnipro, Ukraine
E-mail: as@alt-print.com

SUGGESTED CITATION
S.V. Adjamskiy, G.A. Kononenko, R.V. Podolskyi, O.A. Safronova (2025) Study of the influence of roughness on the mechanical properties of stainless steel samples made by the LPBF technology. *The Paton Welding J*., **2**, 3–7.
DOI: https://doi.org/10.37434/tpwj2025.02.01

JOURNAL HOME PAGE
https://patonpublishinghouse.com/eng/journals/tpwj

Received: 31.10.2024
Received in revised form: 03.02.2025
Accepted: 27.03.2025

DOI: https://doi.org/10.37434/tpwj2025.02.02

WORKPLACE OF A COSMONAUT-WELDER FOR WELDING OF OBJECTS ON THE SURFACE OF THE MOON

N.V. Piskun[1], O.R. Bulatsev[1], V.A. Kryukov[1], Zeng Ruchuan[2], Ye.H. Ternovy[1]

[1]E.O. Paton Electric Welding Institute of the NASU
11 Kazymyr Malevych Str., 03150, Kyiv, Ukraine
[2]Beijing Spacecrafts No.104, Youyi Road, Haidian District, Beijing, P.R.C., China

ABSTRACT

When permans explore the Moon, not only the development of specialized electron beam welding equipment, but also auxiliary equipment, which is the workplace (WP) of a cosmonaut-welder, is very relevant. The paper describes the working project for the manufacture of the cosmonaut-welder WP, which is adapted for performing electron beam welding and related technologies with a hand tool in Earth orbit and on the surface of the Moon. The development of the WP took into account the peculiarities of the surface of the Moon and, first of all, the reduced gravity compared to the Earth, low temperature, and the presence and action of lunar dust (regolith). It is shown that the main technical characteristics of the cosmonaut-welder WP are: transport dimensions, mass characteristics, service area, selection of the chassis design of the mobile WP, as well as the specific choice of the electric drive and its power supply (autonomous, solar battery, battery or onboard network of the space station). The object of research and calculations was the typical design of the lunar module of DB "Pivdenne" Enterprise. The proposed workplace of the cosmonaut-welder is made in the form of a folded "cradle". In the transport position, it should take up a minimum of space and have a minimum weight. Several variants of the cosmonaut-welder workplace are proposed and considered according to the following parameters: dimensions in the transport position, the number of moving elements from the point of view of the influence of lunar dust — regoliths, the weight of the structure, convenience and ease of transfer from the transport position to the working position. Calculations of the necessary weight of the cosmonaut-welder workplace for performing work on the surface of the Moon have been carried out. The measures that ensure the reliability of the operation of the cosmonaut-welder workplace in open space and on the surface of the Moon are given.

KEYWORDS: workplace, cosmonaut-welder, electron beam welding, spacecraft engineering

INTRODUCTION

During exploration of the near-earth space and the surface of the Moon, it will be necessary to perform mounting, and in a number of cases also repair-restoration operations. Electron beam welding is a priority technology during fabrication of structures in spacecraft engineering, which allows producing reliable joints with guaranteed tightness without lowering of their strength and with preservation of weight and dimensional characteristics [1]. Over the recent years this welding process has regained its popularity among the researchers [2].

New generation electron beam tool developed at PWI for performance of welding and related processes, is capable of operating both in the manual (during work performance by cosmonaut-welder), and in the robotic version.

There are many situations, when we cannot do without the cosmonaut-researcher. These are non-standard situations, when it is necessary to assess the scope of violations, and determine the methods for performing the work or repair operations. There is a large number of operations, (primarily, repair-restoration operations or fixing the fragments of large-sized structures), for which it is difficult or impossible to prepare in advance. Moreover, occurrence of emergency situations is probable, which require performance of urgent technological operations, such as cutting, welding or brazing, during which the process and scope of operations will be determined by the cosmonaut directly in site.

During exploration of the Moon a lot of attention is given to establishing long-term lunar bases (LLB) and the infrastructure for these constructions. Taking into account the special physical conditions on the surface of the Moon, i.e., first of all, superhigh vacuum (up to 10^{-11} Pa), the required tightness of LLB structures can be ensured using welding. Therefore, development of specialized electron beam welding hardware and auxiliary equipment, which is the cosmonaut-welder workplace (WP) is relevant in exploration of the Moon.

Welding operator WP developed at PWI, is designed for performance of technological and repair operations in service of base modules on the surface of the Moon. It is required for operator movement to the place of performance of the operations of maintenance and repair of the space module skin, with the possibility of its lifting, tilting and rotation around the vertical axis [3].

During work performance in the Earth orbit, with the height close to 300 km, the movement of the flying object is accompanied by frequent changes of day and night: during every 90 minutes of flight the man is in the dark for 45 min. Human adaptation to the sun's rays, the brightness of which is doubled, also becomes relevant. Therefore, there is the need for ar-

tificial lighting for the cosmonaut-welder workplace during operation in complete darkness.

THE OBJECTIVE

of this work is creation of cosmonaut-welder workplace, meeting the modern requirements to space hardware, and using modern component base and advanced materials.

To achieve this objective, PWI "Space Technology" Department developed the working design for manufacturing cosmonaut-welder WP which is adapted for performing electron beam welding with the hand tool in the Earth orbit or on the surface of the Moon. During performance of this work, the peculiarities of the lunar surface were taken into account, first of all, reduced gravity, compared to Earth, low temperature and presence and impact of the lunar dust.

CREATION OF THE WELDING OPERATOR WORKPLACE

The following concept was proposed: develop a workplace of cosmonaut — welding operator, providing the opportunity of comfortable work of a man in a spacesuit during performance of the above-mentioned operations when mounting LLB structures and for other operations.

The welding operator WP was developed, proceeding from the conditions that it will be necessary to weld LLB structure elements 3000 mm in diameter, 6000 mm long and 6 mm thick.

The main technical characteristics of cosmonaut-welder WP are as follows: transport dimensions, weight characteristics, service area, selection of the mobile WP chassis design, as well as specific choice of the electric drive and its power supply (automonous, solar battery, battery or on-board network of the space station). WP should be made in the form of a folded structure, which in the transport position takes a minimum volume at minimum weight, depending on the selected structure material.

In this work a typical design of lunar module of DB "Pivdenne" enterprise was taken as the object of study. The horizontal orientation module is an aluminium welded structure of a cylindrical shell, frame and torispherical bottoms. The module outer diameter is equal to 3000 mm, and WP supports are adjustable by 100 mm by height.

Figure 1 shows the general view of a typical lunar module design [4]. For increase of the amount of movement in height, the supports provide the possibility of additional manual adjustment (possibility of extending the movement by 100 mm). Sequential connection of such blocks into one structure with various purposes, such as residential and research modules, allows creating a base, sufficient for the man to stay on the Moon.

Taking these factors into account, several design variants of the cosmonaut-operator WP were proposed and considered, in compliance with the following requirements: minimal overall dimensions in the transport position, limited number of mobile elements, minimal structure weight due to the selected heat-hardenable aluminium alloy 2219 with heat-reflecting coating over the entire structure surface [4, 5]. Convenience and ease of its transfer from the transport into the working position are provided. Convenience of performance of technological work can be provided due to operator position with different manipulator positions: from minimal lower position to maximal upper one. Possibility of the operator taking the intermediate positions is also provided, for instance when performing repair of defects on the module surface. In this variant the operator is an inclined position. Considering the effect of reduced gravity, the comfort of performing the technological operations is impaired, which requires reliable fixation of the operator relative to the work object.

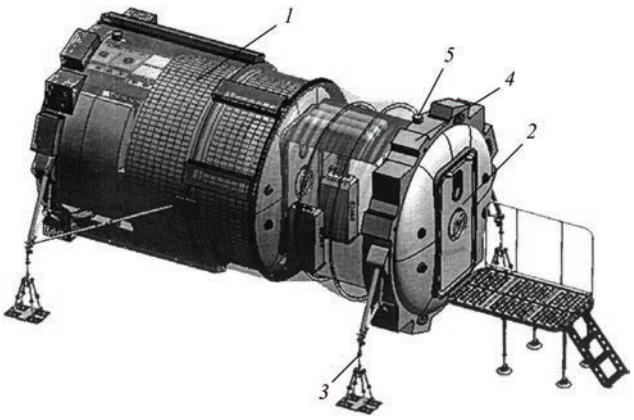

Figure 1. General view of a typical design of a lunar module of horizontal orientation with protection [4]: *1* — power shell with external coating; *2* — pressurized doors; *3* — mounting supports; *4* — docking device; *5* — pressure release device

During work performance on the surface of the Moon, the specialized cosmonaut-welder WP is one of the most complex tasks for realization of manual electron beam welding in the general complex of hardware for working in space [6]. Solving this problem will enable fixing the cosmonaut-welder for precise coordination of complex motions during welding.

Long-term operation and maintenance of such complex and volumetric equipment requires development of means for installation and scheduled preventive repair. It can be shell perforation as a result of accidental mechanical impact or from a meteorite strike. One of the main elements to solve this task is development of a welding tool and welder workplace to repair defects resulting from such phenomena.

Technical characteristics of welding operator workplace include the following; transport dimensions, weight characteristics, material for manufacture, service area, selection of the design of mobile workplace chassis, as well as specific choice of the electric drive and its power supply [7].

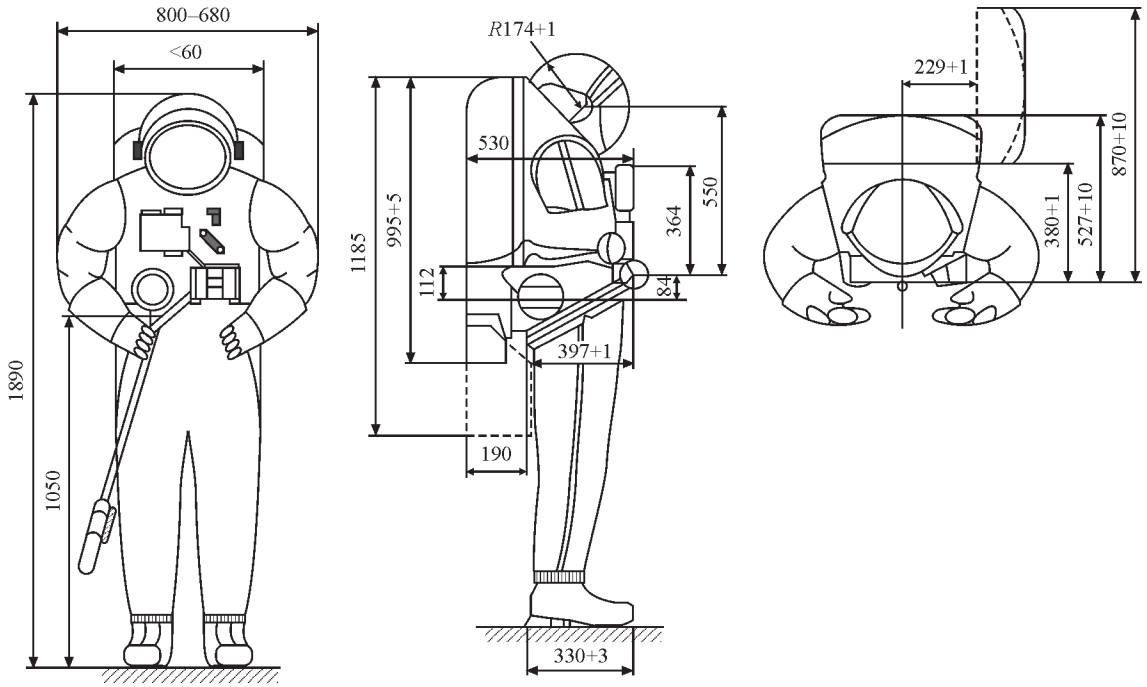

Figure 2. Tentative overall dimensions of a cosmonaut in a spacesuit

Figure 2 shows the tentative overall dimensions of a cosmonaut in a spacesuit. The welder's platform – "cradle" was developed for these data. A single variant of the "cradle" was developed, as this device is directly connected with the welding operator and cannot change.

The workplace proper is made in the form of a folded "Cradle" (Figure 3). It should take up minimum space and have minimum weight in the transport position. Special grips are holding the "cradle" frontal frame in the transport position and provide fixation of all the elements in such a shape. In the working position, the grips are holding the "cradle" side frames in the vertical position. Mounted on the workplace platform is a bracket to prevent slipping of the welder's feet during the workplace tilting, when working in the upper zone. Workplace tilting at an angle of approximately 30° is ensured by pitch drive, and workplace rotation by an angle of ±15° is performed by swing drive. Both these drives are located at the end of the other lever of workplace movement.

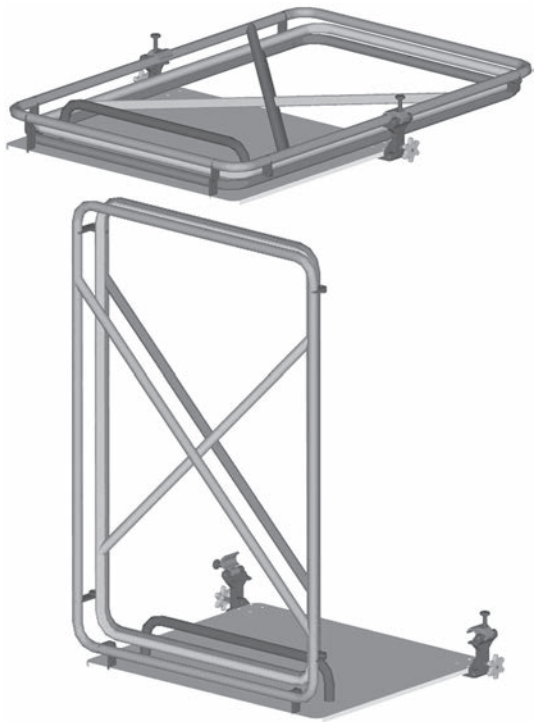

Figure 3. "Cradle" in the transport position

Figure 4 shows the intermediate transformations of the "cradle" from the transport into the working position. The process of deployment of all the structure elements is shown sequentially. The locking handrail is opened and closed by welding operator by turning the handle, when entering the "cradle".

OPTIONS OF COSMONAUT-WELDER WP DESIGN

Several options of cosmonaut-welder workplace have been proposed and considered based on the following parameters: overall dimensions in the transport position, number of mobile elements, structure weight, convenience and simplicity of transferring from the transport into the working position. The quality of welding operations performance largely depends on the position of cosmonaut-welder. Welding operations are performed by a man in a spacesuit in the vertical position. Figure 5 shows the variants of operator's position during performance of work on repairing defects on the module surface. Here, we had to tilt the operator. This is quite possible, in view of the low gravity value. The cylinder (the outer diameter of which is equal to 3000 mm) is resting on adjustable supports. The technical proposals were developed, proceeding from these initial data. Workplace inclina-

tion at an angle of ~300° is provided by a step drive, and the workplace rotation by an angle of ±150° is performed by the rotation drive.

The above-mentioned variant has better parameters of transport stowage the mobile workplace. The workplace should be transported using a four-wheel trolley with controlled stops.

Results of selection of operator workplace variants were used to make a 2D model, based on the mentioned variant. In some intermediate positions, the operator platform did not allow moving along the module outer surface.

For the platform to pass, it was necessary to move the workplace trolley, but such actions are inadmissible, as the trolley should stand on jack supports during the operator working in the workplace. This necessitated some changes in the length and position of manipulator base mounts. Manipulator base fasteners were moved to the position under the rear wheel axle; length of the first lever was increased to 1500 mm and length of the second lever — to 1800 mm.

Figure 5, *f* shows the upper position of the workplace, which enables servicing the module upper surface. This model allowed observing how the interaction of the operator, workplace and the module housing occurs during movement from the lower to the upper point, which commands the operator should issue from the control panel to the manipulator. The Table 1 gives the new dimensions of the welding operator workplace.

Workplace control panel should have the following commands. For the trolley: forward, backward, left, right, lower, raise the jacks. For workplace manipulator: forward, backward, up, down, left, right, tilt, straight, initial position. Initial position is when the operator is in the lowest position (Figure 5, *a*).

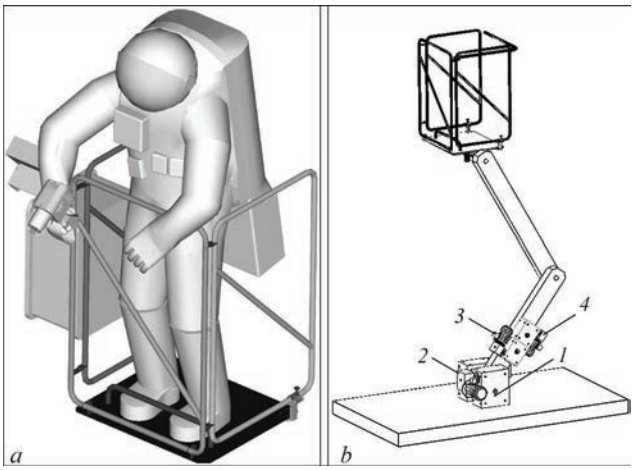

Figure 4. General layout of the welding operator platform and arrangement of the technological block with the seat for the tool and control panel in the "cradle": welding operator platform (*a*), manipulator with drives *1*, *2, 3*, *4* (*b*)

The next stage of the work was selection of the principles of placing and choosing the drives, mounted on WP manipulator "arm" (Figure 4, *b*). Several variants of drive placing were considered. Drives *1* and *2* should be responsible for movement of the platform with welding operator and power supply and control modules. More over, these drives are responsible for movement of the structure of the workplace proper. The weight of welding operator in the spacesuit is ~220 kg. Weight of all the modules is ~25 kg. Weight of the workplace structure should be ~130 kg. Thus, the total weight of all the elements, moving in space, is ~ 375 kg. On the Moon the weight is 6 times lower, than on the Earth, i.e. it is equal to ~62.5 kg. The distance from the center of fastening of the first lever to the center of gravity is ~2 m. Then, the moment required for movement of the welding operator is equal to 125 kg/m. Drives *1* and *2* have up to 165 kg/m mo-

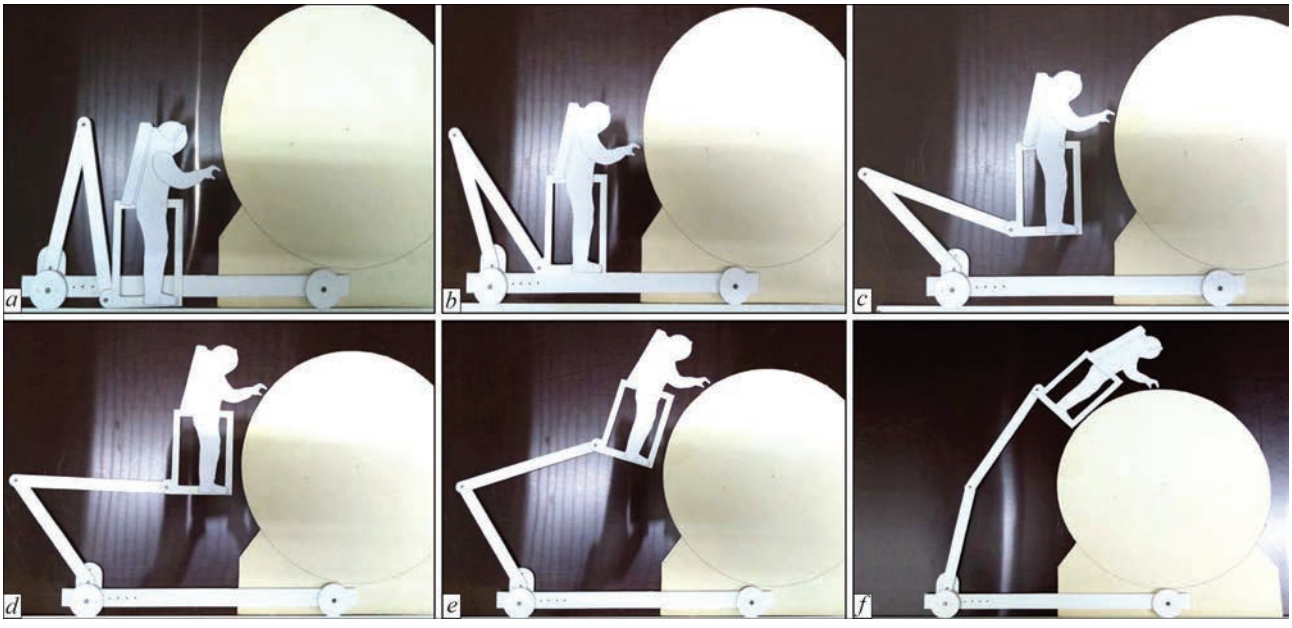

Figure 5. Intermediate phases of workplace positioning during maintenance of the module

Table 1. Dimensions of operator workplace

Parameter	Value, mm
Base between WP wheels	3000
Length of WP manipulator first lever	1500
Length of WP manipulator second lever	1800
Module diameter	3000
Depth of WP platform	820
Height of WP platform	1060
Width of WP trolley	220
Distance between trolley surface and first lever mounting axis	100

ment and drives *3* and *4* — 40 kg/m. At the stage of technical proposals the following drives were selected: gear motors NMRV 150/075 and NMRV 090/040.

Several variants of placement of the drives for controlling the manipulator arm position, WP inclination and rotation in the trolley base were considered. The most optimal is the WP manipulator variant with placing of the drives for controlling the manipulator arm position, WP inclination and rotation at the trolley base, which reduces the load on the manipulator even more, and greatly improves its characteristics. In this case, the weight to be moved in the smallest and the service area is greater than with all the other variants.

WP reliability is ensured by the following measures:

- application of verified component base with the required parameters and characteristics, ensuring their operation under the conditions, which are in place at different stages of ground-based training and during experiment performance;
- ensuring the quality of manufacturing, in accordance with the quality system acting at the enterprise;
- using the required safety factors during design and engineering optimization;
- conducting the required scope of ground-based experiments with application of advanced procedures, using limit testing modes with simulation of the conditions in place in standard and emergency situations.

CONCLUSIONS

1. Welding operator WP which is designed for performance of technological and repair operations in service of the station modules on the surface of the Moon, is an integral part of welding equipment.

2. Welding operator WP is necessary for operator movement from the place of performance of the operations on maintenance and repair of the space module skin with the capability of its lifting, tilting and rotation around the vertical axis.

3. Development of a specialized WP of cosmonaut-welder is one of the most complicated tasks in the overall complex of hardware for work performance in space. It enables fixing the cosmonaut-welder which is required for precise coordination of complex movements, ensuring quality and stable manual electron beam welding in orbit or on the surface of the Moon.

REFERENCES

1. Paton, B.E. (2023) Prospects for the application of welding in Space. *Avtomatychne Zvaryuvannya,* **3**, 1–15 [in Ukrainian].
2. https://thinkorbital.com/news/launch-of-first-welding-system/
3. Paton, B.E., Gavrish, S.S., Shulim, V.F. et al. (2000) Manual electron beam technological work in space. In: *Space: Technologies, Materials Science, Structures.* Ed. by B.E. Paton, Kyiv, PWI, 191–215 [in Russian].
4. Degtyarev, A.V., Lobanov, L.M., Kushnaryov, A.P. et al. (2020) On possibilities for development of the common-sense concept of habitats beyond the Earth. *Acta Astronautica,* **170**, 487–498. DOI: https://doi.org/10.1016/j.actaastro.2020.02.014
5. Paton, B.E. et al. (1999) Device for manual electron beam processing of materials in Space. United States, Pat. # 5,869,801.
6. Hlushak, S.O. (2023) Evolution of electron beam hardware for welding in Space. *The Paton Welding J.*, **8**, 78–84. DOI: https://doi.org/10.37434/tpwj2023.08.11
7. Paton, B.E., Bulatsev, O.R., Perepechenko, B.I. et al. (2000) Device of the work station for conducting experiments in Space. Pat. UA on Invention 95020653, Publ. 15.09.2000 [in Ukrainian].

ORCID

N.V. Piskun: 0000-0003-1459-2310,
Zeng Ruchuan: 0009–0000–4551–3641,
Ye.H. Ternovy: 0000–0002–4323–0944

CONFLICT OF INTEREST

The Authors declare no conflict of interest

CORRESPONDING AUTHOR

N.V. Piskun
E.O. Paton Electric Welding Institute of the NASU
11 Kazymyr Malevych Str., 03150, Kyiv, Ukraine.
E-mail: nadamova54@gmail.com

SUGGESTED CITATION

N.V. Piskun, O.R. Bulatsev, V.A. Kryukov, Zeng Ruchuan, Ye.H. Ternovy (2025) Workplace of a cosmonaut-welder for welding of objects on the surface of the Moon. *The Paton Welding J.*, **2**, 8–12.
DOI: https://doi.org/10.37434/tpwj2025.02.02

JOURNAL HOME PAGE

https://patonpublishinghouse.com/eng/journals/tpwj

Received: 27.09.2024
Received in revised form: 07.01.2025
Accepted: 31.03.2025

DOI: https://doi.org/10.37434/tpwj2025.02.03

STRUCTURE AND PROPERTIES OF WELDED JOINTS OF HEAT-RESISTANT TITANIUM ALLOY OF Ti–Al–Zr–Sn–Mo–Nb–Si SYSTEM PRODUCED BY ELECTRON BEAM WELDING

S.V. Akhonin[1], V.Yu. Bilous[1], E.L. Vrzhyzhevskyi[1], R.V. Selin[1], I.K. Petrychenko[1], S.L. Schwab[1], S.L. Antonyuk[2]

[1]E.O. Paton Electric Welding Institute of the NASU
11 Kazymyr Malevych Str., 03150, Kyiv, Ukraine
[2]SC "O.K. Antonov ANTK"
1 Mriya Str., 03062, Kyiv, Ukraine

ABSTRACT

Heat-resistant titanium-based pseudo-α-alloys have become widely applied in many sectors of modern industry, which is due to a high level of their specific mechanical properties at higher temperatures. Application of electron beam welding technology is the most rational when manufacturing parts and components from heat-resistant titanium alloys. Its special feature are high rates of cooling of the weld metal and HAZ, which complicates welding of heat-resistant titanium alloy Ti–6.5Al–5.3Zr–2.2Sn–0.6Mo–0.5Nb–0.75Si, where the high silicon content ensures lower ductility characteristics at room temperature. The influence of electron beam welding on the weld metal and HAZ structure, and on the mechanical properties of the heat-resistant titanium alloy Ti–6.5Al–5.3Zr–2.2Sn–0.6Mo–0.5Nb–0.75Si was studied. It was found that application of electron beam welding with local heat treatment at 750 °C leads to reduction of the size of packages with Widmanstatten morphology from 50–100 to 20–50 μm and increase in welded joint strength from 996 to 1041 MPa, which corresponds to base metal strength.

KEYWORDS: heat-resistant titanium alloy, microstructure, mechanical properties, electron beam welding, local heat treatment

INTRODUCTION

Heat-resistant titanium alloys combine high specific values of strength, increased characteristics of fatigue and crack propagation resistance, as well as corrosion resistance [1, 2]. However, establishing the possibility of producing sound welded joints of advanced heat-resistant titanium alloys is an urgent task in view of the growing requirements to engine components being designed [3, 4]. Heat-resistant titanium-based pseudo-α-alloys are considered promising materials in aviation and space engineering, and automotive industry, owing to preservation of the α-structure at elevated temperatures, which is due to maintaining the temperature of polymorphic (α→β)-transformation at the highest possible level. During polymorphic (α→β)-transformation, the hexagonal close packed crystal lattice of the more heat-resistant α-titanium loses its stability and develops into a cubic body-centered modification of the less heat-resistant β-titanium [5, 6]. The highest heat resistance is demonstrated by doped alloys of Ti–Si–X systems due to formation in the cast state of a framework of strengthening phases arising during eutectic crystallization [7]. One of the directions for increasing the titanium alloy heat resistance is creation of in-situ composites based on refractory silicide compounds. In Ti–Al–Si system a continuous series of eutectic compositions forms along the surface of isoconcentration of isoconcentration close to 10 at.% Si, where α-Ti is the matrix, and Ti_5Si_3 has the role of strengthening phase [8, 9]. One of such promising alloys is the experimental pseudo-α-alloy Ti–6.5Al–5.3Zr–2.2Sn–0.6Mo–0.5Nb–0.75Si, which can be used to manufacture parts of GTE turbocompressor rotor, as well as of the engine and cooling systems of internal combustion engines (ICE), because their specific weight will be two times less, compared to traditional materials [10, 11].

The great majority of structures from heat-resistant titanium alloys are manufactured using the technologies of electron beam welding (EBW) [12, 13]. EBW features are high quality of welding zone protection from contact with atmospheric gases and welding performance in one pass, as well as the possibility of conducting local heat treatment (LHT) of the welded joint in the vacuum chamber right after welding. The possibility of performing local heating and further heat treatment in the vacuum chamber is an essential advantage of EBW technology [14, 15]. Preheating of the welded joints is a rather effective technological measure which is used in welding high-strength steels to prevent cold cracking [16–18].

Table 1. Modes of electron beam welding of heat-resistant titanium alloy Ti–6.5Al–5.3Zr–2.2Sn–0.6Mo–0.5Nb–0.75Si

Mode	Beam current, mA	Welding speed, mm/s	Preheating temperature, °C	LHT temperature, °C	LHT duration, min
1	90	7	–	–	–
2	–»–	–»–	400	–	–
3	–»–	–»–	–»–	750	10

EBW features high rates of cooling of the weld metal and HAZ, which results in lower strength of the welded joint of heat-resistant titanium alloys in as-welded condition. In case of performance of welded joints on promising heat-resistant titanium alloy Ti–6.5Al–5.3Zr–2.2Sn–0.6Mo–0.5Nb–0.75Si, EBW is more complicated in connection with the high content of silicon, which is several times higher than silicon solubility in titanium in the weld metal [19]. Influence of the thermal cycle of welding leads to structural changes in the weld metal and HAZ of this alloy resulting in development of a stressed state and in formation of cold cracks, considering the low ductility of silicon-alloyed metal [20, 21].

Thus, it is necessary to study the weldability of new generation heat-resistant titanium alloys and to determine the technological welding modes, which will provide an optimal structure of the weld metal and HAZ, in order to achieve a set of high mechanical properties of the welded joints with the strength not less than 90 % of that of the base material.

The objective of this work is studying the influence of electron beam welding on the structure of weld metal and HAZ, as well as mechanical properties of welded joints of heat-resistant titanium alloy Ti–6.5Al–5.3Zr–2.2Sn–0.6Mo–0.5Nb–0.75Si.

MATERIALS AND EXPERIMENTAL PROCEDURE

Heat-resistant titanium alloy Ti–6.5Al–5.3Zr–2.2Sn–0.6Mo–0.5Nb–0.75Si is highly sensitive to the thermal cycle of welding. Therefore, it is necessary to study the influence of such technological measures, available for electron beam welding, as preheating and local heat treatment in the vacuum chamber, on the possibility of producing defectfree welded joints.

Electron beam welding was performed in UL-144 machine fitted with ELA 60/60 power unit. Plates made cut out of an ingot of heat-resistant titanium alloy of Ti–6.5Al–5.3Zr–2.2Sn–0.6Mo–0.5Nb–0.75Si system produced by electron beam melting, were used for investigations [22]. Hot-rolled plates from the above-mentioned alloy 10 mm thick were produced in a reversible two-roll rolling mill 500/350 of Skoda Company [23]. Rolling began at the temperature of 1050 °C, the temperature of the end of rolling was not lower than 800 °C. After rolling, the metal was annealed at 900 °C for 1 h.

Chemical composition of experimental alloy Ti–6.5Al–5.3Zr–2.2Sn–0.6Mo–0.5Nb–0.75Si was as follows, wt.%: Ti — base; Al — 6.4–6.8; Zr — 5.1–5.4, Sn — 1.8–2.5; Mo — 0.55–0.75; Nb — 0.5–0.6; Si — 0.74–0.76.

EBW of 10 mm thick samples was performed. Samples of heat-resistant Ti–6.5Al–5.3Zr–2.2Sn–0.6Mo–0.5Nb–0.75Si alloy were assembled without edge preparation or a gap. EBW modes for heat-resistant titanium alloy Ti–6.5Al–5.3Zr–2.2Sn–0.6Mo–0.5Nb–0.75Si are given in Table 1. Figure 1 shows an example of a welded joint of heat-resistant Ti–6.5Al–5.3Zr–2.2Sn–0.6Mo–0.5Nb–0.75Si alloy produced by EBW without application of preheating or LHT.

Power of the electron beam during preheating and LHT was 3 kW, which ensured up to 750 °C temperature in the treatment zone. The width of the treatment zone with preheating and LHT along the weld was 30 mm. The temperature in LHT zone was monitored with thermocouples and recorded using a multichannel potentiometer KSP4. Figure 2, *b* gives an example of the thermal cycle in welding with preheating up to 400 °C, Figure 2, *c* presents the recorded thermal cy-

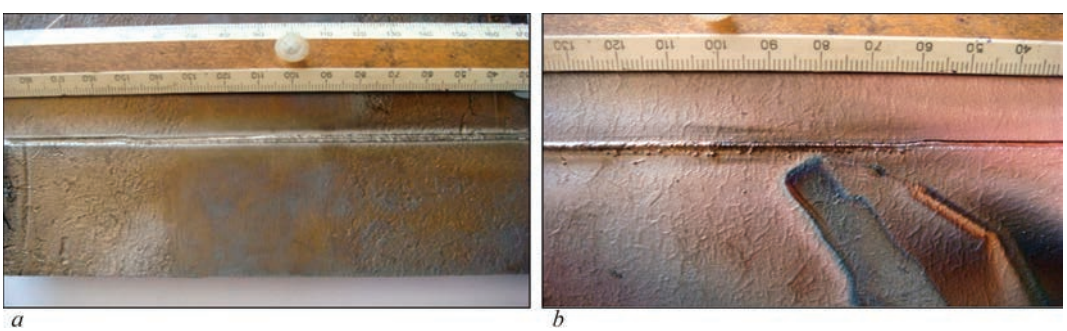

Figure 1. Welded joint of heat-resistant titanium alloy Ti–6.5Al–5.3Zr–2.2Sn–0.6Mo–0.5Nb–0.75Si made by EBW (mode 1), in as-welded condition: *a* — face; *b* — root side

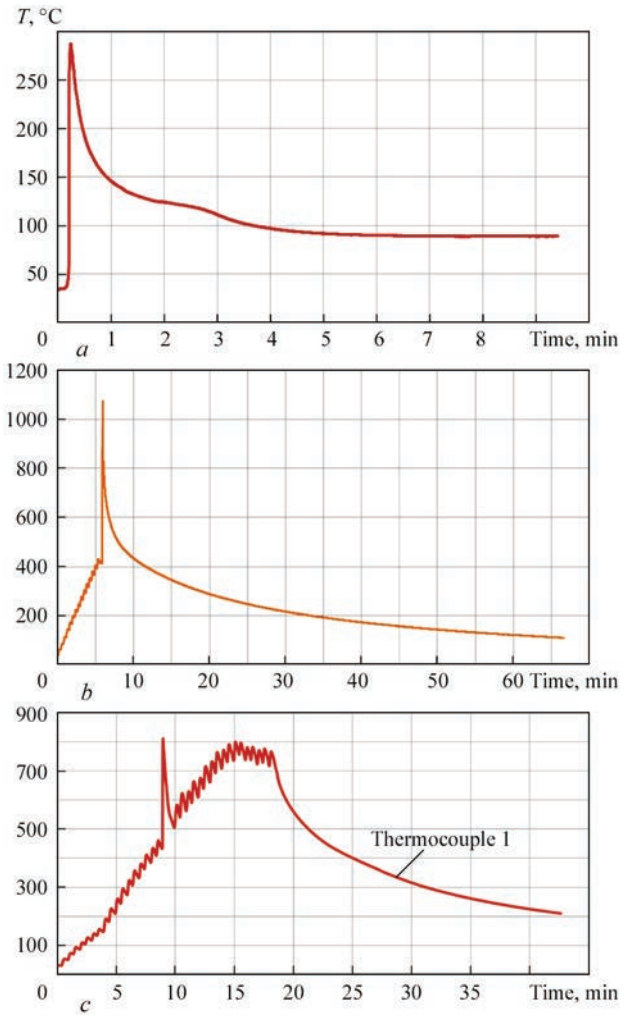

Figure 2. Thermal cycle in the HAZ in EBW of heat-resistant Ti–6.5Al–5.3Zr–2.2Sn–0.6Mo–0.5Nb–0.75Si alloy: *a* — without preheating or LHT; *b* — with preheating to 400 °C; *c* — with preheating to 400 °C and further LHT at 750 °C

cle in welding with preheating to 400 °C and postweld LHT at 750 °C.

Examination of transverse sections of EB welded joints on heat-resistant Ti–6.5Al–5.3Zr–2.2Sn–0.6Mo–0.5Nb–0.75Si alloy showed that the macrostructure of the base metal, weld metal and HAZ is more homogeneous in the condition after preheating and LHT (Figure 3).

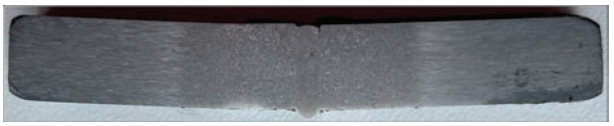

Figure 3. Macrosection of as-welded joint of heat-resistant titanium alloy Ti–6.5Al–5.3Zr–2.2Sn–0.6Mo–0.5Nb–0.75Si made by EBW (mode 3)

MICROSTRUCTURE OF EB WELDED JOINTS OF HEAT-RESISTANT TITANIUM ALLOY Ti–6.5Al–5.3Zr–2.2Sn–0.6Mo–0.5Nb–0.75Si

The Ti–6.5Al–5.3Zr–2.2Sn–0.6Mo–0.5Nb–0.75Si alloy belongs to the group of pseudo-α-alloys, in which the α-phase is the alloy matrix, and a certain amount of the β-phase can form, depending on the specific conditions of microstructure formation. Studies of the initial alloy structure immediately after rolling was over, showed that the metal in as-rolled condition has a fine-grained structure, formed by globular (equiaxed) grains 5–15 μm in size, whereas precipitates of β-phase crystallites are observed along the boundaries of α-phase grains in relatively small amounts (Figure 4).

Before welding, the alloy was vacuum annealed at the temperature of 900 °C. Microstructure analysis indicates that annealing led to a change in the alloy structure morphology (Figure 5, *a*). During cooling after annealing, a Widmanstatten structure (basket weave structure) was formed, which consisted of α- and β-phase platelets. The size of individual packages of the Widmanstatten structure, assessed by the maximal length of the platelets in the package was 20–50 μm (Figure 5, *b*) which is indicative of a significant increase in the size of grains of the matrix α-phase during annealing.

Figure 6 shows the microstructure of weld metal of EB welded joint of heat-resistant Ti–6.5Al–5.3Zr–2.2Sn–0.6Mo–0.5Nb–0.75Si alloy. Image magnification is determined by the scale mark on the respective photo. Microstructure analysis indicates that a typical dendrite structure of cast metal forms in the weld zone (Figure 6, *a*). It is dense and no defects such as porosity, cracks or nonmetallic inclusions are detected in it.

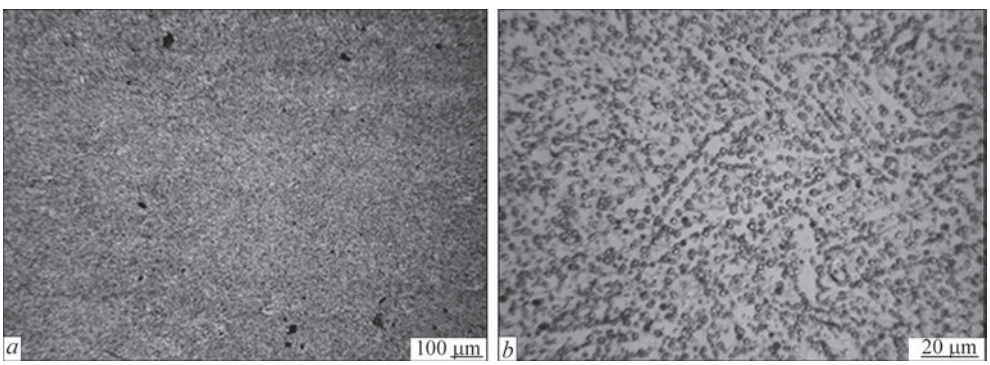

Figure 4. Microstructure of the central zone of a hot-rolled sheet of Ti–6.5Al–5.3Zr–2.2Sn–0.6Mo–0.5Nb–0.75Si alloy in as-rolled state

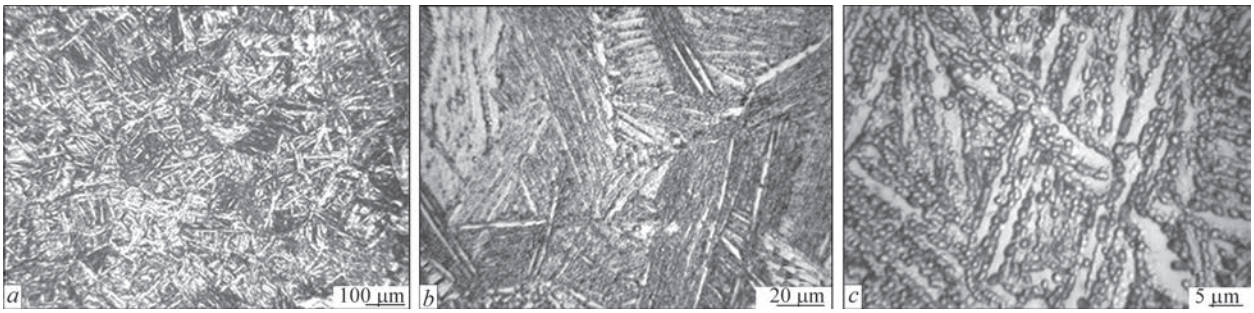

Figure 5. Microstructure of the central zone of a 10 mm hot-rolled sheet of Ti–6.5Al–5.3Zr–2.2Sn–0.6Mo–0.5Nb–0.75Si alloy in as-annealed condition

The size of dendrite branches on the section surface can be tentatively assessed by the difference in etchability of individual areas, and it is equal to 100–500 μm. Dendrite area boundaries have no excess phase precipitation, and are not the weak points of the material. It is important that rapid cooling of the molten weld metal in EBW results in formation of rather dispersed packages of Widmanstatten morphology in the dendritic areas with package size (by the size of the largest platelets) in the range of 20–50 μm, which is close to the characteristics of dispersion of base metal structure.

Considering the high rate of cooling to temperatures below $T_{p.tr}$, the intragranular structure of the weld metal is represented by martensite acicular α′-phase (Figure 6, *b*), which forms due to β→α′ transformation. The primary grain boundaries have a thin intermittent α-fringe, the thickness of which is close to 1–2 μm. The martensite needle thickness is 1–2 μm. Dispersed particles of titanium silicides of up to 1 μm size, as well as an intermittent layer between the martensite platelets are also present in the weld metal (Figure 6, *c*).

Microstructure analysis of the HAZ metal of EB welded joint of heat-resistant titanium alloy Ti–6.5Al–5.3Zr–2.2Sn–0.6Mo–0.5Nb–0.75Si indicates that the HAZ metal preserves the main morphological and dimensional characteristics of the base metal (Figure 7).

Obviously, β-phase precipitation in the α-phase matrix, as well as potential formation of α_2-phase (Ti_3Al) precipitates under the impact of the welding heat and partial decomposition of metastable β-phase blocks the growth of matrix grain. This assumption is further confirmed by a certain reduction of the amount of β-phase observed in the HAZ, compared to the base metal structure. The HAZ width is equal to approximately 500 μm. HAZ metal consists of equiaxed grains with lamellar intragranular structure, the thickness of α-platelets in the colonies being equal to 1.5–5.0 μm (Figure 7, *b*). Dispersed particles from less than 1.0 to 1.5 μm size are localized, mainly, within

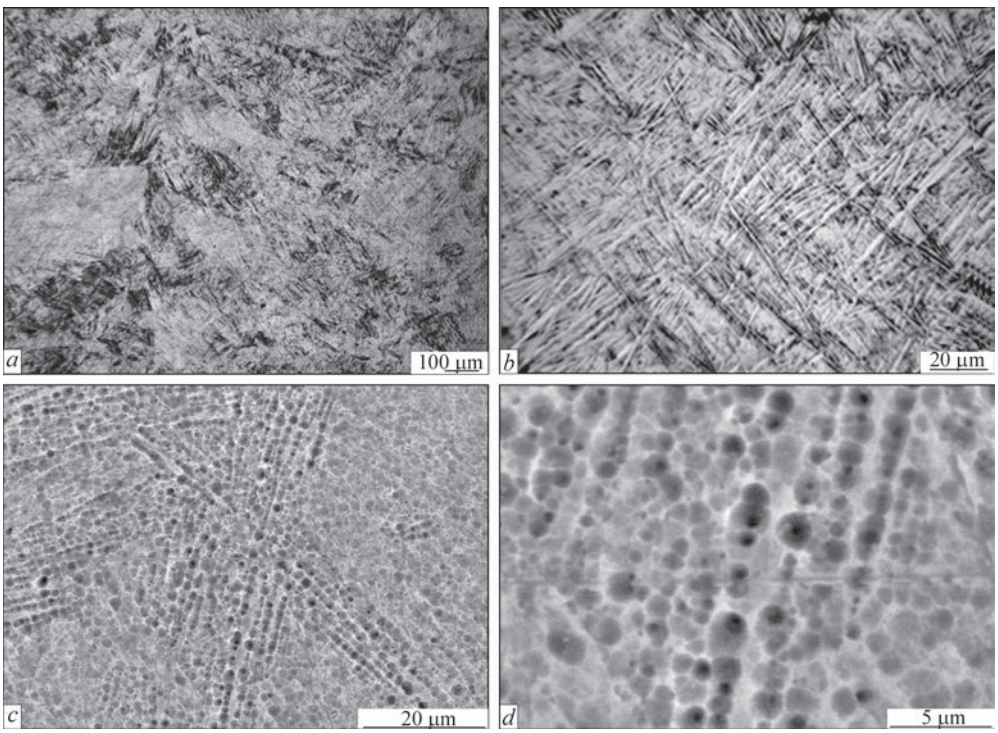

Figure 6. Microstructure of weld metal of EB welded joint of heat-resistant Ti–6.5Al–5.3Zr–2.2Sn–0.6Mo–0.5Nb–0.75Si alloy in as-welded condition

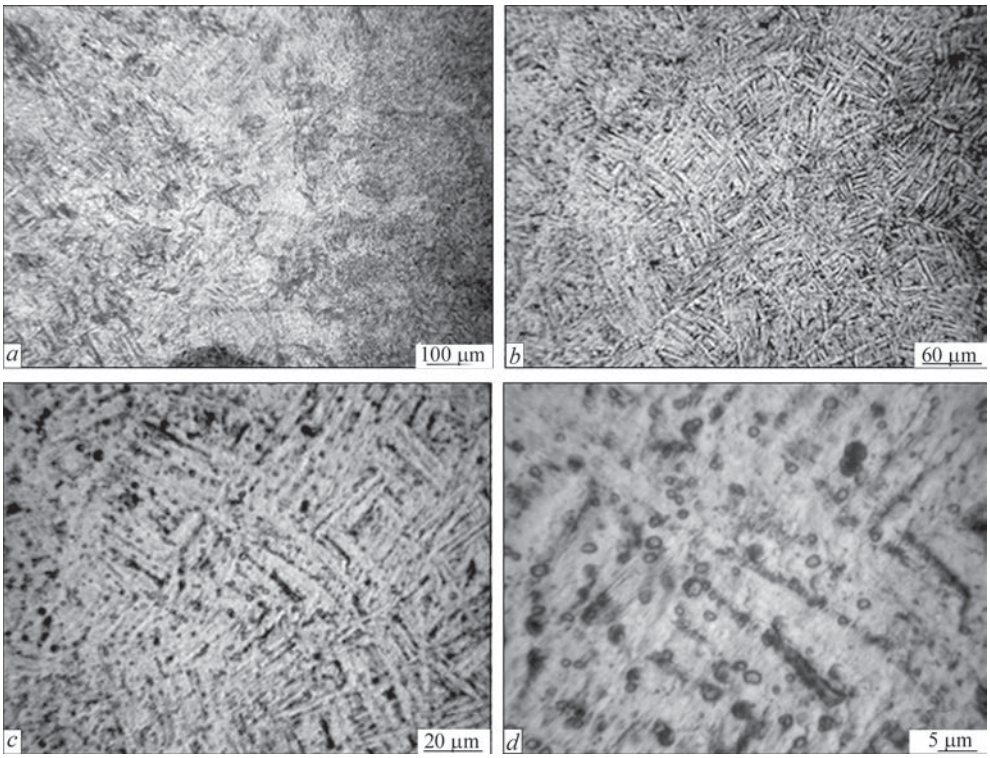

Figure 7. Microstructure of HAZ metal of EB welded joint of heat-resistant Ti–6.5Al–5.3Zr–2.2Sn–0.6Mo–0.5Nb–0.75Si alloy in as-welded condition

the platelets. In some places there are elongated layers of another phase between the adjacent platelets of up to 3–8 μm length (Figure 7, *c*, *d*).

Determination of microhardness distribution in EB welded joint of heat-resistant titanium alloy Ti–6.5Al–5.3Zr–2.2Sn–0.6Mo–0.5Nb–0.75Si in as-welded condition led to the conclusion that the microhardness level in different areas of the welded joint is very heterogeneous (Figure 8).

The greatest microhardness values are recorded in the weld metal at the level of 3000 MPa. The lowest level of 2400 MPa was found in the base metal, and the medium one of 2500 MPa was determined in the HAZ metal. It should be noted that a heterogeneous microhardness distribution causes the heterogeneity of the welded joint mechanical properties.

In order to ensure microstructure homogeneity, and homogeneous distribution of microhardness in different areas of welded joints of heat-resistant titanium alloy Ti–6.5Al–5.3Zr–2.2Sn–0.6Mo–0.5Nb–0.75Si, EBW with preheating to 400 °C was used.

Microstructure analysis of weld metal of welded joint of heat-resistant Ti–6.5Al–5.3Zr–2.2Sn–0.6Mo–0.5Nb–0.75Si alloy, made by EBW with preheating to

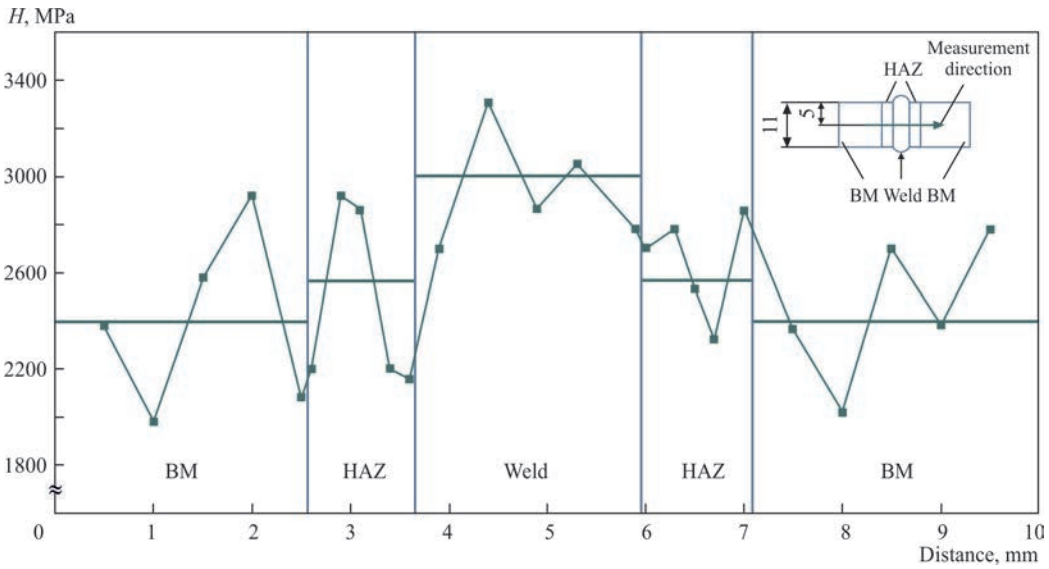

Figure 8. Distribution of microhardness (*H*) in EB welded joint of heat-resistant titanium alloy Ti–6.5Al–5.3Zr–2.2Sn–0.6Mo–0.5Nb–0.75Si in as-welded condition

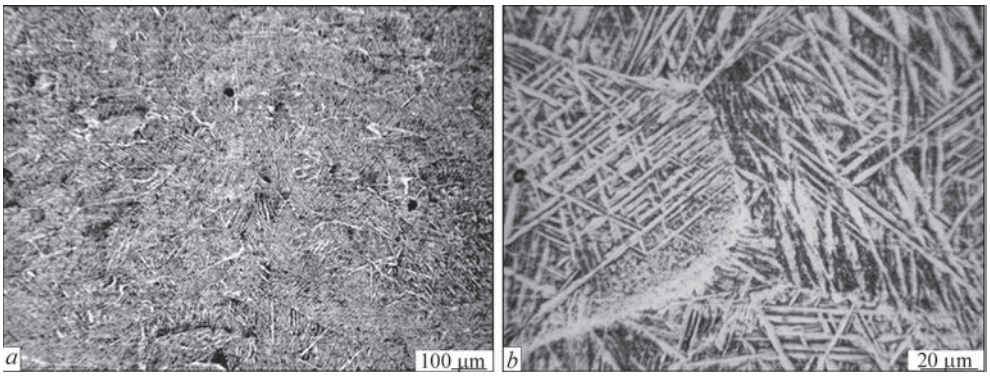

Figure 9. Microstructure of weld metal of welded joint of heat-resistant Ti–6.5Al–5.3Zr–2.2Sn–0.6Mo–0.5Nb–0.75Si alloy, made by EBW with preheating to 400 °C, in as-welded condition

400 °C indicates formation of a typical dendrite structure of cast metal in the weld zone (Figure 9). It is dense and no defects such as porosity, cracks or nonmetallic inclusions are indentified in it. The weld metal consists of equiaxed primary β-grains, elongated in the direction of heat removal. The equiaxed grains are localized predominantly along the weld axis.

There is an α-fringe along the primary grain boundaries, the thickness of which is 1.5–7.0 μm (Figure 9, *a*). The size of the dendrite branches in the section plane can be tentatively assessed by precipitation of the α-phase interlayers along the boundaries of the dendrite areas. It is equal to 200–300 μm. Precipitation of such interlayers decreases the structure homogeneity and may potentially facilitate crack propagation during fracture. The intragranular structure consists of martensitic α-phase, which mainly forms small-sized colonies, the colony width being 5–20 μmm (Figure 9, *b*). Platelet thickness is from 1 to 2 μm. Chains of dispersed particles are observed between α-phase platelets.

As in the case of welding without preheating, accelerated cooling of the molten weld metal results in formation of rather dispersed packages of Widmanstatten morphology in the dendritic areas. In this case, however, coarser packages with the size (by the size of the largest platelets) in the range of 50–100 μm are formed that is larger than in welding without preheating, and larger than in the base metal structure. Combined with formation of α-phase interlayers on the boundaries of the dendritic areas and on the boundaries of individual Widmanstatten packages, this can potentially facilitate crack initiation and propagation during destruction.

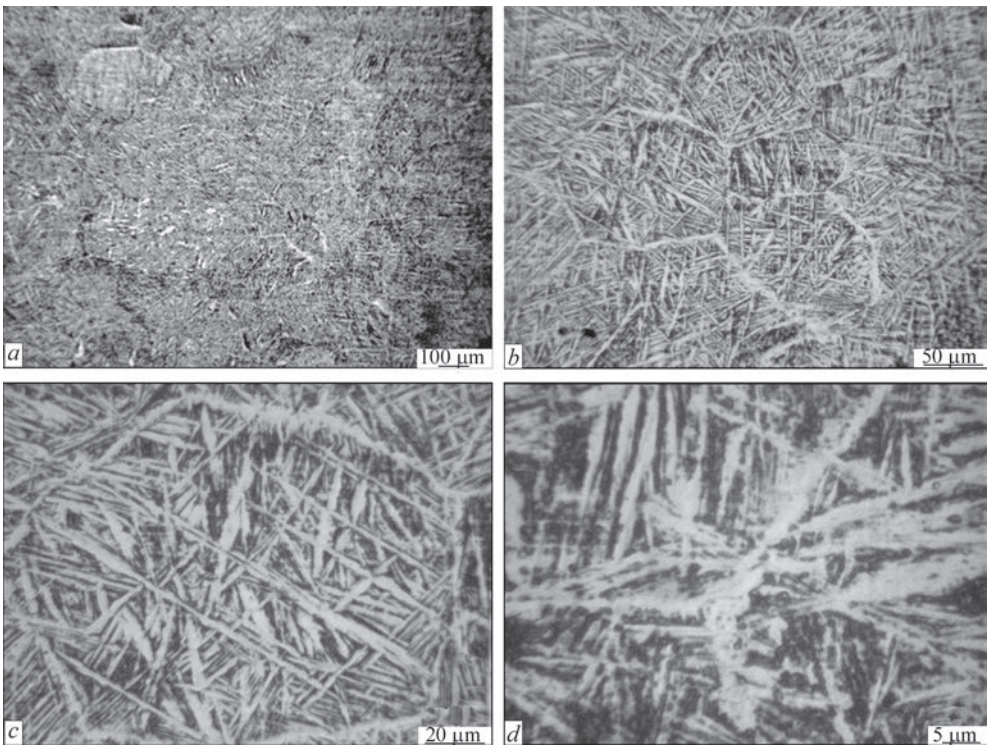

Figure 10. Microstructure of HAZ metal of welded joint of heat-resistant Ti–6.5Al–5.3Zr–2.2Sn–0.6Mo–0.5Nb–0.75Si alloy, made by EBW with preheating to 400 °C, in as-welded condition

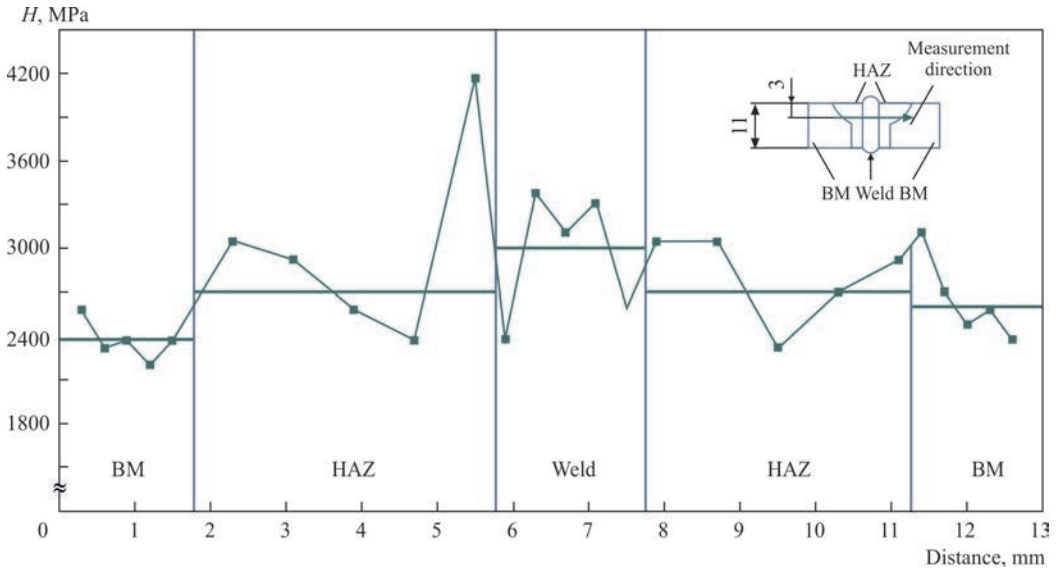

Figure 11. Distribution of microhardness (*H*) in welded joint of heat-resistant Ti–6.5Al–5.3Zr–2.2Sn–0.6Mo–0.5Nb–0.75Si alloy made by EBW with preheating to 400 °C, in as-welded condition

Analysis of metal microstructure in the HAZ of the welded joint of heat-resistant titanium alloy Ti–6.5Al–5.3Zr–2.2Sn–0.6Mo–0.5Nb–0.75Si, produced by EBW with preheating to 400 °C, indicates that structure coarsening is observed in the HAZ in welding with preheating, compared to base metal structure (Figure 10). HAZ metal consists of equiaxed primary grains of 50–300 μm size (Figure 10, *b*, *c*) with an α-fringe, the thickness of which is 1–7 μm. The intragranular structure is made up of lamellar α-phase, which forms small colonies of up to 20 μm size (Figure 10, *c*, *d*). Platelet thickness is 1.5–5.0 μm. Isolated dispersed particles and their clusters are observed in the gaps between the platelets (Figure 10, *d*).

Similar phase precipitates were observed also in other areas of the welded joint of this alloy, as well as in the welded joint made by EBW without preheating. It can be noted, that structure of welded joints produced by EBW without preheating and with preheating is identical in the corresponding areas.

Thus, while the main morphological characteristics of base metal (basket weave structure) are preserved, the Widmanstatten package size is somewhat larger, and formation of α-phase interlayers is observed on package boundaries. Additional supply of thermal energy into the welding zone due to preheating in EBW promotes temperature increase in the welding zone and slows down the cooling after completion of the welding process, that leads to significant coarsening of the weld structure and occurrence of grain growth processes in the HAZ.

Establishing the microhardness distribution in EB welded joint of heat-resistant titanium alloy Ti–6.5Al–5.3Zr–2.2Sn–0.6Mo–0.5Nb–0.75Si in the condition after welding with preheating to 400 °C, led to the conclusion that the microhardness level in different areas of the welded joints is also very heterogeneous (Figure 11). The highest microhardness values are recorded in the weld metal at the level of 3000 MPa. The lowest level was found in the base metal at 2400 MPa.

To ensure a uniform distribution of microhardness and a homogeneous microstructure in different areas of welded joints of heat-resistant titanium alloy Ti–6.5Al–5.3Zr–2.2Sn–0.6Mo–0.5Nb–0.75Si, EBW with preheating to 400 °C and LHT at 750 °C for 10 min was used (mode 3, see Table 1).

Analysis of the produced welded joint microstructure (Figure 12) indicates that a typical dendrite structure of cast metal forms in the weld zone. It is dense, and no defects such as porosity, cracks or nonmetallic inclusions were revealed in it. The size of dendrite branches on the section surface is equal to 100–150 μm. The boundaries of the dendritic areas do not contain any excess phase precipitates and are not the material weak points. It is important that rapid cooling of the molten weld metal results in formation in the dendritic areas of rather dispersed packages of Widmanstatten morphology with package size (by the size of the largest platelets) in the range from 20 to 50 μm, which is close to the characteristics of dispersion of the base metal structure.

Smaller primary β-grains of 100–150 μm size (Figure 12, *a*) form in the weld metal than in the case of simple EBW with grains of 300–400 μm size. In addition to equiaxed primary grains localized near the axis, the weld metal also contains non-equiaxed grains, elongated in the direction of the heat removal (Figure 12, ***b)***. The intragranular structure of the weld metal is of lamellar type (Figure 12, *c*), platelet width being 1–2 μm. Dispersed particles 1 μm in size or less are located both along the platelet boundaries, and in the spaces between

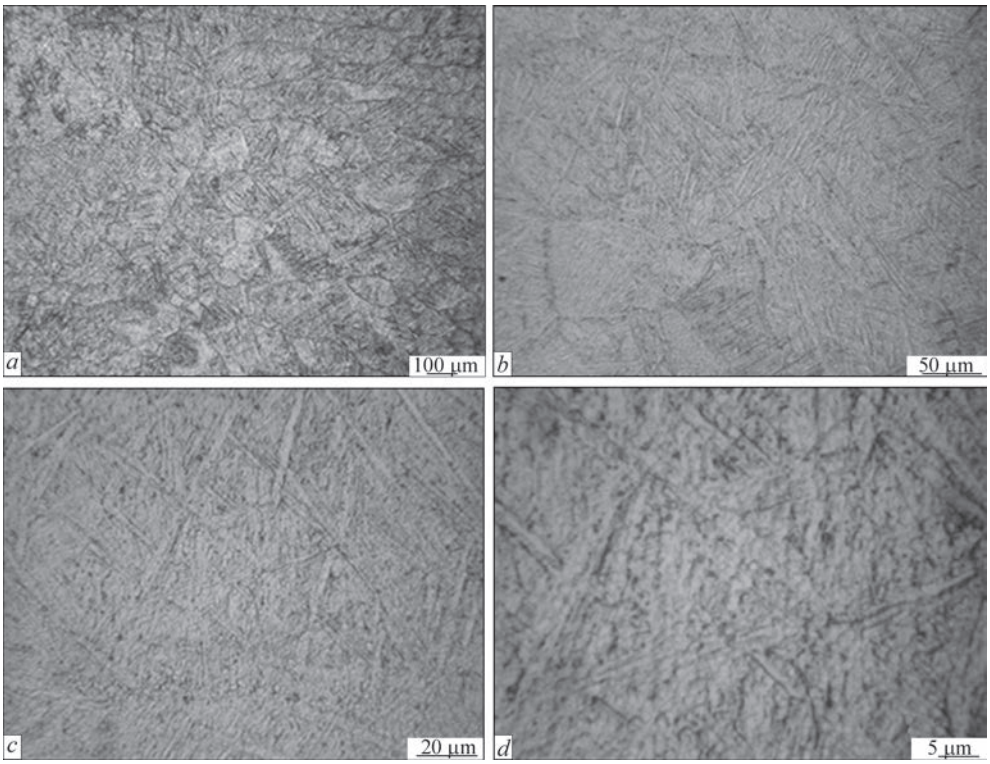

Figure 12. Microstructure of weld metal of welded joint of heat-resistant Ti–6.5Al–5.3Zr–2.2Sn–0.6Mo–0.5Nb–0.75Si alloy, made by EBW with LHT at 750 °C

them (Figure 12, *d*). It is obvious that the dispersed particles are titanium silicides (Ti_5Si_3), which form in the alloy being welded, due to its increased silicon content, which is higher than its solubility in α-titanium.

The structure of HAZ metal of the samples with different heat treatment is given in Figure 13. Microstructure analysis shows that the HAZ preserves the main morphological and dimensional characteristics of the base metal (Figure 13, *a*).

No differences were observed in the structure after application of different heat treatment modes. A clearer definition of α-phase platelets due to β-phase

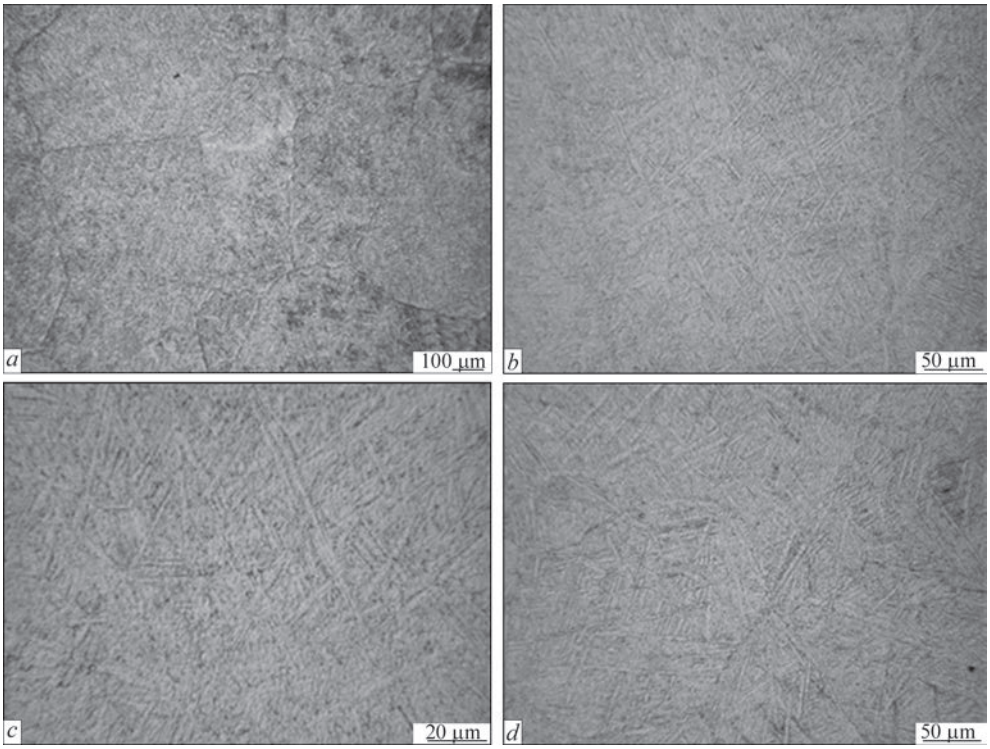

Figure 13. Microstructure of HAZ metal of welded joint of heat-resistant Ti–6.5Al–5.3Zr–2.2Sn–0.6Mo–0.5Nb–0.75Si alloy, made by EBW with LHT at 750 °C

precipitation along the platelet boundaries and, possibly, formation of intermetallic particles, is seen in the HAZ structure (Figure 13, *c*). Dispersed particles 1 μm in size and less are located both in the fusion zone near the HAZ along platelet boundaries, and in the spaces between the platelets (Figure 13, *d*). Grain size in the HAZ metal is equal to 200–500 μm.

Although application of different heat treatment modes did not lead to any significant changes in the welded joint microstructure, the difference in the intensity of structure etching and in the amount of β-phase on the boundaries of α-phase platelets suggests that the mechanical properties of the joints could change under the thermal impact, as a result of relaxation of mechanical stresses and formation of excess phases.

Thus, the technology of electron beam welding of heat-resistant Ti–6.5Al–5.3Zr–2.2Sn–0.6Mo–0.5Nb–0.75Si alloy with LHT allows producing a tight joint without porosity, cracks or nonmetallic inclusions. At EBW without heating a relatively fine-grained weld structure forms and there is no HAZ microstructure coarsening.

DISCUSSION OF THE RESULTS

It should be noted that a considerable coarsening of the weld structure and increase of grain size in the HAZ are observed in EBW with preheating to 400 °C. Therefore, use of just heating for EBW of heat-resistant Ti–6.5Al–5.3Zr–2.2Sn–0.6Mo–0.5Nb–0.75Si alloy is not rational. It can be explained by an undesirable range of cooling rates at EBW with only the preheating. So, the cooling rate in the HAZ in EBW without preheating or LHT is equal to 88–131 °C at 700–800 °C, the cooling rate in the HAZ in EBW with preheating is 30–50 °C/s, and the cooling rate in EBW with preheating to 400 and LHT at 750 °C is 8.3–8.8 °C/s.

Determination of microhardness distribution in the welded joint of heat-resistant titanium alloy Ti–6.5Al–5.3Zr–2.2Sn–0.6Mo–0.5Nb–0.75Si produced by EBW

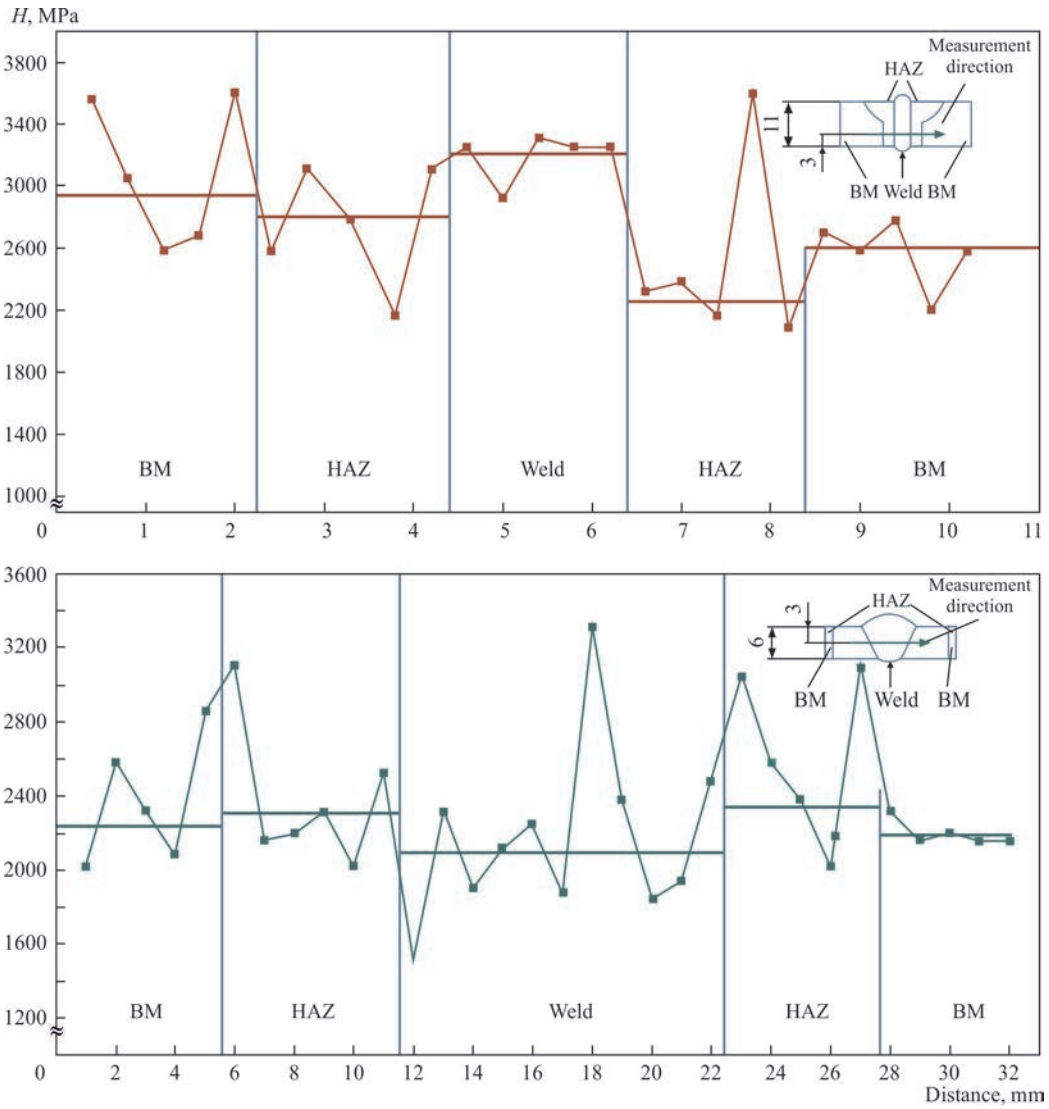

Figure 14. Microhardness distribution in EB welded joint of heat-resistant titanium alloy Ti–6.5Al–5.3Zr–2.2Sn–0.6Mo–0.5Nb–0.75Si in the condition after LHT at 750 °C for 10 min (*a*), after annealing at 850 °C for 1 h (*b*)

Table 2. Mechanical properties of EB welded joints of heat-resistant titanium pseudo-α-alloy Ti–6.5Al–5.3Zr–2.2Sn–0.6Mo–0.5Nb–0.75Si, in as-welded condition

Mode	T_{pr}, °C	T_{LHT}, °C	σ_t, MPa	$\sigma_{0.2}$, MPa	δ_s, %	*KCV*, J/cm^2
As-annealed base metal	–	–	1027	996	2.7	13.9
EBW, mode 1	–	–	996	901	–	12.3
EBW with preheating, mode 2	400	–	910	840	–	17.9
EBW with LHT, mode 3	–»–	750	1041	1012	–	17.4

with LHT suggested that microhardness distribution in different areas of the welded joint is still nonuniform (Figure 14, *a*). Note that the proposed LHT widened the welded joint HAZ. The width of base metal area, where an increase in microhardness values to 3000 MPa occurred, expanded to that of the LHT zone, in this case to 30 mm. Furnace annealing should be used to achieve a completely homogeneous metal of the weld, HAZ and base metal. So, vacuum annealing of the welded joints at the temperature of 850 °C intensified the diffusion processes, which resulted in alloying element redistribution in the welded joint structure. Microhardness distribution in EB welded joint of heat-resistant titanium alloy Ti–6.5Al–5.3Zr–2.2Sn–0.6Mo–0.5Nb–0.75Si in as-annealed condition showed that the microhardness level in different areas of the welded joints is homogeneous, being at the level of base metal microhardness of 2100–2300 MPa.

Determination of mechanical properties of EB welded joint of heat-resistant titanium pseudo-α-alloy Ti–6.5Al–5.3Zr–2.2Sn–0.6Mo–0.5Nb–0.75Si led to the conclusion that the lowest strength values in as-welded condition are demonstrated by joints made by EBW with preheating to 400 °C, and they are equal to 910 MPa (Table 2) or 88 % of BM strength after annealing. The strength values are the highest in welded joints produced by EBW with LHT at 750 °C (mode 3, see Table 1) and they are equal to 1041 MPa, which is at the level of BM strength. Welded joints made by simple EBW without application of additional technological measures, have medium values of strength at the level of 996 MPa or 97 % of BM strength.

The main difference of welded joints of heat-resistant titanium pseudo-α-alloy Ti–6.5Al–5.3Zr–2.2Sn–0.6Mo–0.5Nb–0.75Si is the fact that application of just the preheating leads to coarsening of the welded joint microstructure and deterioration of their mechanical properties, while for pseudo-β-alloys EBW in combination with preheating allows producing a finer microstructure of the welded joints, increasing the welded joints strength and ensuring equal strength of the welded joints to base metal [24].

Thus, EBW application in combination with LHT when producing welded joints of heat-resistant titanium pseudo-α-alloy Ti–6.5Al–5.3Zr–2.2Sn–0.6Mo–0.5Nb–0.75Si allows making welded joints equal in strength to the base metal, and additional furnace annealing should be used to ensure a homogeneous structure in all the zones of the welded joint, including the HAZ.

CONCLUSIONS

1. Investigations of the structure of welded joints of heat-resistant titanium alloy Ti–6.5Al–5.3Zr–2.2Sn–0.6Mo–0.5Nb–0.75Si revealed that application of EBW with LHT at 750 °C leads to reduction of the size of packages with Widmanstatten morphology from 50–100 to 20–50 μm and increase in welded joint strength from 996 to 1041 MPa.

2. EBW of heat-resistant Ti–6.5Al–5.3Zr–2.2Sn–0.6Mo–0.5Nb–0.75Si alloy with application of just the preheating leads to a significant coarsening of the weld structure and to occurrence of the grain growth processes in the HAZ with larger packages of Widmanstatten morphology of 50–100 μm size forming in the metal, which is greater than in the base metal structure, and to deterioration of the welded joint mechanical structure.

3. Determination of the mechanical properties of the welded joints of heat-resistant titanium pseudo-α-alloy Ti–6.5Al–5.3Zr–2.2Sn–0.6Mo–0.5Nb–0.75Si produced by EBW with application of additional technological measures, such as preheating and local heat treatment, suggests that welded joints made by EBW with LHT at 750 °C have the greatest strength values, equal to 1041 MPa, which is at the level of base metal strength.

4. A technological process of EBW of heat-resistant titanium pseudo-α-alloy Ti–6.5Al–5.3Zr–2.2Sn–0.6Mo–0.5Nb–0.75Si with LHT is proposed, which envisages preheating of the welded joints to the temperature of 400 °C and LHT at 750 °C, which ensures formation of a highly homogeneous fine microstructure in welded joints and provides strength values of the joints of 1041 MPa in as-welded condition, which is at the level of base metal strength.

REFERENCES

1. (2003) *Titanium and titanium alloys. Fundamentals and applications*. Ed. by Leyens and M. Peters. Weinheim, WILEY-VCH Verlag GmbH & Co, KGaA.

2. Ertuan Zhao, Shichen Sun, Yu Zhang (2021) Recent advances in silicon containing high temperature titanium alloys. *J. of Materials Research and Technology*, **14**, September–October, 3029–3042.
3. Firstov, S., Kulak, L., Miracle, D. et al. (2001) *Proc. of 8th Annual Inter. Conf. on Composites Engineering ICCE/8, Aug. 5–11, Tenerife, Canary Islands, Spain*. Ed. by D. Hui, 245–246.
4. Saha, R.L., Nandy, T.K., Misra, R.D.K. (1991) Microstructural changes induced by ternary additions in a hypo-eutectic titanium-silicon alloy. *J. of Materials Sci.*, **26**, 2637–2644.
5. Firstov, S.O., Kulak.L.D., Kuzmenko, M.M., Shevchenko, O.M. (2018) Alloys of Ti–Al–Zr–Si system for high temperature operation. *Fiz.-Khimich. Mekhanika Materialiv,* 54(**6**), 30–35 [in Ukrainian].
6. Shichen Sun, Hongze Fang, Yili Li et al. (2023) Formation mechanism and effect on the mechanical properties of TiSi phase for Ti–5Al–5Mo–5Cr–3Nb–2Zr alloyed by silicon. *J. of Alloys and Compounds*, 938(**25**), 168510.
7. Hong Feng, Shuzhi Zhang, Fan Peng et al. (2023) Enhanced mechanical properties of a near-α titanium alloy by tailoring the silicide precipitation behavior through severe plastic deformation. *Materials Sci. and Eng*., 880(**26**), 145356.
8. Wu, T., Beaven, P., Wagner, R. (1990) The Ti_3 (Al, Si) + Ti_5 $(Si, Al)_3$ eutectic reaction in the Ti–Al–Si System. *Scripta Metallurgica*, **24**, 207–212.
9. Bulanova, M., Tretyachenko, L., Golovkova M. (1997) Phase equilibria in the Ti-rich corner of the Ti–SiAl system. *Zeitschrift Metallkunde*, **88**, 257–265.
10. Mazur, V.I., Taran, Y.N., Kapustnikova, S.V. et al. (1994) *Titanium matrix composites*. US Pat. No. 5366570, Nov. 22.
11. Hayat, M.D., Singh, H., He, Z., Cao, P. (2019) Titanium metal matrix composites: An overview. Pt A. *Composites*, 121418–121438. DOI: https://doi.org/10.1016/j.compositesa.2019.04.005
12. Akhonin, S.V., Vrzhizhevsky, E.L., Belous, V.Yu., Petrichenko, I.K. (2017) Influence of preheating parameters and local heat treatment on structure and properties of dispersion-strengthened joints of silicon-containing titanium alloys made by electron beam welding. *The Paton Welding J*., **7**, 43–47. DOI: https://doi.org/10.15407/tpwj2017.07.09
13. Li, Y., Wang, H., Han, K. et al. (2017) Microstructure of Ti–45Al–8.5Nb–0.2W–0.03Y electron beam welding joints. *J. of Materials Proc. Technology*, **250**, 401–409.
14. Kurashkin, S.O., Tynchenko, V.S., Seregin, Y.N. et al. (2020) The model of energy distribution during electron beam input in welding process. *J. of Physics: Conf. Series*, 1679(**4**), 042036. IOP Publishing.
15. Seregin, Y.N., Murygin, A.V., Laptenok, V.D., Tynchenko, V.S. (2018) Modeling of electron beam distribution in electron beam welding. *IOP Conf. Series: Materials Sci. and Eng*., 450(**3**), 032036. IOP Publishing.
16. Liu, P., Zhang, G.M., Zhai, T., Feng, K.Y. (2017) Effect of treatment in weld surface on fatigue and fracture behavior of titanium alloys welded joints by vacuum electron beam welding. *Vacuum*, **141**, 176–180.
17. Schmidt, P. (2019) Vorteile und Besonderheiten: Elektronen Strahlschweißen von Titanbauteilen. *Der Praktiker*, **4**, 158–162.
18. Zhao, X., Lu, X., Wang, K., He, F. (2022) Investigation on the microstructure and mechanical properties of Ti6Al4V titanium alloy electron beam welding joint. In: Proc. of the Institution of Mechanical Eng., Pt C. *J. of Mechanical Eng. Sci*., 236(**6**), 2957–2966.
19. Hansen, M., Kessler, H.D., McPherson, D.J. (1952) *Transact. Amer. Soc. Met*., **44**, 518.
20. Akhonin, S., Hryhorenko, G., Berdnikova, O. et al. (2019) Fine structure of heat-resistant titanium alloys welded joints. In: *Proc. of 9th Inter. Conf. on Nanomaterials: Applications & Properties (NAP-2019). September 15–20, Odessa, Ukraine*. Pt 1., Sumy, Sumy State University, 1–5.
21. Pederson, R., Niklasson, F., Skystedt, F., Warren, R. (2012) Microstructure and mechanical properties of friction- and electron-beam welded Ti–6Al–4V and Ti–6Al–2Sn–4Zr–6Mo. *Materials Sci. and Eng., A*, **552**, 555–565.
22. Akhonin, S.V., Berezos, V.O., Pikulin, O.M. et al. (2022) Producing high-temperature titanium alloys of Ti–Al–Zr–Si–Mo–Nb–Sn system by electron beam melting. *Suchasna Elektrometal*., **2**, 3–9. DOI: http://doi.org/10.37434/sem2022.02.01
23. Akhonin, S.V., Severin, A.Yu., Pikulin, O.M. et al. (2022) Structure and mechanical properties of high-temperature titanium alloy of Ti–Al–Zr–Si–Mo–Nb–Sn system after deformation treatment. *Suchasna Elektrometal*., **4**, 43–48. DOI: http://doi.org/10.37434/sem2022.04.07
24. Akhonin, S.V., Belous, V.Yu., Selin, R.V. et al. (2018) Electron beam welding and heat treatment of welded joints of high-strength pseudo-β titanium alloy VT19. *The Paton Welding J*., **7**, 10–14. DOI: http://dx.doi.org/10.15407/tpwj2018.07.02

ORCID

S.V. Akhonin: 0000-0002-7746-2946,
V.Yu. Bilous: 0000-0002-0082-8030,
E.L. Vrzhyzhevskyi,: 0000-0001-8651-8510,
R.V. Selin: 0000-0002-2990-1131,
I.K. Petrychenko: 0009-0008-1097-7137,
S.L. Schwab: 0000-0002-4627-9786

CONFLICT OF INTEREST

The Authors declare no conflict of interest

CORRESPONDING AUTHOR

V.Yu. Bilous
E.O. Paton Electric Welding Institute of the NASU
11 Kazymyr Malevych Str., 03150, Kyiv, Ukraine.
E-mail: belousvy@gmail.com

SUGGESTED CITATION

S.V. Akhonin, V.Yu. Bilous, E.L. Vrzhyzhevskyi, R.V. Selin, I.K. Petrychenko, S.L. Schwab, S.L. Antonyuk (2025) Structure and properties of welded joints of heat-resistant titanium alloy of Ti–Al–Zr–Sn–Mo–Nb–Si system produced by electron beam welding. *The Paton Welding J*., **2**, 13–23.
DOI: https://doi.org/10.37434/tpwj2025.02.03

JOURNAL HOME PAGE

https://patonpublishinghouse.com/eng/journals/tpwj

Received: 11.10.2024
Received in revised form: 25.11.2024
Accepted: 31.03.2025

DOI: https://doi.org/10.37434/tpwj2025.02.04

PRODUCING A WÜSTITE MELT BY THERMAL DECOMPOSITION OF HEMATITE PELLETS WITH ARGON PLASMA

V.O. Shapovalov[1], **V.G. Mogylatenko**[1,2], **M.V. Karpets**[1,2], **R.V. Kozin**[1]

[1]E.O. Pat Electric Welding Institute of the NASU
11 Kazymyr Malevych Str., 03150, Kyiv, Ukraine
[2] National Technical University of Ukraine "Igor Sikorsky Kyiv Polytechnic Institute"
37 Prosp. Beresteiskyi, 03056, Kyiv, Ukraine

ABSTRACT

Reducing CO_2 emissions is of paramount importance, in order to address the issues of global warming. The negative contribution of Ukrainian metallurgists to atmospheric pollution over the past 20 years amounted to about 1 bln t of carbon dioxide by the year 2020. The solution can be found in the transition to the production of "green steel", i.e. steel manufactured from direct hydrogen-based reduction iron. Under the conditions of applying plasma heating, high temperatures lead to a rapid melting of pellets, thermal decomposition of oxides occurs, and a reducing agent (hydrogen) is activated. Decomposition of oxides during the heating and melting process accelerates the overall process of pellet reduction to wüstite. And only in that moment, the use of hydrogen for reduction of iron and its deoxidation becomes justified. It was established that forming of a wüstite melt is possible without the use of a reducing agent during plasma melting in an argon atmosphere.

KEYWORDS: direct reduction, pellets, thermal decomposition, kinetics, magnetite melt, dilution with iron, wüstite

INTRODUCTION

Steelmaking is a large source of greenhouse gases. In 2022, 1.91 t of CO_2 were emitted per t of steel. The production of 1 t of steel, depending on the smelting method, emits 0.4–2.4 t of CO_2. The CO_2 emissions intensity and power consumption are calculated based on the weighted average steel production using different schemes: blast furnace — oxygen converter, blast furnace — electric arc furnace and direct reduced iron production in an arc furnace [1].

In 2023, the top 10 polluting countries increased their industrial emissions to a record 24.5 bln t of CO_2 compared to 23.9 bln t (+2.5 %) in 2022. The three major polluters were China, the United States and India, which together accounted for more than 53 % of all industrial emissions. China emitted a record 11.2 bln t of CO_2, which is an increase of 642 mln t compared to 2022 and the highest annual growth since 2011 [2, 3]. As for Ukraine, according to Ukrmetalurgprom, its metallurgical enterprises produced 6.19 mln t of steel in 2022, and 6.23 mln t in 2023. Experts predict that Ukrainian steelmakers will be able to increase steel production to 7–8 mln t. It should be noted that this forecast can be considered very optimistic, and the main reason here is the loss of a number of enterprises in Donetsk region, as well as the forced shutdown of a number of other enterprises [4, 5]. If we assume an average CO_2 emission of 1.4 t per t of steel, Ukrainian metallurgical plants will emit at least 8.7 mln t annually in 2022 and 2023, and over the 20 years from 2000 to 2020, 663.1 mln t of steel were smelted [6] and, even according to underestimates, about 1 bln t of carbon dioxide were emitted. Such is Ukraine's negative contribution to air pollution.

Today, it is widely recognised that reducing CO_2 emissions is of paramount importance in combating global warming. The gas accumulated in the atmosphere absorbs and stores heat in the infrared range. A CO_2 concentration of one part per mln (1 ppm) is equivalent to adding approximately 7.8 Gt of carbon dioxide to the atmosphere [7].

Today, most blast furnaces in Europe are over 25 years old, and only a few of them have undergone modernization [2, 8]. This opens up the possibility of replacing some of the production capacities with a more updated steelmaking technology using direct reduction of iron ore pellets or ore with hydrogen, followed by smelting in various types of furnaces.

Transition to green steel production faces not only technological and design challenges. One of the most important areas of works to reduce carbon emissions is the production of hydrogen on a production scale, which is directly related to the development and launch of powerful electrolysers and the generation of a significant amount of green electricity. According to estimates given in [2], electrolysers will consume approximately 296 TWh of electricity per year. According to the online edition of "Ekonomichna Pravda", electricity production in 2021 was 156.56 TWh [9] (156.56 bln kWh), which is half as much as the electricity consumption by electrolysers.

Technologically, there are two ways of direct iron reduction from oxides by hydrogen. The first method,

which is the most developed and the one which uses existing production capacities, is the production of sponge iron using a hydrogen or a hydrogen-carbon environment. The use of natural gas or adding carbon to the hydrogen atmosphere have a positive effect on the reduction kinetics, but it does not completely eliminate carbon dioxide emissions. Reduction using ammonia as a reducing agent can give positive results, in particular, when reducing iron in the solid state [10, 11]. According to thermodynamic calculations, the degree of metallization is expected to improve significantly by increasing the amount of ammonia in the gas atmosphere, reaching 97 % when using 20 % of ammonia.

The method of hydrogen reduction and production of iron in the form of a sponge is not perfect. Its main disadvantages are the long time of reduction and the need to use separate equipment for reduction and melting. It is possible to combine these two processes by using high-temperature hydrogen plasma as an energy source for reduction and melting.

STATE-OF-THE-ART OF THE ISSUE

Plasma melting has a number of advantages over electric arc melting. The main advantage is that the process of iron reduction is intensified due to high plasma temperatures (hydrogen activation, acceleration of mass transfer, production of reduced iron in a liquid state and the possibility of melt alloying without intermediate production of iron ingots with their subsequent remelting). Also, an equally important advantage is a decrease in specific electricity consumption. For example, depending on various factors, its total specific power consumption for an electric arc furnace ranges between 500 and 700 kWh, and for a plasma arc furnace it is approximately from 350 to 550 kWh per 1 t of melted steel [12].

Hydrogen is an excellent reducing agent at both low and high temperatures. Moreover, when hydrogen molecules transfer into the plasma state, they can receive additional internal energy of oscillating and rotational motion, and transfer into atomic and ionised states. Free electrons, phot and other elementary particles are observed in the plasma. Their ratio depends on the plasma temperature, which can reach tens of thousands of degrees. However, the temperature of the liquid metal in plasma-arc melting is much lower and in the plasma plume action zone is about 3000–4000 K [13–15]. As a rule, excited molecules and atomic hydrogen interact with metal under real temperature conditions. Due to their high reactivity, the reduction of iron oxides occurs under much more favourable thermodynamic conditions than the reduction with hydrogen gas alone. PAM provides and improves the kinetic conditions for the interaction of hydrogen with oxides, which at solid state temperatures often determine the rate of reduction.

In the production of iron by direct reduction from oxides using hydrogen plasma, the first step is the melting of the charge (Fe_2O_3 hematite). Roughly in this period it is not necessary to use hydrogen as a reducing agent and the melting can be carried out in an inert gas (argon). This is associated with the following causes.

From the diagram of the Fe–O system shown in Figure 1 according to [16], it follows that at a temperature of 1730 K in an atmosphere of pure oxygen or at 1663 K in air, hematite dissociates with the formation of magnetite (Fe_3O_4) and oxygen, i.e., even before the melt is produced. The use of an inert atmosphere or vacuum accelerates this process, which occurs according to the reaction:

$$6Fe_2O_3 = 4Fe_3O_4 + O_2. \quad (1)$$

Thus, the oxygen content in the oxide decreases from 30.06 to 28.08 % at 1856 K. Hence, the primary reduction of the lower oxide from the higher oxide occurs without hydrogen consumption and without

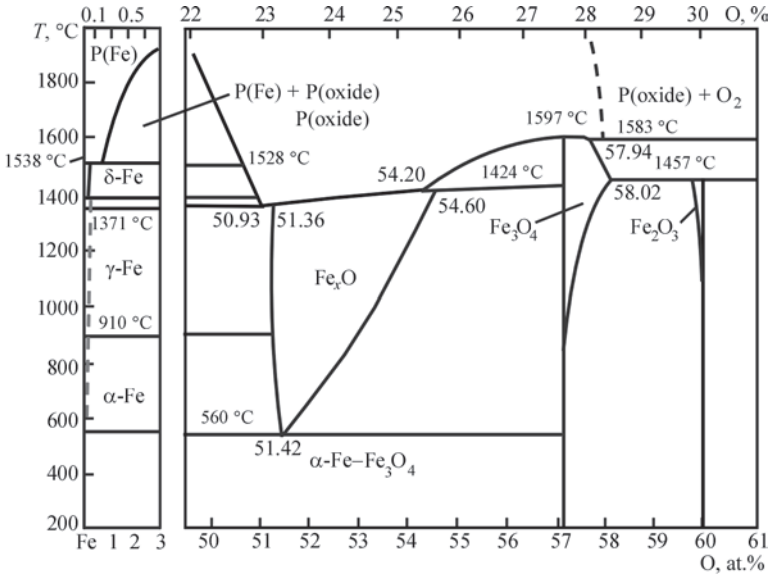

Figure 1. State diagram of the Fe–O system according to [16]

additional energy consumption directly for the reduction, since it coincides with the process of heating hematite to its melting point.

The obtained magnetite has the stoichiometric formula Fe_3O_4, which can be written as ($FeO{\cdot}Fe_2O_3$). The subsequent reaction already requires the presence of a reducing agent, in our case hydrogen, and can be written as:

$$Fe_3O_4 + H_2 = 3FeO + H_2O \quad (2)$$

or

$$FeO{\cdot}Fe_2O_3 + H_2 = 3FeO + H_2O. \quad (3)$$

Thermodynamic calculations show that reaction (3) occurs with a large negative change in free energy [17]. Since the plasma-arc furnace is a flow reactor, from which gaseous moisture is removed either by cleaning the gas phase during its recirculation or by continuous evacuation to the surrounding atmosphere, the reaction can proceed even until the oxide is completely used and reduced iron is obtained. The duration of the iron reduction from wüstite is determined by the kinetic characteristics of the reaction.

The next stage of iron reduction from the melt of wüstite can be described by the reaction:

$$FeO_{(max\ O)} + H_2 \rightarrow FeO_{(min\ O)} + H_2O. \quad (4)$$

Here, a fairly quick running of the reduction process is ending. Reaction:

$$FeO_{(min\ O)} + H_2 \rightarrow Fe_{(max\ O)} + H_2O \quad (5)$$

is proceeding very slowly in the temperature range from melting to 3147 K. The change in the free energy of the reaction of iron reduction from the wüstite melt in this temperature range has a small negative value: from –2454 to –3142 J/mol, and the logarithm of the equilibrium constant varies from 0.0568 to –0.0191 [14].

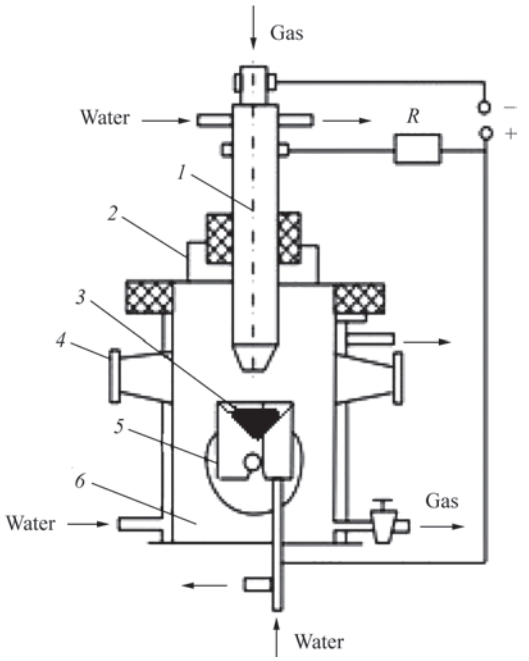

Figure 2. Scheme of the experimental plasma-arc installation [15]: *1* — plasmatron; *2* — cover; *3* — molten sample; *4* — observation device; *5* — opening mould; 6 — sealed chamber

The next step is deoxidation of iron with hydrogen. It should be noted that hydrogen deoxidation is very slow according to the data presented in [18]. The final oxygen content of 0.001 % was reached after 0.5 h during deoxidation of the metal containing only 0.035 % of oxygen with carbon under melting conditions. Hydrogen treatment under the same conditions after 4 h led to a decrease in oxygen content of only 0.0015 %, i.e. it was more than 8 times slower.

Thus, before addressing the issue of overcoming the kinetic obstacles during deoxidation of iron melt, it is necessary to produce a melt of wüstite and then reduced iron with the maximum amount of dissolved oxygen at the lowest consumption. There are at least two methods of producing a wüstite melt. These are reduction of the oxide melt to FeO or dilution of the magnetite melt with iron, i.e. the reaction [19]:

$$Fe_3O_4 + Fe = 4FeO. \quad (6)$$

The change in the free energy of the reaction (6) ranges from –32174 to –63752 J/mol at temperatures from melting to 3000 K. The equilibrium constant varies within 8–13 in the same temperature range.

The latter method is considered in this paper.

RESEARCH PROCEDURE

MELTING PROCESS

To produce oxide melts, plasma-arc melting was used, the equipment for which was developed at the E.O. Pat Electric Welding Institute [15]. It allows melting under the condition, when the entire surface of the liquid pool is covered with a plasma plume. The sealed chamber in which the melting is carried out is cooled by water, it has a plasma arc observation system, a plasmatron adjustment system and a gas pressure regulation and control system.

After the liquid pool is melted and held in the atmosphere of plasma-forming gas, the high-temperature state of the melt is fixed in a water-cooled metal mould. The equipment scheme is shown in Figure 2.

The melting procedure is as follows. A sample weighing 5.5–7.5 g is loaded into the melting chamber on a closed mould. A vacuum of 0.133 Pa is created in the chamber and then the chamber volume is filled with an inert plasma-forming gas (argon) to a pressure of 83.36–98.07 kPa. Subsequently, the plasmatron arc is ignited. The pellet sample is heated and melted, and then the melt is held under plasma heating. At the end of the holding time, the sample is rapidly crystallized in a copper water-cooled mould. 10 melts of pellets were performed with a holding time of 150 s and pro-

Table 1. Initial data for melts and results obtained for dilution of the melt with iron

Calculation for the experiment								
Number of melting	1	2	3	4	5	6	7	8
Weight of Fe_3O_4, g	4.021	2.913	2.673	3.244	3.826	3.826	3.821	3.101
Weight of iron, g	0	0.110	0.120	0.630	0.760	0.940	1.120	0.920
Fe/Fe_3O_4	0	0.038	0.045	0.194	0.199	0.246	0.293	0.297
Result of the experiment								
Weight of Fe_3O_4, g	57.11	23.25 20.32	25.86 17.25	20.1 20.08	31.06 29.45	17.39 17.14	0 0	0 0
Weight of FeO, %	42.89	76.75 79.68	74.14 82.75	79.9 79.92	68.95 70.55	82.61 82.86	100 100	100 100

duced samples were averaged according to the chemical composition, which is given below:

Fe_3O_4 — 52.51 %, FeO — 24.01 %,
Fe_2SiO_4 — 21.80 %, Fe_2O_3 — 1.42 %.

Thus, each subsequent experiment was carried out with the same material. The composition of iron silicide was converted to FeO and a mixture of the two components Fe_3O_4 and FeO, which amounted to 100 %, was the initial point. A certain amount of iron was added to the oxides, which was calculated in advance. The calculation data are shown in Table 1.

X-ray diffraction studies of the samples were carried out using a DRON UM-1 diffractometer in a monochromatic copper K_α radiation by the step scanning method (U = 35 kV; I = 25 mA, exposure time at a point is 5 s, step is 0.05°, output slits are 1×12 mm). The obtained X-ray patterns were decoded using PowderCell 2.4, a software for full-profile analysis of X-ray spectra from a mixture of polycrystalline phase components. The profiles of diffraction maxima were approximated by the Pseudo-Voigt function. The international crystallographic database PCPDFWIN (1973) was used for the calculations.

The examples of the obtained X-ray spectra of samples 2, 4, 6, and 8, respectively, are shown in Figure 3. After recalculation, the amount of magnetite and wüstite corresponds to the data in Table 1.

EXPERIMENTAL RESULTS AND DISCUSSION

In [19], the study of the kinetics of pellet decomposition was limited to 150 s for technical reasons. It was decided to extend the melting time to test the possibility of transferring the melt to a homogeneous state corresponding to the wüstite without dilution with iron.

The studies (Figure 4) have shown that with an increase in holding time, decomposition continues for at least 360 s.

The studies were carried out both with continuous holding of the melt for 360 s, as well as with periodic crystallization and subsequent heating. In other words, the sample was heated for 30 s until melting, held for 60 s and crystallized. Then the cycle was repeated. The number of such cycles was 6. Thus, the sample was in the liquid state for 360 s and in the heating state for 180 s. The results for these two melting schemes were slightly different. Thus, when the melt

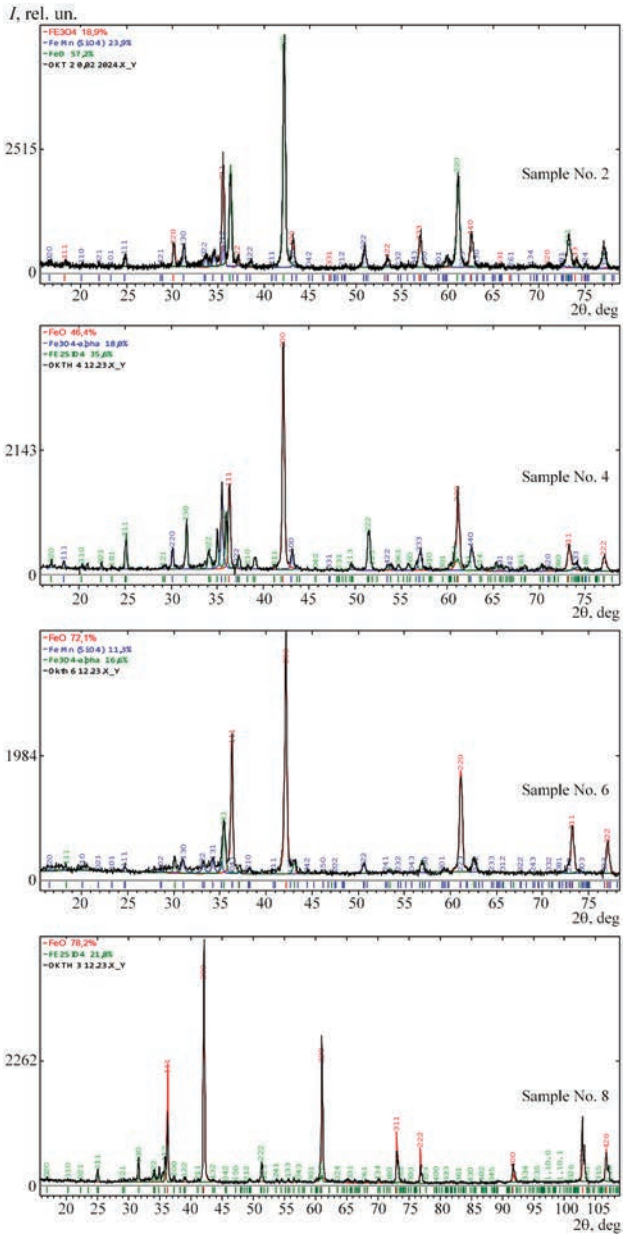

Figure 3. Examples of X-ray spectra of melt samples 2, 4, 6 and 8 (see Table 1)

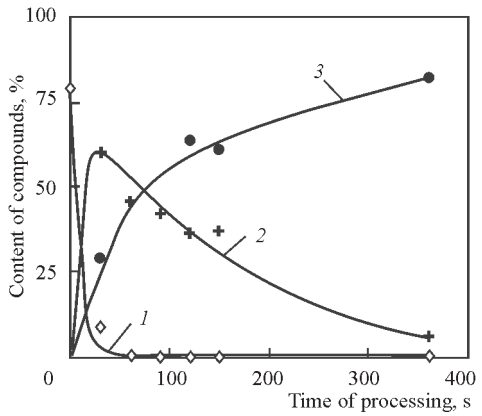

Figure 4. Change in the content of oxides in a rapidly crystallized melt after different holding times at PAM in an argon atmosphere: *1* — Fe_2O_3; *2* — Fe_3O_4; *3* — FeO

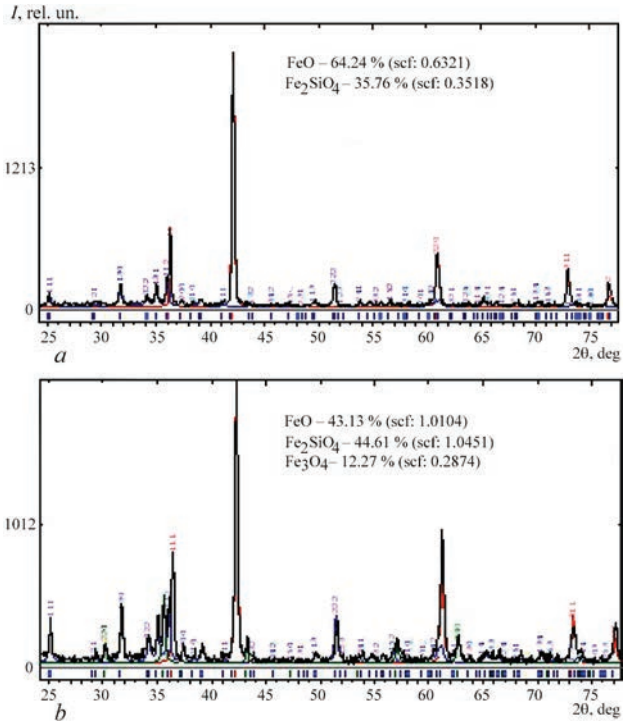

Figure 5. X-ray spectra of samples at step and continuous holding of the melt: *a* — 6 cycles of 60 s, *b* — 1 cycle of 360 s

is held continuously for 6 min under plasma heating, the wüstite content grows to 74.6 %, and magnetite decreases to 12.3 % (Figure 5, *b*). The rest of content is SiO_2. During the step heating and crystallization, it is possible to remove oxygen from the solid oxide system and the melt due to the additional time spent on repeated heating, and magnetite disappears (Figure 5, *a*). Thus, we obtain a melt of wüstite, although with a certain increase in power consumption.

The main negative conclusion is a significant decrease in the rate of decomposition of the Fe_3O_4 melt to FeO with an increase in the holding time of the oxide melt in the liquid state, even at PAM. Especially if we take into account the size factor when changing from small laboratory weighed portions to real industrial metal masses.

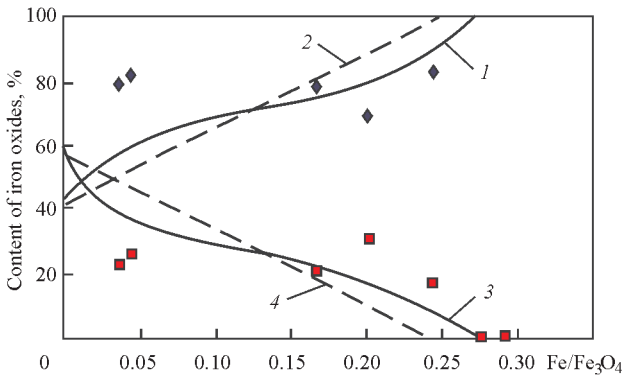

Figure 6. Change in the composition of the oxide melt depending on the amount of iron added to the magnetite melt: *1*, *2* — wüstite content; *3*, *4* — magnetite content; *1*, *3* — experiment; *2*, *4* — theoretical calculation

As for the other method, the theoretical calculation for the initial values of the components of reaction (6) (see Table 1) showed that when iron is added to the magnetite melt, the dependence of the content of iron oxides on the amount of iron, with respect to the Fe/Fe_3O_4 ratio, is linear (Figure 6) and is described by the following equations.

Change in FeO content (theoretical):

$$(\mathrm{FeO}) = 237\frac{\mathrm{Fe}}{\mathrm{Fe_3O_4}} + 42.9.$$

Change in Fe_3O_4 content (theoretical):

$$(\mathrm{Fe_3O_4}) = -237\frac{\mathrm{Fe}}{\mathrm{Fe_3O_4}} + 57.1.$$

The Fe/Fe_3O_4 ratio being 0.241, this means that all magnetite, according to reaction (6), is converted to wüstite.

The difference between the theoretical and experimental dependences is most probably associated with the use of small weighing portions of material during the experiments. However, the final difference between the theoretical value of the ratio of the initial reaction components being 0.241 and the experimental value being 0.293 is 0.052 or approximately 20 % in absolute values, which can be considered acceptable.

CONCLUSIONS

1. It was found that at continuous holding of the melt in argon plasma under experimental conditions for 360 s, the content of wüstite grows to 74.6 %, and magnetite decreases to 12.3 %. After 6 cycles of periodic crystallization of the melt and subsequent melting with a holding time of 60 s, magnetite completely disappears and a melt of wüstite FeO_{max} is formed.

2. A significant decrease in the rate of decomposition of liquid Fe_3O_4 to FeO with an increase in the time of continuous holding of the oxide melt in the liquid state even at plasma-arc heating is observed.

3. When adding iron to the magnetite melt, the theoretical dependence of the iron oxide content on

the Fe/Fe_3O_4 ratio is described by linear dependences. The experimental values differ from the theoretical ones by 20 %, but allow using this method to produce a wüstite melt.

REFERENCES

1. *World steel in figures*. https://worldsteel.org/steel-topics/statistics/world-steel-in-figures/
2. Kolisnichenko, V. *Carbon emissions in metallurgy will be reduced by 30 % by 2050 — Woodmac* [in Ukrainian]. https://gmk.center/ua/news/vybrosy-ugleroda-v-metallurgii-k-2050-godu-sokratyatsya-na-30-woodmac-2/
3. Kolisnichenko, V. *10 biggest polluting countries emitted record amount of CO_2 in 2023* [in Ukrainian]. https://gmk.center/ua/news/10-najbilshih-krain-zabrudnjuvachiv-u-2023-roci-vikinuli-rekordnu-kilkist-so2/
4. *In 2024 steel production in Ukraine will amount 7–8 mln t according to experts.* https://delo.ua/ru/industry/v-2024-godu-vyplavka-stali-v-ukraine-sostavit-7-8-mln-tn-429900/
5. *By the results of 2023 Ukrainian metallurgists produced 5.37 mln t of roll stock.* https://gmk.center/news/ukrainskie-metallurgi-po-itogam-2023-goda-proizveli-5-37-mln-t-prokata/
6. *Metallurgy of Ukraine: 30 years of evolution and partnership.* https://mind.ua/ru/publications/20230257-metallurgiya-ukrainy-30-let-evolyucii-i-partnerstva
7. Behera, P., Rajput, P., Bhoi, B. (2022) A sustainable technology to produce green and clean steel by hydrogen plasma smelting reduction. In: *Proc. of the IEI Conf. on Advanced Materials Technology Department CSIR-Institute of Minerals and Materials Technology, Bhubanswar, Odisha*, *India*, 751013. DOI: https://doi.org/10.36375/prepare_u.iei.a282. https://preprint.prepare.org.in/index.php/iei/article/view/282/155
8. (2021) *Carbon-free steel production: Cost reduction options and usage of existing gas infrastructure*. European Parliamentary Research Service. Brussels. EU. DOI: https://doi.org/10.2861/01969. https://www.europarl.europa.eu/RegData/etudes/STUD/2021/690008/EPRS_STU(2021)690008_EN.pdf
9. *Electricity production in Ukraine increased by 5 % over the year. Ekonomichna Pravda* [in Ukrainian]. https://www.epravda.com.ua/news/2022/01/11/681292/
10. Tiara Triana, Geoffrey Brooks, M. Akbar Rhamdhani (2024) Ammonia direct reduction of iron oxides-preliminary assessment. In: P*roc. of the Iron & Steel Technology Conf. (AISTech 2024), Columbus, Ohio, USA*, 295–302. DOI: https://doi.org/10.33313/388/035
11. Tiara Triana, Geoffrey A. Brooks, M. Akbar Rhamdhani, Mark I. (2024) Iron oxide direct reduction and iron nitride formation using ammonia: Review and thermodynamic analysis. *J. of Sustainable Metallurgy*, **10**, 1428–1445. DOI: https://doi.org/10.1007/s40831-024-00860-z
12. Shapovalov V.O., Biktagirov F.K., Mogylatenko V.G. (2023) *Out-of-furnace processing of steels: Methods, processes, technologies*. PWI, Kyiv, Khimgest.
13. Tiago Bristt Gonoring, Adonias Ribeiro Franco, Estefano Aparecido Vieira, Ramiro Conceição Nascimento (2022) Kinetic analysis of the reduction of hematite fines by cold hydrogen plasma. *J. of Materials Research and Technology*, **20**, 2173–2187. DOI: https://doi.org/10.1016/j.jmrt.2022.07.174
14. Lakomsky, V.I. (1974) *Plasma arc remelting:* Monography. Kyiv, Tekhnika [in Russian].
15. Grigorenko, G.M., Pomarin, Yu.M. (1989) *Hydrogen and nitrogen in metals during plasma melting.* Kyiv, Naukova Dumka [in Russian].
16. Shurkhal, V.Ya., Larin, V.K., Chernega, D.F. et al. (2000) *Physical chemistry of metallurgical systems and processes:* Manual. Kyiv, Vyshcha Shkola [in Ukrainian].
17. Kozin, R.V., Shapovalov, V.O., Mogylatenko, V.G., Biktagirov, F.K. (2023) Analysis of direct reduction of iron by hydrogen. In: *15th Inter. Sci.-Tekhn. Conf. on New Materials and Technologies in Mechanical Engineering, 9 April 27–28, 2023, Kyiv*, KPI, IPMS, PWI.
18. Knyuppel, G. (1973) Deoxidation and vacuum treatment of steel. Pt 1. Thermodynamic and kinetic regularities. Moscow, Metallurgiya [in Russian].
19. Shapovalov, V.O., Mogylatenko, V.G., Karpets, M.V., Kozin, R.V. (2023) Thermal decomposition of hematite pellets at heating by argon plasma. *Suchasna Elektrometal.*, **3**, 13–18 [in Ukrainian]. DOI: https://doi.org/10.37434/sem2023.03.03

ORCID

V.O. Shapovalov: 0000-0003-1339-3088,
V.G. Mogylatenko: 0000-0002-6550-2058
M.V. Karpets: 0000-0001-9528-1850,
R.V. Kozin: 0000-0002-8501-0827

CONFLICT OF INTEREST

The Authors declare no conflict of interest

CORRESPONDING AUTHOR

V.G. Mogylatenko
National Technical University of Ukraine
"Igor Sikorsky Kyiv Polytechnic Institute"
37 Prosp. Beresteiskyi, 03056, Kyiv, Ukraine.
E-mail: vmogilatenko@gmail.com

SUGGESTED CITATION

V.O. Shapovalov, V.G. Mogylatenko, M.V. Karpets, R.V. Kozin (2025) Producing a wüstite melt by thermal decomposition of hematite pellets with argon plasma. *The Paton Welding J.*, **2**, 24–29.
DOI: https://doi.org/10.37434/tpwj2025.02.04

JOURNAL HOME PAGE

https://patpublishinghouse.com/eng/journals/tpwj

Received: 16.09.2024
Received in revised form: 21.10.2024
Accepted: 31.03.2025

DOI: https://doi.org/10.37434/tpwj2025.02.05

REFINING METALLURGICAL SILICON

G.G. Didikin, V.O. Osokin, Ya.A. Stelmakh

E.O. Paton Electric Welding Institute of the NASU
11 Kazymyr Malevych Str., 03150, Kyiv, Ukraine

ABSTRACT

The review presents modern technologies used to refine metallurgical silicon to a purity of 5–6 N for photovoltaic cells. Refining of silicon is performed using an intermediate metal Al to capture silicon impurities after its fusion with Si. The removal of C, Ca, Fe, Ti, P from the Al-Si melt with Si is shown. After a two-time directional crystallization of the melt, Si of a purity acceptable for use in photovoltaic technologies was produced. Positive results were obtained during plasma remelting with the simultaneous application of gases in the core: Ar–H_2, H_2–H_2O, O_2, or H_2 in an Ar-based plasma. The electromagnetic stirring of the bath provides accelerated mass transfer in the liquid compared to the reaction rate on the surface with control of the surface shape. Removal of metal impurities Na, Ca, Ba, and Al up to 90–100 % was achieved using 30 % H_2 in Ar plasma. Carbon removal was observed using oxygen in the plasma at temperatures above 1530 °C. It was found that H_2 is more effective in plasma than O_2. A constant voltage in the liquid bath increases the refining efficiency by 10 times. The best results in removing boron from molten silicon were obtained by blowing the melt with humidified argon or water vapor. The resulting silicon product had favorable electronic properties. It is noted that during electron beam remelting, it is possible to purify silicon from elements with high vapor pressure and perform oxidative refining from boron impurities using a mixture of oxygen and inert gas with application of a cold hearth and zone recrystallization. In the process of EBCZM, after increasing the vacuum depth, the amount of oxygen and phosphorus in silicon can be reduced by a factor of 10.

KEYWORDS: metallurgical silicon, purification, vacuum and oxidative refining, plasma remelting, electron beam melting, silicon, solar grades, impurity elements

INTRODUCTION

Having a number of advantages, in particular, natural abundance, silicon is the most suitable material for solar photovoltaic power generation [1]. Requirements to silicon of solar grades (SoG–Si) for photoelectric converters (PEC) are much higher than those for metallurgical silicon from carbothermic reduction of silica (MG–Si), and additional refining is required to produce it. In view of the difference in the requirements for purity of silicon for the electronic and photoelectric industry and high equipment cost, the interest in investigation of different methods of development of the technologies for direct production of SoG–Si silicon remains relevant. The work presents the known technologies of refining MG–Si metallurgical silicon.

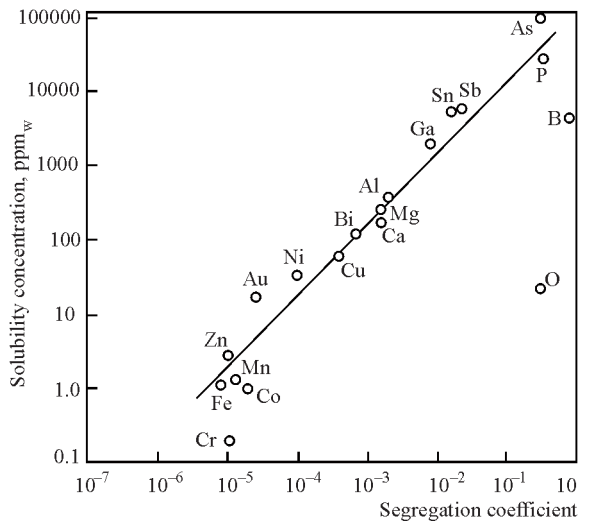

Figure 1. Solubility of some elements in silicon in the solid state, depending on the segregation coefficient [2]

INVESTIGATION PROCEDURE, EQUIPMENT AND MATERIALS

The technologies of metallurgical silicon refining to purity suitable for manufacture of photoelectric converters were selected as the object of studies.

Silicon refining with a solvent is one of the metallurgical approaches to produce SoG–Si from MG–Si using an intermediate metal, acting as an impurity trap during solidification after its fusion with Si. During cooling the pure silicon crystals precipitate from the melt, and the impurities together with the intermediate metal are forced to the solidification front, and remain in the liquid phase. The product (Si) is extracted by liquid filtering methods, leaching or electrochemical dissolution of the solidified alloy and electromagnetically induced separation. The intermediate metal should have a high affinity to boron and phosphorus, which have a low coefficient of segregation in silicon, readily dissolve in liquid silicon and have a low solubility in solid silicon (Figure 1) [2].

Al can be the intermediate metal. The process of C, Ca, Fe, Ti, P removal from Al–Si melt was studied in [3, 4]. Results showed only partial removal of these elements from Si. In works [5–8] aluminium was used as a cleaning agent to produce silicon of solar grades. As a result, Fe, Ti content in silicon was markedly re-

duced, and after two-times directional crystallization Si of a purity acceptable for application in photoelectric technologies was produced. The authors of work [9] reported a lowering of Fe, Zr, V, Ca, Ba, P, Cu, Ti, Cr and Mn concentration due to refining with aluminium. Boron content remained unchanged, and P content decreased from 45 to 15 ppm. Effective removal of Fe, Ti, Cu, Mn and Ni impurities, compared to P and B, is shown in works [10, 11]. In keeping with the obtained results, the coefficients of segregation between solid Si and Si–Al melt decrease at lower temperatures (at 1000 °C [10]), which is more favourable for Si refining, than the coefficient of segregation between the solid and liquid silicon at its melting temperature of 1414 °C [11]).

PLASMA MELTING AND REACTIVE GAS

Alongside the traditional refining stage, experiments with simultaneous application of gases of different composition bled into the active zone were conducted during plasma melting to increase the effectiveness of boron removal during solvent refining. The authors of work [12] performed experiments in Ar–H_2 atmosphere, based on the results of work [13], where the method of a melting zone was studied in the mixture of H_2–H_2O. Increase of specific resistance of silicon produced by this method was noted, in connection with boron evaporation. A more advanced method consists in silicon melting by a plasma torch when feeding reactive gas. Furtheron this procedure was studied, as a rule, using O_2 or H_2 in Ar-based plasma to remove boron. Some important experimental results are given in the Table 1 [14–17].

Boron is the most difficult to remove impurity in silicon, its limit concentration for silicon of SoG–Si class is ≤0.3–0.4 ppm_w. Under oxidizing conditions boron can form a range of oxides, the lightest of which are BO [18] or HBO [19] (in H_2–H_2O atmosphere). A serious limitation of plasma melting process is the fact that just the upper surface of the silicon bath is exposed to the influence of the plume so that impurity removal depends on their diffusion to the surface. Bath stirring with the new technique of electromagnetic stirring was used in work [20]. This method ensures accelerated mass transfer in the liquid, compared to the rate of the reaction on the surface, enables monitoring the surface shape, controlling the induction effect. Using the same procedure, the authors of [21] determined that phosphorus can evaporate in the form of P_2 at silicon melting temperature, but effective removal of boron will require the presence of H_2 (or H_2O) and O_2 to form HBO. This, however, caused problems associated with silicon loss, as well as passivation of silicon surface due to formation of a layer of solid SiO_2.

In work [22] it was found that H_2 is more effective in plasma than in O_2, for removal of metal impurities. Effectiveness of Na, Ca, Ba and Al removal was 90–100 % with application of 30 % H_2 in Ar plasma. Carbon removal was observed with application of oxygen in the plasma at temperatures above 1530 °C. Authors of [23] modified the process, applying constant voltage to the liquid bath, which increased the refining effectiveness 10 times at 105 V positive bias. During plasma melting and hydrogenation of the silicon bath [24] hydrogen presence in the plasma led to removal of residual oxygen in the silicon deposit and promoted defect passivation. Produced silicon product had favourable electronic properties.

The best results on boron removal from molten silicon were achieved during melt blowing by humidified argon or water vapor [25, 26]. Combination of the process of growing silicon ingots and its refining is a promising direction in creation of new technologies of silicon ingot production. In work [27] a 100 mm long ingot with a dense and homogeneous structure was produced (its drawing rate was 1.5 mm/min), using continuous melting of silicon in a sectional mould (to compensate for ingot expansion during crystallization) with application of high-frequency heating. At the final melting stage, due to application of a uniformly heated graphite body in the unit upper part, an upward directed crystallization of the ingot was ensured under the condition of its blowing with a gaseous reagent (Ar–1.2 % H_2O in the amount of 0.04 g/min), total gas mixture flow rate being 4 l/min. Boron content in silicon at blowing for 15 min decreased by 4 ppm_w (from 28 to 24 ppm_w).

Table 1. Experiments with plasma melting

Parameters	Scale	Significant results
Ar–0.079 up to 0.1 vol.% O_2 [14]	250 g	Increase in O_2 addition improves B removal
Ar–1.24 vol.% H_2O, 25 min [15]	5 g	[B] was decreased from 35.7 to 0.4 ppm_w
Ar–0.66 vol.% O_2, 30 min	10–40 g	[B] was decreased from 12 to 3 ppm_w
Ar–H_2O, from 15 to 60 min [16]	–	[B] removal speed increases with increase in H_2O addition
Ar, Ar + He, Ar + H_2 w/H_2O to 14.2 vol.% [17]	0.6 to 300 kg	[B] constantly decreases to <0.1 ppm_w; higher temperatures accelerate boron oxidation

The problem of manufacturing photoelectric converters (PEC) to meet the requirements of 99.9999 % SoG–Si (0.3 ppm_w B and 1.5 ppm_w P) may be solved by development of laboratory equipment with induction crucibleless suspension melting [28–30]. PWI developed and manufactured a stand for studying the processes of silicon refining from boron during induction suspension melting at temperatures of 2150–2250 °C, with the time of keeping silicon in the liquid state of 1–5 min and blowing with argon-based mixture (O_2–10 % H_2). Melting was conducted in a sectional crucible in an argon atmosphere. Intensive stirring of a silicon drop in an electromagnetic field during blowing with argon-hydrogen mixture in the presence of oxygen in metallurgical silicon promoted formation of volatile compounds of B–O–H system. In keeping with the derived data, at holding of a liquid silicon drop for 5 min boron content decreased from 0.00141 (14.1 ppm_w) to 0.00118 wt.% (11.8 ppm_w), i.e. by 16.4 %.

ELECTRON BEAM REMELTING, EVAPORATION METHODS

At present, solar panel PECs are manufactured from SG–Si silicon, including mono-crystalline-Si [31], multi-crystalline-Si, and thin film-Si PEC are also becoming widely accepted [32]. Electron beam remelting (EBR) is one of the most effective methods of silicon refining. Research works [33–35] performed in PWI electron beam units on refining scrap (mono-crystalline Si scrap), and commercial silicon (TU 48-0106.01–04) are known, and structural features of high-purity silicon produced by vacuum (VR) and oxidative refining (OR) of metallurgical silicon have been studied. The works present the technological features of EBR–VR or OR application. Attempts have been made to improve the vacuum melting technology using the electron beam, in order to remove phosphorus. Behaviour of metal and non-metal impurities during removal, depending on melting time, beam power or gas blowing (Ar or O_2) was studied. As a result, the amount of P decreased from 40 to 3 ppm_w, and B content did not change [36, 37]. In works [38, 39] crushed leached MG-Si of 99.92 % purity and whole metallurgical silicon of initial purity of 99.88 % were melted by the electron beam to make 25 mm thick discs 99 mm in diameter. Silicon of 5N purity was produced, but its purity was limited by regions in the disc upper and edge part. Refining from metal impurities was higher than 99 %, from phosphorus — 98 % (0.4 ppm_w), however, boron removal was not effective. The authors of work [40] studied phosphorus removal using electron beam method in the periodic and continuous configuration. In experiments with periodic action phosphorus removal rate is proportional to the temperature at the interface, and it depends on beam power, but with power increase the silicon evaporation rate be comes higher. In the continuous experiments phosphorus level of ≤0.1 ppm_w has been achieved at up to 50 kg/h silicon feed rate and up to 250 kW beam power, and it led to considerable silicon loss.

In work [41] the ecological cleanliness of EBR process is noted and the possibility of vacuum refining of silicon through evaporation of impurities with high vapour pressure and zone recrystallization is reported in [42]. The possibility of silicon cleaning in one technological cycle of vacuum and oxidative refining with a mixture of oxygen with inert gas is emphasized (in particular, to remove boron impurity in the form of BO, B_2O, B_2O_3 boron oxides). The author proposed a scheme of EB process of refining lumpy crystalline silicon using a cold hearth for evaporation of elements with a high vapour pressure and oxidative refining from boron impurities, and a mould for zone cleaning from Al, Cu, Fe, Ti impurities. A technology of cleaning using quartz glass has been developed.

ELECTRON BEAM CRUCIBLELESS ZONE MELTING

Work [43] presents data on the influence of sterility of vacuum melting chamber on the content of background and volatile impurities in silicon single-crystals, produced by the method of electron beam crucibleless zone melting. The problem of silicon cleaning from oxygen is relevant when it is used as radiation resistant material. Oxygen presence in silicon lowers the electronic instrument response speed and is the cause for unreproducible instrument parameters [44, 45]. During electron beam crucibleless zone melting silicon cleaning from alloying and background impurities is caused by zone recrystallization and impurity desorption from the sample surface [46]. Content of impurities in silicon is influenced by residual atmosphere in the melting vacuum chamber. This must promote impurity desorption from silicon sample surface during melting. Investigations using the infrared (IR) spectroscopy method showed that after chamber purging with helium and with increase in vacuum depth the oxygen content decreases by more than an order, while phosphorus content decreases by an order.

The authors of this paper considered the peculiarities of vacuum and oxidative refining during electron beam melting of metallurgical silicon of different purity. Ingots of initial metallurgical silicon were produced by electron beam melting in a cold copper crucible, in order to conduct the research (Figure 3). To produce silicon ingots, EBR of lumpy MG-Si was conducted by gradually increasing the power of the electron beam (EB), and refining proper was per-

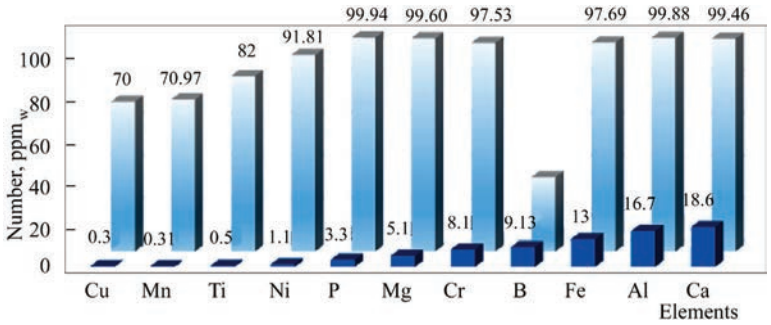

Figure 2. Impurity element content in the initial state in metallurgical silicon of Kr0 grade (GOST 2169–69) and degree of their cleaning after EBR and oxidative refining

formed at a constant beam power with melt soaking for a controlled (17 min) period of time. For subsequent crystallization, EB power was gradually reduced, ensuring a temperature gradient from the ingot edge to its center, promoting the process of zone cleaning during melting, as well as compensation of Si volumetric expansion during ingot crystallization to prevent its cracking. Technological time of conducting the experiment was 20 min. Produced ingots had the shape of a convex disc 95 mm in diameter and 30 mm thick (Figure 3). After completion of the stages of vacuum and oxidative refining, the power of heating the silicon bath was gradually reduced up to the moment of complete crystallization of the produced ingot material [47].

At the same temperature and pressure of conducting the technological process more probable is melt refining from impurity elements, having higher partial pressure (vapour pressure), allowing for its coefficient of distribution/activity in the melt [9–14]. Refining kinetics essentially depends on the technological parameters, as the real processes occur under considerably non-equilibrium thermodynamic conditions.

During heating of initial silicon by the electron beam the vapour phase over solid silicon and its melt is made up of Si gas (g), Si_2 (g), Si_3 (g). Up to the temperature of 1227 °C predominantly Si (g) is present in the vapour phase, at 1727 °C it is 94.8 % Si(g), 4.94 % Si_2 (g) and 0.26 % Si_3 (g). Silicon vapour pressure in the melting point (1417 °C) is equal to $5.66 \cdot 10^{-7}$ atm. Silicon begins to noticeably evaporate at temperatures above 1527 °C.

In silicon-oxygen system there are two silicon oxides: SiO with melting temperature of 1702 °C, boiling temperature of 1880 °C, and silicon dioxide SiO_2 with T_m = 1723 °C. SiO forms during SiO_2 reduction by silicon at high temperatures.

During metallurgical silicon recrystallization by the electron beam under vacuum, vacuum refining proceeds in the formed ingot, which is based on the difference in vapour pressure of different elements. Components, for which vapour pressure is higher than that of silicon vapours, will be removed. Figure 4, *a* shows vapour pressure in the melting point of metal impurity elements.

In boron-oxygen system, B_2O_3 boron oxide is the most stable in the solid state. This modification melts in the temperature range of 325–450 °C. At boron oxide heating with elementary boron above 1000 °C, there are heat-resistant linear molecules O=B=B=O in the vapours. Degree and speed of silicon cleaning from boron strongly depend on temperature. Boron starts to noticeably evaporate at temperatures above 2027 °C, in the melting point of 2075 °C the vapour pressure is equal to $1.37 \cdot 10^{-5}$ atm, and evaporation rate becomes equal to $4.122 \cdot 10^{-5}$ g/(cm^2·s) [15]. For effective cleaning the melt temperature should have been increased up to 2500 °C and higher.

The difference in the rate of silicon and boron evaporation from the silicon melt can be judged from literature data, for instance, for 2127 °C temperature, it is equal to $(102.8 \text{ and } 0.7) \cdot 10^{-4}$ g/(cm^2·s). Accordingly, it leads to selective evaporation of silicon in the form of oxides, and, as a result, to increase in boron content in the melt.

To study the possibility of MG–Si refining from impurities with low partial pressure (B, P, Bi, etc.), EBR was followed by oxidative refining (OR), which consists in melt treatment with gases/vapour, which contain the oxidizer (water vapour, oxygen) with high chemical affinity to impurities with formation of highly volatile compounds/oxides.

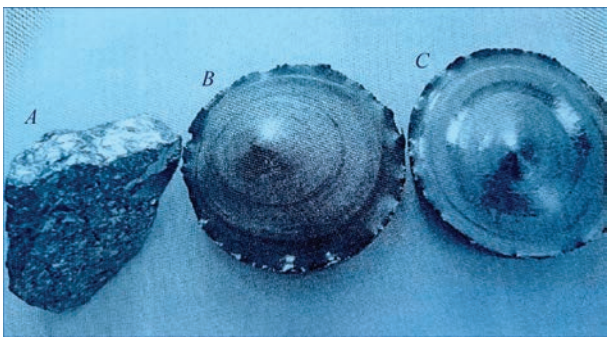

Figure 3. Initial metallurgical silicon (*A*) and ingots after vacuum (*B*) and oxidative (*C*) refining

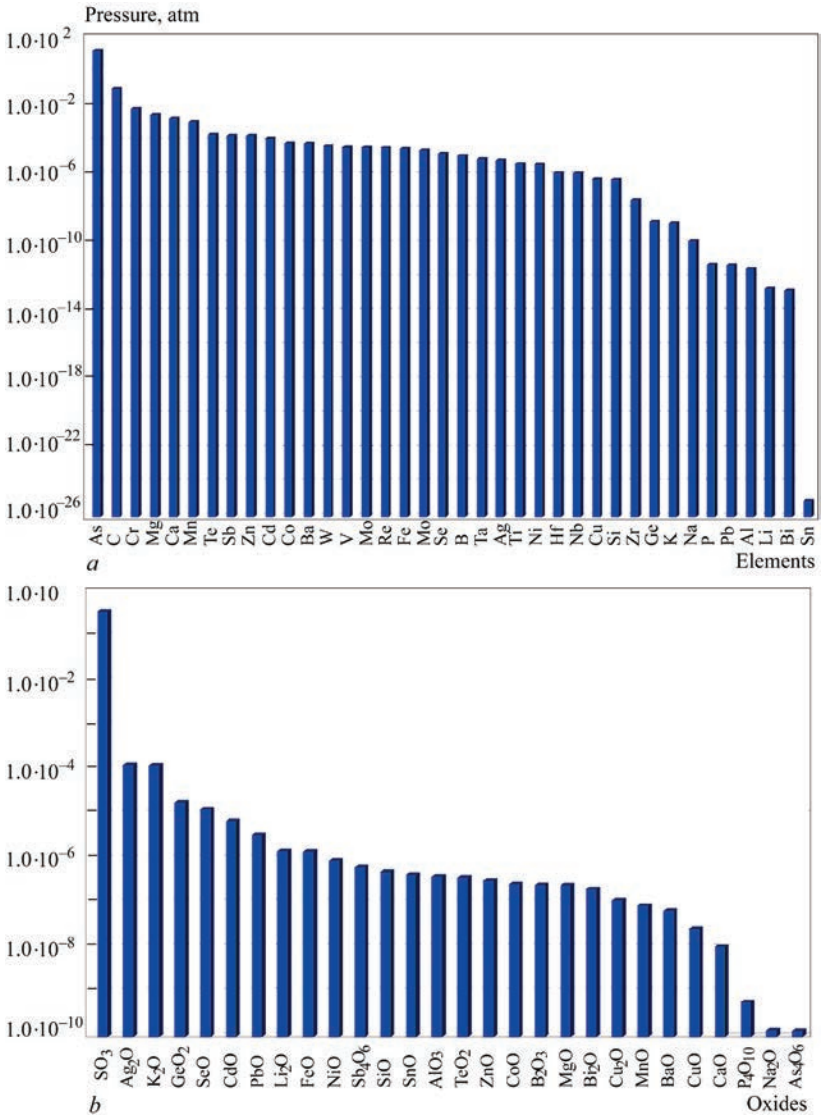

Figure 4. Partial pressure of saturated vapour in the melting point of impurity elements of metals (*a*) and oxides (*b*)

Figure 4, *b* gives the vapour pressure in the melting point of oxide impurity elements.

Volatility of monoatomic phosphorus is low, and diatomic phosphorus is the lightest (P_2). Phosphorus removal can be performed with humidified air with formation of PH_2, PH_3, PN at temperatures of 1400–1500 °C. At higher temperatures thermal decomposition of these light components occurs, and, as a result, at the temperature of ~1700 °C silicon cleaning from phosphorus through PH_2, PH_3, PN becomes practically impossible.

During performance of experimental oxidative refining (OR) of MG–Si, oxygen with flow rate of 70–80 ml/min was used during EBR for treatment of metallurgical silicon melt. An additional factor for refining from impurities in EBR is their fragmentation and partial removal, as a result of local overheating of inclusions in the zone of EBR high-energy impact [16]. Inclusions, which differ significantly by their thermal-physical parameters (heat conductivity, heat capacity) compared to the main component of the melt (Si), are quickly overheated, partially sublimated, destroyed and removed from the melt. The above-described process in the from of microexplosions with partial removal of the material particles from the melt surface is often observed visually during performance of the technological process of EBR of metals and alloys in general and of MG–Si, in particular.

The effectiveness of metallurgical silicon refining was determined by the following formula

$$C_{ef} = (C_{in} - C_{vr.or}).100/C_{in},$$

where C_{ef} is the refining effectiveness; C_{in} is the concentration of initial silicon impurities; $C_{vr.or}$ is the impurity concentration after electron beam vacuum and oxidative refining.

Figure 5, *a*, *b* shows the results of the effectiveness of evaporation of impurities from metallurgical silicon (*a*) and higher purity silicon (*b*).

Obtained results confirmed the effectiveness of MG–Si cleaning from metal impurities of Sb, Cr, Mo, K, Ti during vacuum refining and possibility of clean-

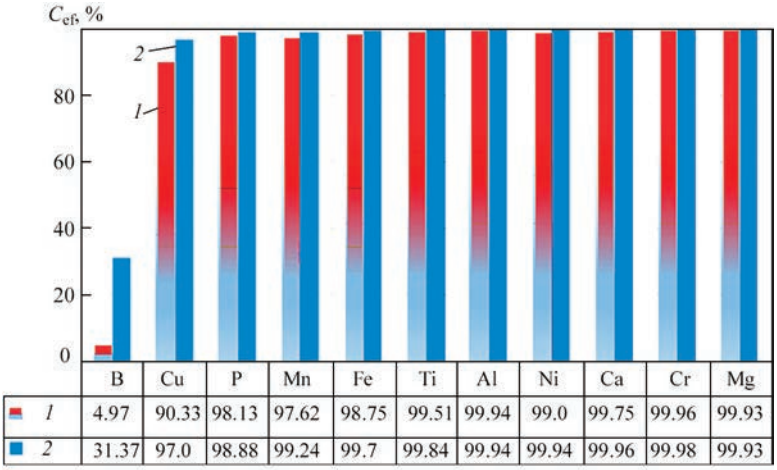

	B	Cu	P	Mn	Fe	Ti	Al	Ni	Ca	Cr	Mg
1	4.97	90.33	98.13	97.62	98.75	99.51	99.94	99.0	99.75	99.96	99.93
2	31.37	97.0	98.88	99.24	99.7	99.84	99.94	99.94	99.96	99.98	99.93

a

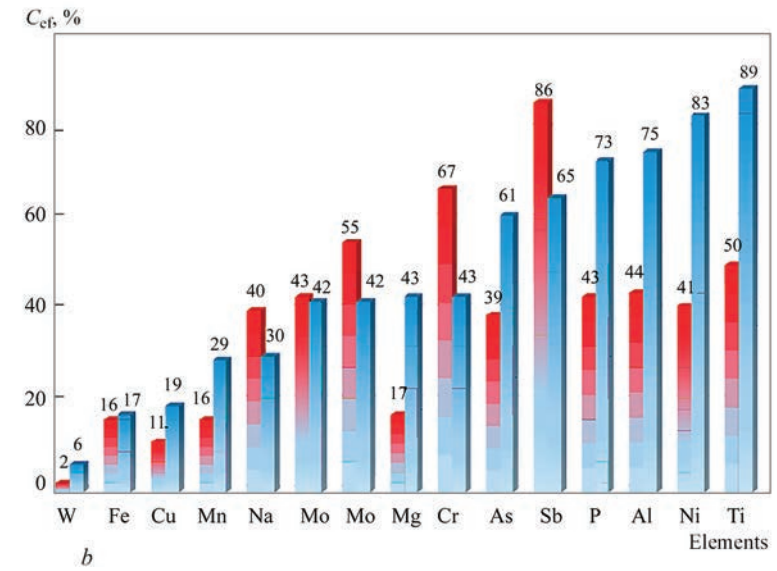

b

Figure 5. Effectiveness of refining samples of metallurgical silicon (*a*) and higher-purity silicon (*b*) after vacuum and oxidative refining: *1* – vacuum refining; *2* – oxidative refining

ing from Ti, Ni, Al, As, P and partially boron during oxidative refining. More effective refining of silicon from impurity elements and boron during EBR can be expected under the condition of a developed surface of the melt and greater duration of the ingot surface staying in the molten state.

CONCLUSIONS

1. Modern technologies are presented, which are used for refining metallurgical silicon.

2. Intermediary metal (Al) acts as an impurity trap during silicon refining after its fusion with Si. Low temperatures (beyond 1000 °C) are more favourable for Si refining. Partial removal of C, Ca, Fe, Ti, P and an abrupt lowering of Fe, Ti content in Al–Si melt with Si is shown. Double directional crystallization of the melt allowed producing Si of the purity acceptable for application in photoelectric technologies.

3. For boron removal positive results were obtained during plasma remelting with simultaneous use of gases bled into the active zone: Ar–H_2, H_2–H_2O, O_2 or H_2 in Ar-based plasma.

4. The technique of electromagnetic stirring of the bath ensures accelerated mass transfer in the liquid, compared with the speed of reaction on the surface, and surface shape is controlled.

5. It is found that H_2 is more effective in the plasma than O_2 for removal of metal impurities: effectiveness of Na, Ca, Ba and Al removal was equal to 90–100 % at application of 30 % H_2 in Ar plasma, and carbon removal was observed during oxygen application in the plasma at temperatures above 1530 °C.

6. Constant voltage on the liquid bath increases the refining effectiveness 10 times. Obtained silicon product had favourable electronic properties.

7. The best results on boron removal from molten silicon were obtained during melt blowing with humidified argon or water vapour.

8. The possibility of silicon cleaning from elements with a high vapour pressure and oxidative refining from boron impurities in one technological cycle of vacuum and oxidative refining with a mixture

of oxygen with inert gas, using a cold hearth and zone recrystallization is noted.

9. During electron beam crucibleless zone melting silicon cleaning from alloying additives and background impurities is caused by zone recrystallization and impurity desorption from the sample surface. After increasing the vacuum depth, oxygen content decreases by more than an order, with phosphorus content decreasing by an order.

REFERENCES

1. Despoto, E., El Gammal, A., Fontaine, B. et al. (2010) *Global market outlook for photovoltaics until 2014, European Photovoltaic Industry Association, Brussels, 2010)*. https://www.academia.edu/98819863/High_Temperature_Refining_of_Metallurgical_Grade_Silicon_A_Review?uc-sb-sw=98763071
2. Johnston, M.D., Khajavi, L.T., Li, M. et al. (2012) High-temperature refining of metallurgical grade silicon: A review. *JOM*, **64**, 935. DOI: https://doi.org/10.1007/s11837-012-0384-3
3. Obinata, I., Komatsu, N. (1957) Thermodynamics of phosphorus in solvent refining of silicon using ferrosilicon alloys. *Sci. Rep. RITU*, **A-9**, 118–30. https://ouci.dntb.gov.ua/en/works/ldBWBkY7/
4. Ciftja, A., Engh, T.A., Tangstad M. (2008) *Refining and recycling of silicon: A review*. NTNU, Trondheim. https://www.researchgate.net/publication/267552614_Refining_and_Recycling_of_Silicon_A_Review
5. Kotval, P.S., Strock, H.B. (1978) US Pat. 4,124,410, Union Carbide Corporation.
6. Kotval, P.S., Strock, H.B. (1980. a) US Pat. 4,193,974, Union Carbide Corporation.
7. Kotval, P.S., Strock, H.B. (1980. b) US Pat. 4,193,975, Union Carbide Corporation.
8. Kotval, P.S., Strock, H.B. (1980. c) US Pat. 4,195,067, Union Carbide Corporation.
9. Gumaste, J., Mohanty, B., Galgali, R. et al. (1987) Solvent refining of metallurgical grade silicon. *Sol. Energy Mater*., **16**, 289–96. DOI: https://doi.org/10.1016/0165-1633(87)90077-3
10. Yoshikawa, T., Morita, K. (2005) In: *EPD Congress on High-Temperature Refining of Metallurgical-Grade Silicon (TMS, Warrendale, PA)*, 549–58. https://tspace.library.utoronto.ca/bitstream/1807/93627/1/High%20Temp_TSpace.pdf
11. Bathey, B., Cretella, M.C. (1982) Vacuum refining of molten silicon. *J. Mater. Sci*., **17**, 3077–96. DOI: https://doi.org/10.1007/BF01203469
12. Yoshikawa, T., Arimura, K., Morita, K. (2005) Thermodynamics of impurities removal from Si–Fe alloy. *Metall. Mater. Transact. B*, 36B(**6**), 837–42. DOI: https://doi.org/10.1007/s11663-005-0085-1
13. Theuerer, H.C. (1956) Boron removal from silicon by humidified gases. *J. Metals*, **8**, 1316–19. DOI: http://dx.doi.org/10.1007/s40553-014-0007-8
14. Morvan, D., Amouroux, J., Charpin, M.C., Lauvrey, H. (1983) High-temperature refining of metallurgical-grade silicon: A review. *Rev. Phys. Appl.*, 18(**4**), 239–51. http://ui.adsabs.harvard.edu/abs/2012JOM....64h.935J/abstract
15. Suzuki, K., Kumagai, T., Sano, N. (1992) *ISIJ Int*., 32(**5**), 630–34. https://link.springer.com/article/10.1007/BF02662772
16. Ikeda, T., Maeda, M. (1996) High-temperature refining of metallurgical grade silicon. *Mater. Transact., JIM*, 37(**5**), 983–87. https://tspace.library.utoronto.ca/bitstream/1807/93627/1/High%20Temp_TSpace.pdf
17. Nakamura, N., Baba, H., Sakaguchi, Y., Kato, Y. (2004) Boron removal from silicon by humidified gases. *Mater. Transact*., 45(**3**), 858–64. https://link.springer.com/article/10.1007/s11663-005-0085-1
18. Suzuki, K., Kumagai, T., Sano, N. (1992) Thermodynamics of boron in a silicon melt. *ISIJ Int*., 32(**5**), 630–34. https://link.springer.com/article/10.1007/s11663-012-9671-1
19. Lynch, D. (2009) Winning the global race for solar silicon. *JOM*, 61(**11**), 41–48. https://link.springer.com/article/10.1007/s11837-009-0166-8
20. Delannoy, Y., Alemany, C., Li, K.-I. et al. (2002) Plasma-refining process to provide solar-grade silicon. *Sol. Energy Mater. Sol. Cells*, **72**, 69–75. https://www.academia.edu/6146609/Plasma_refining_process_to_provide_solar_grade_silicon
21. Alemany, C., Trassy, C., Pateyron, B. et al. (2012) Processes for upgrading metallurgical grade silicon to solar grade silicon. *Sol. Energy Mater. Sol. Cells*, **72**, 41–48. DOI: https://doi.org/10.1016/j.egypro.2012.03.011
22. Tsao, S., Lian, S.-S. (2005) Boron removal from silicon by humidified gases. *Mat. Sci. Forum*, **475–479**, 2595–98. DOI: http://dx.doi.org/10.1007/s40553-014-0007-8
23. Rousseau, S., Benmansour, M., Morvan, D., Amouroux, J. (2007) Boron removal from silicon by humidified gases. *Sol. Energy Mater. Sol. Cells*, 91(**20**), 1906–15. DOI: http://dx.doi.org/10.1007/s40553-014-0007-8
24. Benmansour, M., Rousseau, S., Morvan, D. (2008) High-temperature refining of metallurgical-grade silicon: A review. *Surf. Coat. Technol*., **203**, 839–43. http://ui.adsabs.harvard.edu/abs/2012JOM....64h.935J/abstract
25. Moon, D.V., Lee, H.M, Kim, B.K. (2010) Boron removal from UMG-Si by hydrid melting utilizing Steam plasma torch and EMCM. In: *Proc. of Conf. on Photovoltaic Spesialist, 35th IEEE, Honolulu, 20–25 June 2010*, 002194–002197.
26. Nakamura, N., Baba, H., Sakaquchi, Ya., Kato, Yo. (2004) Boron removal in molten silicon by a steam-faded plasma melting method. *Materials Transact*., 45(**3**), 858–864.
27. Shapovalov, V.A., Sheiko, I.V., Nikitenko, Yu.A. et al. (2012) Induction melting and refining of silicon in a sectional solidification mould. *Advances in Electrometallurgy*, **4**, 259–263.
28. Grigorenko, G.M., Shapovalov, V.A., Sheiko, I.V. et al. (2013) Refining of silicon in levitation melting. *Advances in Electrometallurgy*, **1**, 40–45.
29. Fogel, A.A. (1979) *Induction method of liquid metal containment in levitation.* Leningrad, Mashinostroenie [in Russian].
30. Grigorenko, G.M., Sheiko, I.V. (2006) *Induction melting of metals in cold crucibles and cooled sectional moulds.* Kyiv, Stal [in Russian].
31. *Future of solar photovoltaic, deployment, investment, technology, grid integration and socio-economic aspects*. https://www.irena.org/publications/2019/Nov/Future-of-Solar-Photovoltaic
32. *Solar power Europe, what's cool in solar: Wafers*. https://www.solarpowereurope.org/whats-cool-in-solar-wafers/
33. Osokin, V.A., Shpak, P.A., Ishchenko, V.V. et al. (2008) Electron beam technology of polycrystalline silicon refining for solar energy. *Metallurg,* **2**, 69–73 [in Russian].
34. Osokin, V.A., Panibratsky, V.A. (2010) Refining of metallurgical silicon by vacuum electron beam method. *Vymiryuvalna ta Obchyslyuvalna Tekhnika v Tekhnologichnykh Protsessakh,* **2**, 40–47 [in Russian].
35. Osokin, V.A., Panibratsky, V.A., Shpak, P.A., Piyuk, E.L. (2011) Peculiarities of structure of high-pure silicon produced by electron beam refining of metallurgical silicon. *Metallurg,* **8**, 82–87 [in Russian].
36. Ikeda, T., Maeda, M. (1992) Purification of metallurgical silicon for solar-grade silicon by electron beam button melting.

ISIJ Int., 32(**5**), 635–642. DOI: https://doi.org/10.2355/isijinternational.32.635
37. Suzuki, K., Sakaguchi, K., Nakagiri, T., Sano, N. (1990) Gaseous removal of phosphorus and boron from molten silicon. *J. Japan Inst. Met*., 54(**2**), 161–67. DOI: https://doi.org/10.2320/jinstmet1952.54.2_161
38. Pires, J.C.S., Braga, A.F.B., Mei, P.R. (2003) High-temperature refining of metallurgical-grade silicon: A review. *Energy Mater. Sol. Cells*, 79(**3**), 347–55.
39. Pires, J.C.S., Otubo, J., Braga, A.F.B., Mei, P.R. (2005) The purification of metallurgical grade silicon by electron beam melting. *Mat. Proc. Tech*., 169(**1**), 16–20.
40. Hanazawa, K., Yuge, N., Kato Y. (2004) Model implementation of boron removal using $CaCl_2$–CaO–SiO_2 slag system for solar-grade silicon. *Mater. Transact*., 45(**3**), 844–49. DOI: https://doi.org/10.1007/s11663-017-1105-7
41. Berezos, V.A. (2013) Electron beam refining of crystalline silicon. *Advances in Electrometallurgy*, **3**, 188–194.
42. Berezos, V.A., Erokhin, A.G. (2009) Refining silicon by electron beam melting. *Advances in Electrometallurgy*, **3**, 174–177.
43. Asnis, E.A., Piskun, N.V., Statkevich I.I. (2011) Purification of silicon to remove phonon and doping impurities in electron beam crucibleless zone melting. *Advances in Electrometallurgy*, **4**, 215–217.
44. Paton, B.E., Asnis, E.A., Zabolotin, S.P. et al. (2003) Production of extrapure bulk semiconductor materials under space vacuum. *Kosmichna Nauka i Tekhnologiya,* 9(**5–6**), 30–32 [in Russian].
45. Pfann, B. (1970) *Zone melting.* Moscow, Mir [in Russian].
46. Nepomnyashchikh, A.I., Krasin, B.A., Vasilieva, I.E. et al. (2002) Multicrystalline silicon for solar energy. *Materialy Elektronnoj Tekhniki,* **4**, 16–24 [in Russian].
47. Osokin, V.O., Stelmakh, Y.A., Kurapov, Yu.A., Shpak, P.O. (2022) Features of impurity segregation and microstructure of Si ingot obtained by electron-beam purification of metallurgical grade silicon. *J. of Nano- and Electronic Physics*, 14(**6**), 06012. DOI: https://doi.org/10.21272/jnep.14(6).06012

ORCID
G.G. Didikin: 0000-0002-9268-5072,
V.O. Osokin: 0000-0002-0632-7739,
Ya.A. Stelmakh: 0000-0002-5238-2288

CONFLICT OF INTEREST
The Authors declare no conflict of interest

CORRESPONDING AUTHOR
G.G. Didikin
E.O. Paton Electric Welding Institute of the NASU
11 Kazymyr Malevych Str., 03150, Kyiv, Ukraine.
E-mail: didikin@paton-icebt.kiev.ua

SUGGESTED CITATION
G.G. Didikin, V.O. Osokin, Ya.A. Stelmakh (2025) Refining metallurgical silicon. *The Paton Welding J*., **2**, 30–37.
DOI: https://doi.org/10.37434/tpwj2025.02.05

JOURNAL HOME PAGE
https://patonpublishinghouse.com/eng/journals/tpwj

Received: 10.06.2024
Received in revised form: 31.10.2024
Accepted: 16.01.2025

DOI: https://doi.org/10.37434/tpwj2025.02.06

DETECTION OF INTERNAL ULTRA-SMALL DEFECTS IN ALUMINIUM WELDED JOINTS BY THE SHEAROGRAPHY METHOD

L.M. Lobanov, O.P. Shutkevych, I.V. Kyyanets, I.L. Shkurat, K.V. Shyyan, V.V. Savitsky

E.O. Paton Electric Welding Institute of the NASU
11 Kazymyr Malevych Str., 03150, Kyiv, Ukraine

ABSTRACT

In modern industry, ensuring the quality of welded joints, particularly those made from aluminium alloys, is a crucial task for enhancing the reliability of structures. Special attention is paid to detecting internal defects that may lead to their premature failure. The aim of this work is to develop and apply a shearography non-destructive testing method in combination with thermal loading to detect ultra-small defects in welded joints of aluminium alloys. Loading was provided by an automated system that allowed the surface of tested specimens to be heated by 3–7 °C for 2–4 s. The studies showed that the advanced shearography equipment can detect defects as small as 0.3 mm in diameter, with a depth of up to 1.8 mm, both in the weld zone and in the base metal. The proposed parameters of thermal loading and the settings of the interferometer optical scheme allowed achieving a high sensitivity to ultra-small defects. The shearography method with automated thermal loading is effective for detecting internal defects in welded joints of aluminium alloys and can be used for non-destructive testing in production conditions.

KEYWORDS: non-destructive testing, shearography; aluminium alloys, ultra-small defects

INTRODUCTION

The production of modern parts and structures of high quality and reliability is associated with the use of the latest structural materials with specified physical and mechanical properties. Ensuring the high quality of the produced structures is one of the most crucial scientific and technical challenges. Therefore, it is important to improve the known and develop new modern automated methods and tools for quality testing of mechanisms and structures. Nowadays, various non-destructive methods are used to detect defects in materials and structures, such as radiographic, acoustic, luminescent, eddy current, etc. [1, 2]. Each of these methods has its own disadvantages and advantages, but none of them is universal and does not meet all the requirements for non-destructive testing tools and methods. In leading modern industries, especially in the automotive, shipbuilding, power and aerospace engineering sectors, new structural materials are widely used in the manufacture of thin-sheet structures. They mostly operate under severe mechanical and temperature conditions. Therefore, even a small concentration of stresses caused by defects in welds or structural elements can lead to their failure.

Hidden defects, which are undetected during manufacturing inspections, often cause reduced structural quality. A significant part of product failures at the initial stage of their operation is associated with the manifestation of such hidden defects. In most cases, they also cause the failure of assemblies and structural elements in the course of their further use. Therefore, in order to improve the testing and reliability of structural assemblies and elements, it is important to use modern methods of non-destructive testing [3–6]. A group of the above-mentioned quality testing methods is successfully supplemented by laser interferometry methods, especially speckle interferometry. The shearography method is promising for engineering applications [7, 8]. This method makes it possible to directly obtain the values of derivatives from the displacements and is effective in analysing deformations. The shearography method is insensitive to displacements of the object as a whole, since such displacements do not cause deformations and, therefore, do not require special protection against vibrations.

The intensive development of computing technology has made it possible to significantly improve the method of shearography and develop the method of digital shearography [9]. An important characteristic feature of this method is the ability to observe a dynamic pattern of interference fringes on a monitor in real time. Due to relative simplicity, this method can be used to solve much more complex problems related to deformation analysis and quality testing of structures in laboratory and industrial conditions.

Studies on the detection of fine defects in lamellar composites using thermal-loaded shearography are presented in [10, 11], and both experimental and numerical results on the detection of small defects are presented. In the given articles, a thermomechanical finite element model was created in Abaqus to evaluate different thermal loading schemes for flaw detection. The rational choice of reference and signal interference patterns from the heating/cooling sequence for reliable flaw detection was determined. Experimental and numerical results show that this approach

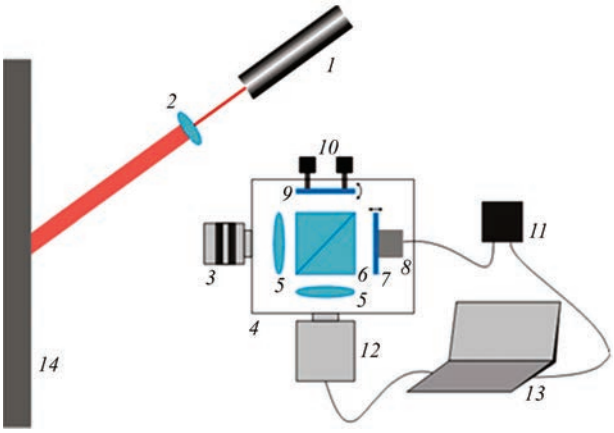

Figure 1. Block diagram of shearography system: *1* — laser; *2* — beam expander; *3* — lens; *4* — shearography interferometer containing lenses *5*, beamsplitter *6,* mirror *7,* mounted on piezoelectric element *8*, mirror *9*, which creates an image shear by means of screws *10*; *11* — PZT controller *8*; *12* — digital camera; *13* — laptop; *14* — tested object

allows detecting millimetre and submillimetre defects in carbon fibre reinforced lamellar composites.

In [12], a method of real-time phase processing with high-frequency synchronization of the digital camera, PZT-mirror and load is proposed to improve the quality of the phase pattern and the efficiency of protection against noise during the phase shift process. The method was applied to optical non-destructive measuring systems of shearography/ESRI to detect minor tear defects with a minimum size of 2 mm and to evaluate the interfacial adhesive strength of bonding layers, respectively. Currently, digital shearography is being intensively developed and has the following advantages: visualization, contact-free nature, high sensitivity and the ability to perform real-time studies of complex-shaped and large-sized objects.

THE AIM

of this work is to develop a technology for detecting internal defects of ultra-small sizes (less than 1 mm in diameter) in aluminium welded joints using the digital shearography method in combination with automated thermal loading.

METHOD OF SHEAROGRAPHY FOR NON-DESTRUCTIVE QUALITY TESTING

To conduct the NDT experiments, a shearography system based on the Michelson interferometer, which is sensitive to out-of-plane deformation, was used to conduct the NDT experiments, which is sensitive to out-of-plane deformation (Figure 1). The shearography experiments were carried out using the software developed by the authors, which contains additional options for control of the thermal load. It allows setting the time of recording the initial state, switching on and off the temperature load, recording the loaded state, as well as the time of exporting the initial and loaded states to the software for processing the received images.

Figure 2. Appearance of shearography interferometer with laser modules and replaceable lens

NON-DESTRUCTIVE QUALITY TESTING OF ALUMINIUM WELDED JOINTS BY THE SHEAROGRAPHY METHOD

Experiments on non-destructive testing by the shearography method in combination with thermal loading were performed on welded aluminium alloy specimens. The specimens were planar and were made by friction stir welding. During the experiments, the specimens were fixed in a mounting frame, which allowed applying a thermal load (Figure 3). The loading was carried out automatically using the developed software. The shearography patterns were recorded both at the heating and cooling stages with a 10-fold optical magnification, which was achieved by installing a 75 mm focal length lens and an additional optical ring. The shear was chosen along the *OX* or *OY* direction and its value was 10 mm.

In the process of testing aluminium specimens, thermal loading with hot air was applied using an industrial hot air gun. The air heating temperature was set to 500 °C, the distance from the hot air gun to the specimen surface was ~20 mm, the heating lasted 2–3 s and the change in surface temperature was up to 10 °C.

Figure 5 shows the location scheme of the defect in the welded specimen. Figure 6 shows settings used for automatic thermal loading. In the first step (Step1), the initial state of the object is recorded. In the second step (Step2), the temperature load is switched on and off in the third step (Step3). In the fourth step (Step4), a speckle pattern of the deformed state of the object is recorded.

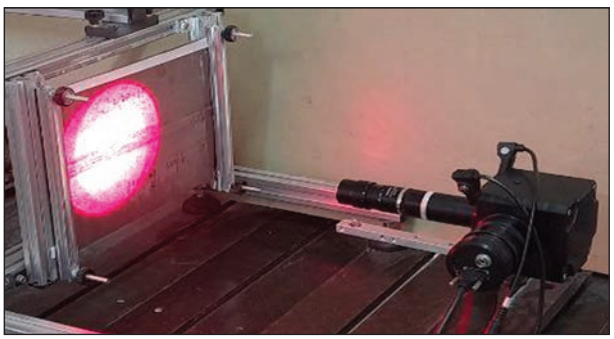

Figure 3. Appearance of shearography interferometer with a 10-fold optical magnification and test specimen fixed in a mounting frame

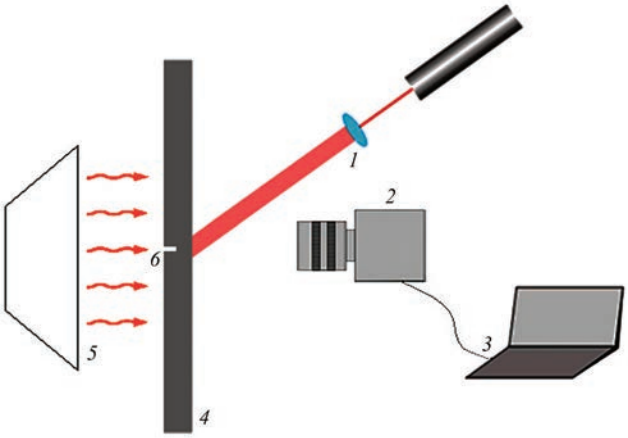

Figure 4. Scheme of the experiment: *1* — laser illumination; *2* — shearography interferometer; *3* — laptop; *4* — tested specimen; *5* — heating source; *6* — blind hole

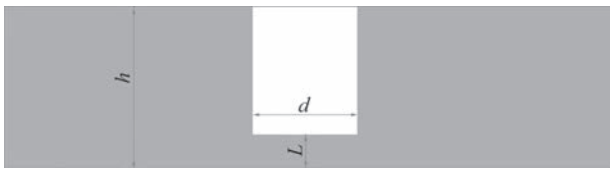

Figure 5. Scheme of defect location in welded specimen: *h* — thickness of specimen; *d* — diameter of hole; *L* — depth of occurrence (wall thickness remaining after drilling a blind hole with a diameter *d*)

In the fifth step (Step5), the initial and final states of the object are exported to a programme for processing.

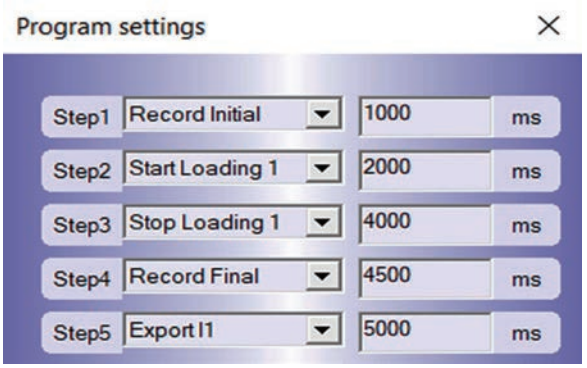

Figure 6. Settings of loading tested specimen in milliseconds

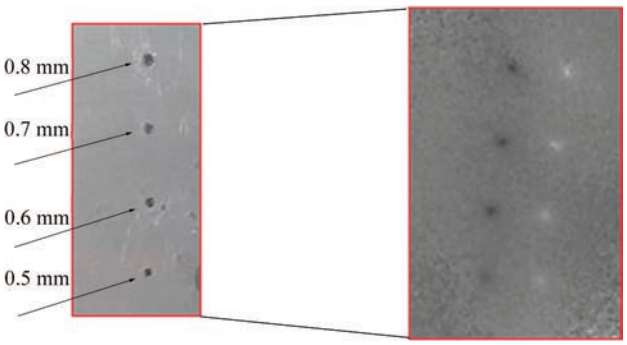

Figure 7. Shearography inspection of the test area of an aluminium specimen: general view of the area (*a*) and a typical pattern of detected defects with diameters *d* = 0.5, 0.6, 0.7 and 0.8 mm (*b*)

To develop the shearography testing procedure, blind holes with a diameter of *d* = 0.5–0.8 mm and a

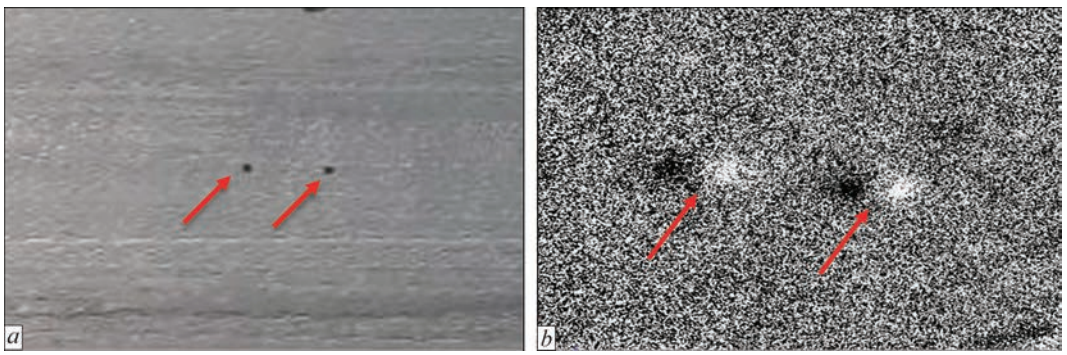

Figure 8. Shearography inspection of the test area of a weld of an aluminium specimen: general view of the area with defects (*a*) and a typical pattern of detected defects with a diameter of 0.3 mm and a depth of *L* = 0.35 and 0.85 mm (*b*)

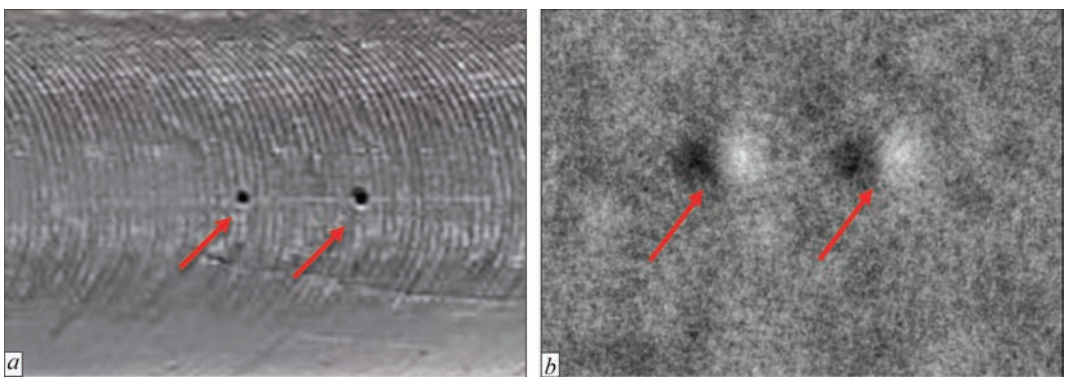

Figure 9. Shearography inspection of the test area of a weld of an aluminium specimen: general view of the area with defects (*a*) and typical pattern of detected defects with a diameter of *d* = 0.3 mm and a depth of *L* = 1.8 and 1.5 mm (*b*)

depth of L = 0.1 mm were drilled on the base metal of a welded specimen with a thickness of h = 2.5 mm (Figure 7, *a*). The results indicating the presence of defects in the studied area are shown in Figure 7, *b*. A local sharp change in the value and sign of the derivative characterises the presence of a defective zone. Since the shear is much larger than the size of the created blind holes, such defects are manifested against the background of uniform deformation as two separate areas in the direction and at a distance of the shear (dark and light).

Following the development of the shearography testing procedure, it was applied to inspect ultra-small artificial defects. The defects represented holes with a diameter of d = 0.3 mm and different drilling depths located in a weld made by friction stir welding. The results of testing defective areas are shown in Figures 8, 9.

The above shearograms clearly show local features that characterise the presence of embedded defects.

CONCLUSIONS

A procedure has been developed to detect ultra-small defects (<1.0 mm) located both in the areas of the base metal of aluminium welded joints and in the weld zone. This was achieved by using a shearography interferometer with a 10-fold optical magnification, selecting a shear that is larger than the sizes of a defect and automated dosed thermal loading. It has been experimentally confirmed that the proposed approach makes it possible to detect defects with a minimum size of 0.3 mm in diameter, which are located under the surface at a depth of 0.35–1.80 mm.

REFERENCES

1. (2001) *Non-destructive testing and technical diagnostics*. Ed. by Z.T. Nazarchuk. Lviv, PMI [in Ukrainian].
2. Rastorgi, P.K., Inaudi, D. (2000) *Trends in otical non-destructive testing and inspection*. Oxford, Elsevier Science B.V.
3. Nazarchuk, Z.T., Muravsky, L.I., Kuts, O.G. (2022) Nondestructive testing of thin composite structures for subsurface defects detection using dynamic laser speckles. *Research in Nondestructive Evaluation*, 33(**2**), 59–77. DOI: https://doi.org/10.1080/09349847.2022.2049407
4. Lai, W.L., Kou, S.C., Poon, C.S. et al. (2009) Characterization of flaws embedded in externally bonded CFRP on concrete beams by infrared thermography and shearography. *J. Nondestruct. Eval*., 28(**1**), 27–35. DOI: https://doi.org/10.1007/s10921-009-0044-x
5. Vandenrijt, J.F., Xiong, H., Lequesne, C. et al. (2019) Shearography inspection of monolithic CFRP composites: Finite element modeling approach for assessing an adequate strategy of artificial defects representing delamination. In: *Conf. Optical Measurement Systems for Industrial Inspection XI*, **11056**, 107–113. DOI: https://doi.org/10.1117/12.2527445
6. Menner, P., Gerhard, H., Busse, G. (2011) Lockin-interferometry: Principle and applications in NDE. *Strojniški Vestnik . J. of Mechanical Eng.*, 57(**3**), 183–191. DOI: https://doi.org/10.5545/sv-jme.2010.169
7. Lobanov, L.M., Pivtorak, V.A., Savitsky, V.V. et al. (2005) Express control of quality and stressed state of welded structures using methods of electron shearography and speckle-interferometry. *The Paton Welding J.*, **8**, 35–40.
8. Hung, Y.Y., Ho, H.P. (2005) Shearography: An optical measurement technique and applications. *Materials Sci. and Eng.: R:Reports*, 49(**3**), 61–87. DOI: https://doi.org/10.1016/j.mser.2005.04.001
9. Lobanov, L.M., Savytskyi, V.V., Kyianets, I.V.et al. (2021) Non-destructive testing of elements of titanium honeycomb panels by shearography method using vacuum load. *Tekh. Diahnost. ta Neruiniv. Kontrol*, **4**, 19–24 [in Ukrainian]. DOI: https://doi.org/10.37434/tdnk2021.04.02
10. Tao, N., Anisimov, A.G., Groves, R.M. (2024) Shearography with thermal loading for defect detection of small defects in CFRP composites. In: *Proc. of the 21st European Conf. on Composite Materials (ECCM21)*, *02–05 July 2024, Nantes, France*, Vol. 4: Experimental Techniques, 85–90.
11. Tao, N., Anisimov, A.G., Groves, R.M. (2022) Shearography non-destructive testing of thick GFRP laminates: Numerical and experimental study on defect detection with thermal loading. *Compos. Struct.*, **282**, 115008. DOI: https://doi.org/10.1016/j.compstruct.2021.115008
12. Bin Liu, Shuo Wang, Mingming Zhan et al. (2022) Optical nondestructive evaluation for minor debonding defects and interfacial adhesive strength of solid propellant. *Measurement*, **194**, 111066. DOI: https://doi.org/10.1016/j.measurement.2022.111066

ORCID

L.M. Lobanov: 0000-0001-9296-2335,
O.P. Shutkevych: 0000-0001-5758-2396,
I.V. Kyyanets: 0000-0002-2559-8200,
I.L. Shkurat: 0009-0003-1888-4203,
K.V. Shyyan: 0000-0001-9198-6554,
V.V. Savitsky: 0000-0002-2615-1793

CONFLICT OF INTEREST

The Authors declare no conflict of interest

CORRESPONDING AUTHOR

V.V. Savitsky
E.O. Paton Electric Welding Institute of the NASU
11 Kazymyr Malevych Str., 03150, Kyiv, Ukraine.
E-mail: viktor.savitsky@nas.gov.ua

SUGGESTED CITATION

L.M. Lobanov, O.P. Shutkevych, I.V. Kyyanets, I.L. Shkurat, K.V. Shyyan, V.V. Savitsky (2025) Detection of internal ultra-small defects in aluminium welded joints by the shearography method. *The Paton Welding J.*, **2**, 38–41. DOI: https://doi.org/10.37434/tpwj2025.02.06

JOURNAL HOME PAGE

https://patonpublishinghouse.com/eng/journals/tpwj

Received: 14.10.2024
Received in revised form: 15.11.2024
Accepted: 31.03.2025

DOI: https://doi.org/10.37434/tpwj2025.02.07

DETECTION OF CIRCULAR SUBSURFACE DEFECTS IN LAMINATED COMPOSITES USING OPTICAL-ACOUSTIC NONDESTRUCTIVE TESTING SYSTEM

O.M. Sharabura, L.I. Muravsky, O.G. Kuts

G.V. Karpenko Physico-Mechanical Institute of the NASU
5 Naukova Str., 79060, Lviv, Ukraine

ABSTRACT

An optical-acoustic system layout for nondestructive testing of subsurface defects in laminated composites has been developed. Detection and localization of subsurface defects in composite laminated structures with the help of the optical-acoustic system layout are performed by forming a series of dynamic speckle patterns of the composite surface, which is excited by a flexural elastic wave, their subsequent recording and accumulation in order to generate differential digital speckle patterns and extract optical spatial responses from defects. To assess the efficiency of detecting such defects, fiberglass laminated structures were manufactured containing three layers of glass textolite plates and circular flat defects of various sizes in the middle layer. Based on the conducted studies, an experimental dependence of the fundamental resonance frequency of circular subsurface defects on their sizes was obtained, which is close to the theoretically plotted one. It is shown that using the created optical-acoustic system layout, it is possible to detect such defects in a wide range of changes in their sizes.

KEYWORDS: optical-acoustic system, dynamic speckle pattern, circular subsurface defect, region of interest, difference speckle pattern, elastic wave, laminated composite

INTRODUCTION

Constant improvement of materials and structural elements, used in mechanical engineering, aerospace, construction industry, etc. requires continuous development of methods and means of their nondestructive testing (NDT) and technical diagnostics. In order to develop new and improve the available methods of NDT of materials and structures, processes of different physical nature, are used. A lot depends on the conditions, under which the control process is expected to be carried out, properties of materials, from which the object of study is made, types of defects to be revealed, etc. Over the recent years, high-speed NDT equipment has been intensively developed. It is based on the principles of thermography, digital speckle-interferometry and shearography [1–4] and enables parallel selection of 2D and 3D data arrays from a large area of the object of study and their further digital processing.

The advantage of thermographic methods is the large area of the object and contactless procedure of material heating. Their possibilities, however, are limited by the small thickness of the material of the object of study, considerable energy costs for its heating and high cost of equipment, in particular an infrared camera. Moreover, the need for preheating the object of study is harmful to the environment and worsens the ecological condition of the surrounding area.

Shearography methods are effectively used for NDT of surfaces of a large area [3–6]. Shearography systems allow testing a large area of the object of study with a high speed without any need for additional heating. They are applied to detect, measure and localize anomalies by reproduction and visualization of microscopic changes on the studied surface during the respective loading. The digital shearography camera checks the entire field of vision practically simultaneously, in contrast to vibrometric and ultrasonic (US) scanning means of [3]. There exist a range of methods of loading application in such systems, in particular diverse mechanical and vibrational loads, loading under the impact of sonic or US signals, pressure, etc., which lead to minor local deformations of the surface caused by both surface and subsurface defects. These can be impact damage, disbanding delamination, porosity, thermal damage, cracks, etc. Such deformations are readily identified by NDT shearography systems [1, 2, 5, 6]. In such systems, however, it is necessary to use a complex imaging module, which complicates their overall design.

Unlike the interferometry NDT methods, in the optical-acoustic method (OAM) only the speckle patterns of the surface are used to detect subsurface defects in composite structures. The surface is excited by elastic waves from an acoustic radiation source. Coherent speckle patterns are formed without application of a reference laser beam, resulting in considerable simplification of optical-digital NDT systems, implementing OAM. The method consists in exciting a composite structure with a flexural elastic wave, illuminating an area of the composite surface with an expanded laser beam, and forming a series of dynamic speckle patterns of the composite surface area generated with opposite polarities of the elastic wave, the frequency of which changes monotoni-

cally. A digital camera accumulates two series of dynamic speckle patterns and, as a result of this accumulation, records a pair of digital speckle patterns (DSPs). After high-speed processing of the DSP pairs, defect maps are obtained containing optical spatial responses from regions of interest located directly above the defects. Further, the obtained defect maps are used to determine the location, dimensions and depth of occurrence of subsurface defects. OAM is described in detail in works [7–11].

OPTICAL-ACOUSTIC SYSTEM FOR NONDESTRUCTIVE TESTING OF SUBSURFACE DEFECTS

A layout of optical-acoustic system (OAS) for subsurface defects NDT was created for OAM technical realization [7–11]. Its block-diagram is shown in Figure 1. One of the key points of difference of OAS consists in that compared to the known interferometry systems for internal defects detection it does not contain an interferometer or a shearography unit. Due to that it has a much simpler design and low sensitivity to vibrations and other external impacts.

Optical spatial response from a subsurface defect to OAS is generated by comparing the recorded DSP $I_{n1}(i, j)$ obtained at maximum values of elastic wave amplitude, with DSP $I_{n2}(i, j)$ obtained at their minimum values. The procedure of DSP cross-correlation is described in detail in [9–11] and it is performed by deriving the difference DSP:

$$I_n(i,j) = |I_{n1}(i,j) - I_{n2}(i,j)|. \quad (1)$$

After deriving the difference DSP which can be interpreted as a defect map, a natural question arises, how the defect parameters can be determined based on the generated map. For this purpose, we need to establish a connection between the subsurface defect shape and its size and depth of occurrence. One of the possible approaches to solving this problem consists in application of mathematical physics methods for construction of a mathematical model of the respective defect. To derive the expressions, connecting the physical parameters of the material, from which the diagnosed object is made, with the defect parameters and its resonance frequencies, the approaches developed for the theory of plates and shells are applied [12, 13]. The works, analyzed and generalized in [13], present the research results for flat isotropic and anisotropic plates of different shape, in particular for rectangular [14, 15], round and elliptical [16–19] ones, including those with different boundary conditions. The theory of vibrations of plates and shells [12, 13] in different recording variants is widely used in the field of nondestructive testing and technical diagnostics [20–24]. In [9–11], in particular, the formulas for

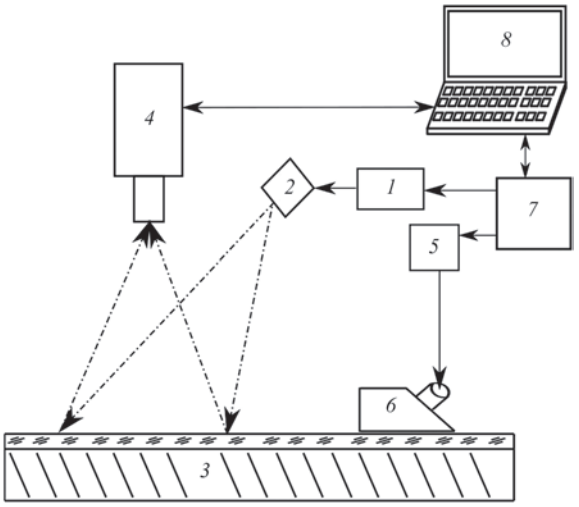

Figure 1. Simplified optical schematic of OAS layout: *1* — semiconductor laser with amplitude modulation; *2* — laser beam expander; *3* — fiberglass laminated structure, containing layers of STEF-1 glass textolite and subsurface defects in the middle layer; *4* — digital camera with a lens; *5* — broadband signal generator for piezoelectric converter; *6* — piezoelectric converter; *7* — control unit; *8* — computer

the model of a square subsurface defect are used. According to this model, the region of interest above the planar defect can be regarded as a thin square membrane, clamped at the edges. If such a defect is excited in one of its resonance frequencies, i.e. in one of the resonance frequencies of the region of interest above the defect, then an optical spatial response from the defect will form at OAS output. For a circular planar subsurface defect, a model of a circular plate from an isotropic material clamped at the edges, can also be used, which can be regarded as the region of interest above the subsurface defect, the dimensions of which correspond to the defect dimensions. According to [13, 20], the formula for determination of fundamental frequency f_{01} of resonance vibration of such a plate has the following form:

$$f_{01} = 0.47 \frac{h}{a^2} \sqrt{\frac{E}{\rho(1-\nu^2)}}, \quad (2)$$

where a is the membrane radius, mm; h is the depth of defect occurrence, mm; E is the Young's modulus, GPa; ρ is the material density, kg/m^3; ν is the Poisson's ratio.

EXPERIMENTAL STUDIES

Experimental studies on detection and identification of subsurface circular planar defects were conducted on samples of fiberglass laminated structures of 400×250 mm size, each of which was produced from three plates of STEF-1 glass textolite and epoxy phenolic polymer resin as a binder [10]. The lower layer, a 5 mm plate from STEF-1 glass textolite provided the structure rigidity. A series of circular and square

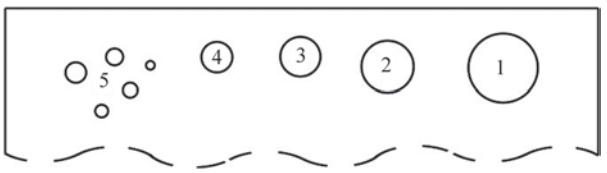

Figure 2. Schematic of arrangement of circular subsurface defects in the detected section of sample No. 1 of the fiberglass laminated structure and their diameters, mm: 1 — 45; 2 — 35; 3 — 25; 4 — 20; 5 — a group of five defects with diameters of 14, 12, 10, 8, 6 mm

holes were cut out in the middle layer, in 1.5 mm glass textolite plate. Made from the same material upper layers in the samples have different thickness. In sample No. 1 from fiberglass laminated structure, which was studied, the upper layer is 0.41 mm thick, i.e. the depth of defect occurrence in this sample is $h = 0.41$ mm. Figure 2 shows the scheme of arrangement of circular subsurface defects in the highlighted section of sample No. 1 with the thickness of upper glass textolite plate $h = 0.41$ mm, numbered from 1 to 5 in the order of decreasing defect diameters.

The developed OAS layout implements a method of quick real-time testing of the studied surface. For this purpose, after setting all the required parameters of the system, we analyze the difference DSP in a wide range of variation of the frequency of the sample excitation by an elastic wave. Each difference DSP is analyzed pixel by pixel for exceeding a certain preset noise level (NL) and under the condition of its exceeding in a certain image pixel, we record this event with a counter. After such verification we obtain M pixels with excess noise level for each difference DSP and for each preset excitation frequency. Further on we will divide this number by the total number of pixels in the image, and as a result we obtain the percentage of the area of optical spatial response from the region of interest, which exceeds the noise level, and, thus, can contain the subsurface defect. During this procedure, the difference DSP is saved for each excitation frequency, in case of exceeding the NL. Derived difference DSP is further on analyzed and processed using the simplest algorithms for digital image processing (DIP).

During NDT of sample No. 1 the difference DSP of the sample surface were obtained using OAS layout and optical spatial responses from defects No. 1–4 were analyzed in the range of variation of piezoelectric converter frequency of 1–50 kHz. Figure 3 shows the difference DSPs after application of DIP procedure, where optical responses from circular defects of different diameters are clearly visible.

Analysis of the images in Figure 3 allows following the correlation of the optical response areas and the respective defect areas, the area of responses from defects becoming smaller with reduction of their sizes. So, for instance, Figure 3, *a* gives an optical response from subsurface defect No. 1, 45 mm in diameter at resonance frequency $f_{01} = 1.8$ kHz. Figure 3, *b* shows the optical response from defect No. 2, 35 mm in diameter at resonance frequency $f_{01} = 2.8$ kHz. However, response from circular defect No. 3 (Figure 3, *c*) at resonance frequency $f_{01} = 4.6$ kHz is much smaller than its diameter, which is attributable to a too weak response from the sample surface, caused by a considerable distance between the excitation source and this defect. Therefore, to obtain defect map from the rest of test defects, the excitation source was moved closer to their location. Figure 3, *d* shows the optical response from a defect 20 mm in diameter at resonance frequency $f_{01} = 7.6$ kHz, the size of which is also smaller than the defect size. Despite the absence of the possibility of accurate determination of the radius of circular subsurface defect, evaluation of its size is satisfactory and sufficient for NDT objectives. Figure 4 gives improved defect maps for defect group No. 5. Figure 4, *a*, *b*, *c* shows the sample surface area where four of five defects of group No. 5 are concentrated, including the largest defect 14 mm in diameter (Figure 4, *a*) obtained at resonance frequency $f_{01} = 13.8$ kHz. The smallest defect 6 mm in diameter from defect group No. 5 could not be seen in the studied frequency range. In Figure 4, *b* we can simultaneously see defects 12, 10 and 8 mm in diameter at resonance frequency $f_{01} = 21.6$ kHz. At this frequency the largest response is formed by a defect 12 mm in diameter. Figure 4, *c* shows the optical response from a defect 8 mm in diameter at frequency $f_{01} = 35.8$ kHz.

Figure 5 presents the theoretical (curve *1*) and experimental (curve *2*) curves of the dependence of resonance frequency f_{01} on the sizes of subsurface defects in sample No. 1. The numbers mark the experimental data obtained for circular defects numbered in Figure 2. To derive a theoretical dependence (curve *1*) formula (*2*) was used, where the parameter

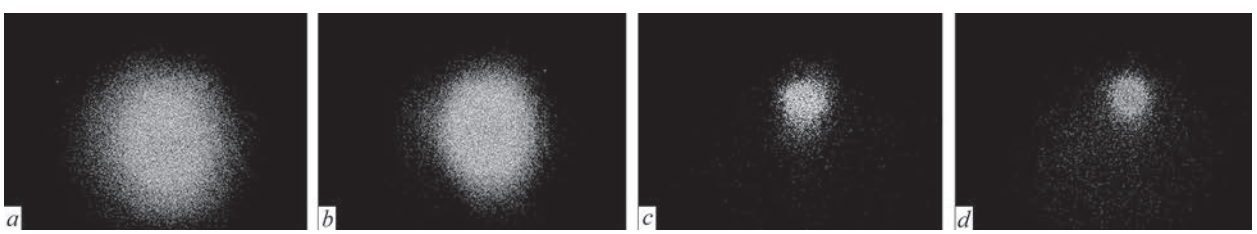

Figure 3. Optical spatial responses from subsurface defects No. 1 — 45 mm in diameter (*a*), No. 2 — 35 (*b*), No. 3 — 25 (*c*), No. 4 — 20 (*d*), which became visible in defect maps

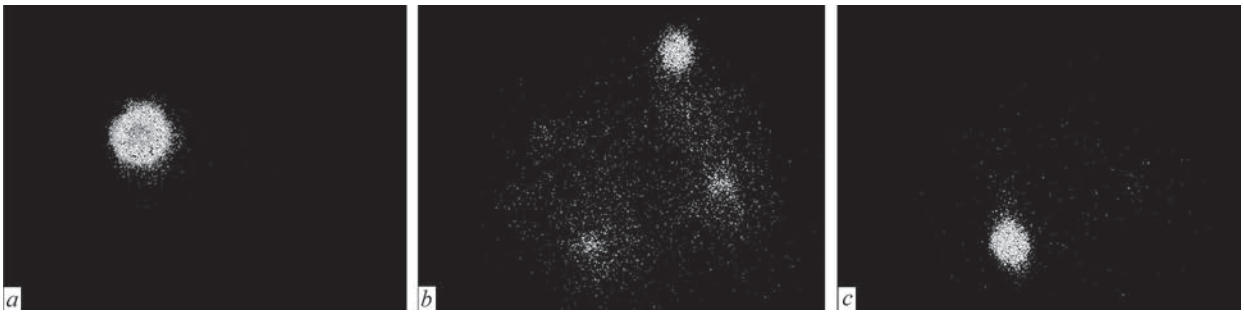

Figure 4. Defect maps of subsurface defect group No. 5 (Figure 2), recorded at the highest intensity of optical responses from defects with diameters of 14 (*a*), 12 (*b*), 8 mm (*c*)

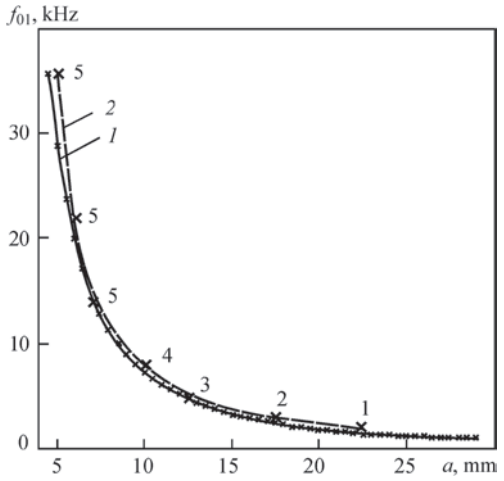

Figure 5. Theoretical (*1*) and experimental (*2*) dependencies of resonance frequency f_{01} on circular defect radius *a*

values were taken from [10] based on experimental data for STEF-1 glass textolite plate. Here the depth of defect occurrence h = 0.41 mm, modulus of elasticity E = 23.3±1.3 GPa, Poisson's ratio ν = 0.14±0.02 and material density ρ = (1.7±0.05)·10^3 kg/m^3.

As shown by the derived dependencies, the best convergence between them is observed for circular defect radius in the range of 6–18 mm, which corresponds to subsurface defects Nos 2–5.

Despite that, research results are indicative of the applicability of formula (2) to determine the depth of defect occurrence with sufficient accuracy in the entire studied range. Deviation of experimental results from the theoretical ones shown in Figure 5, are attributable, in particular, to imperfection of formula (2) for determination of the main resonance frequency f_{01}, deviations in the dimensions of the introduced defects, material orthotropy, etc. One of the methods to improve the accuracy of establishing the parameters of a subsurface defect of unknown dimensions and depth of occurrence is determination of not just the fundamental resonance frequency f_{01}, but also higher order frequencies. Having experimentally determined these frequencies and using formula (2), as well as the respective coefficients for finding multiple resonance frequencies for an isotropic material, we can experimentally determine these resonance frequencies by the spatial structure of optical responses, and, thus, determine the depth of the defect occurrence at unchanged parameters of the composite plate surface layer. Note that for a circular subsurface defect, the spatial structure of optical responses at the fundamental and multiple resonance frequencies corresponds to the structure of the nodes and antinodes of a circular membrane of the same diameter, and that of the defect, at the same resonance frequencies.

Thus, the results of studying the circular subsurface defects using OAS layout and derived experimental dependence of resonance frequency f_{01} on defect radius *a* at depth of occurrence h = 0.41 mm testify to the fundamental possibility of evaluation of the subsurface defect area and its geometrical dimensions.

CONCLUSIONS

Based on the developed OAM, OAS layout was created, which enables detection of subsurface defects in composite laminated structures using a series of dynamic speckle patterns of the composite layer surface above the defect, excited by a flexural elastic wave. After their recording, difference DSP are formed and optical spatial responses from the defects are detected in case of their presence in the digital camera field of view. Formation of dynamic speckle patterns does not require application of an additional reference beam in OAS, which enables designing on its base high-speed optical-digital devices for NDT of subsurface defects, with a low sensitivity to vibrations or other external factors and which are capable of operation in site. It is shown that difference DSP derived at fundamental resonance frequencies f_{01} for circular subsurface defects, allow detecting these defects in fiberglass laminated structures and determining their sizes with diameters in the range of 8–45 mm.

REFERENCES

1. Newman, J.W. (2012) *Laser testing: Shearography & Holography*. Ed. by P.O. Moore. The Nondestructive Testing Overview, Columbus Ohio, American Society for Nondestructive Testing.
2. Lobanov, L.M., Pivtorak, V.A. (2014) Diagnostics of structures by the methods of electron shearography and speckle-interferometry. *Materials Sci.*, **49**, 442–448. DOI: https://doi.org/10.1007/s11003-014-9635-5
3. Howell, P.A. (2020) *Nondestructive evaluation (NDE) Methods and capabilities:* Handbook, NASA/TM−2020-220568, Vol I. Langley Research Center, Hampton, VA, USA.

4. Nazarchuk, Z, Muravsky, L., Kuryliak, D. (2023) Digital speckle pattern interferometry for studying surface deformation and fracture of materials. In*: Optical Metrology and Optoacoustics in Nondestructive Evaluation of Materials*. Springer Series in Optical Sciences, **242**. Singapore: Springer, 149–217. DOI: https://doi.org/10.1007/978-981-99-1226-1_4
5. Chatters, T., Pouet, B., Krishnaswamy, S. (1992) *Shearography with synchronized pressure stressing*. Eds by D.O. Thompson, D.E. Chimenti, Review of Progress in Quantitative NDE, La Jolla, CA, Plenum Press, 426. DOI: https://doi.org/10.1007/978-1-4615-2848-7_54
6. Hung, Y.Y., Yang, L.X., Huang, Y.H. (2013) Nondestructive evaluation (NDE) of composites: Digital shearography. Ed. by V.M. Karbhari, In: *Nondestructive evaluation (NDE) of polymer matrix composites*. Cambridge, Philadelphia, New Delhi: Woodhead Publishing Limited, 84–115.
7. Muravsky, L., Kuts, O., Gaskevych, G., Suriadova, O. (2019) Detection of subsurface defects in composite panels using dynamic speckle patterns. In: *Proc. of IEEE XIth Inter. Scientific and Practical Conf. on Electronics and Information Technologies, 2019*, 7–10. DOI: https://doi. org/10.1109E/LIT.2019.8892294
8. Nazarchuk, Z., Muravsky, L., Kuryliak, D. (2019) To the problem of the subsurface defects detection: Theory and experiment. *Procedia Structural Integrity*, **16**, 11–18. DOI: https://doi.org/10.1016/j.prostr.2019.07.016
9. Nazarchuk, Z.T., Muravsky, L.I., Kuts, O.G. (2022) Nondestructive testing of thin composite structures for subsurface defects detection using dynamic laser speckles. *Research in Nondestructive Evaluation,* **33**, 59–77. DOI: https://doi.org/10.1080/09349847.2022.2049407
10. Muravsky, L., Nazarchuk, Z., Kuts, O., Sharabura, O. (2023) Identification of internal planar square defects in composite panels using optoacoustic technique. In*: Proc. of IEEE 13th Inter. Conf. on Electronics and Information Technologies, ELIT 2023*, 265–269. DOI: https://doi. org/10.1109/ELIT61488.2023.10310846
11. Nazarchuk, Z., Muravsky, L., Kuryliak, D. (2023) Methods for processing and analyzing the speckle patterns of materials surfaces. In*: Optical metrology and optoacoustics in nondestructive evaluation of materials*. Springer Series in Optical Sci., **242**. Singapore: Springer, 249–323. DOI: https://doi.org/10.1007/978-981-99-1226-1_6
12. Timoshenko, S.P., Woinowsky-Krieger, S. (1959) *Theory of plates and shells*. 2nd Ed., McGraw-Hill, New York.
13. Leissa, A.W. (1969) *Vibration of plates*. Scientific and Technical Information Division, National Aeronautics and Space Administration.
14. Li, W.L. (2004) Vibration analysis of rectangular plates with general elastic boundary supports. *J. of Sound and Vibration*, 273(**3**), 619–635. DOI: https://doi.org/10.1016/S0022-460X(03)00562-5
15. Guguloth, G.N., Singh, B.N., Ranjan, V. (2019) Free vibration analysis of simply supported rectangular plates. *Vibroengineering Procedia*, **29**, 270–273. DOI: https://doi.org/10.21595/vp.2019.21135
16. Chakraverty, S., Jindal, R. Agarwal, V.K. (2007) Effect of non-homogeneity on natural frequencies of vibration of elliptic plates. *Meccanica,* **42**, 585–599. DOI: https://doi.org/10.1007/s11012-007-9077-3
17. Maiz, S., Rossit, C.A., Bambill, D.V., Susca, A. (2009) Transverse vibrations of a clamped elliptical plate carrying a concentrated mass at an arbitrary position. *J. of Sound and Vibration*, 320(**4–5**), 1146–1163. DOI: https://doi. org/10.1016/j.jsv.2008.09.013
18. Zhou, Z.H., Wong, K.W., Xu, X.S., Leung, A.Y.T. (2011) Natural vibration of circular and annular thin plates by Hamiltonian approach. *J. of Sound and Vibration*, 330(**5**), 1005–1017. DOI: https://doi.org/10.1016/j.jsv.2010.09.015
19. Anjomshoa, A., Tahani, M. (2016) Vibration analysis of orthotropic circular and elliptical nano-plates embedded in elastic medium based on nonlocal Mindlin plate theory and using Galerkin method. *J. of Mechanical Sci. and Technology*, **30**, 2463–2474. DOI: https://doi.org/10.1007/ s12206-016-0506-x
20. Cawley, P. (1984) The impedance method of nondestructive inspection. *NDT Inter.*, **17**(2), 59–65. DOI: https:// doi.org/10.1016/0308-9126(84)90045-2
21. Cawley, P., Theodorakopoulos, C. (1989) The membrane resonance method of nondestructive testing. *J. of Sound and Vibration*, 130(**2**), 299–311. DOI: https://doi. org/10.1016/0022-460X(89)90555-5
22. Ma, C.C., Huang, C.H. (2004) Experimental whole-field interferometry for transverse vibration of plates. *J. of Sound and Vibration,* 271(**3–5**), 493–506. DOI: https://doi. org/10.1016/S0022-460X(03)00276-1
23. Bruno, F., Laurent, J., Prada, C. et al. (2014) Nondestructive testing of composite plates by holographic vibrometry. *J. of Applied Physics*, 115(**15**), 154503. DOI: https://dx.doi.org/10.1063/1.4871178
24. Lamboul, B., Giraudo, O., Osmont, D. (2015) Detection of disbonds in foam composite assemblies using flexural waves and shearography. In: *AIP Conf. Proceedings,* 1650(**1**), 1155–1161. DOI: http://dx.doi.org/10.1063/1.4914725

ORCID
O.M. Sharabura: 0000-0002-5712-4114,
L.I. Muravsky: 0000-0001-8839-2819

CONFLICT OF INTEREST
The Authors declare no conflict of interest

CORRESPONDING AUTHOR
L.I. Muravsky
G.V. Karpenko Physico-Mechanical Institute of the NASU
5 Naukova Str., 79060, Lviv, Ukraine.
E-mail: muravskyleon@gmail.com

SUGGESTED CITATION
O.M. Sharabura, L.I. Muravsky, O.G. Kuts (2025) Detection of circular subsurface defects in laminated composites using optical-acoustic nondestructive testing system. *The Paton Welding J.*, **2**, 42–46. DOI: https://doi.org/10.37434/tpwj2025.02.07

JOURNAL HOME PAGE
https://patonpublishinghouse.com/eng/journals/tpwj

Received: 24.10.2024
Received in revised form: 14.11.2024
Accepted: 31.03.2025

50 YEARS OF THE ARAKS EXPERIMENT: PROBING THE EARTH'S IONOSPHERE AND MAGNETOSPHERE WITH A POWERFUL ELECTRON BEAM

The early 1970s marked the beginning of active space exploration, highlighted by the successful implementation of several international research projects. These initiatives became possible during a brief period of détente in global tensions. Agreements between the USSR and the USA facilitated scientific and technical cooperation between the two opposing blocs, particularly in the field of space research. The signing of treaties limiting anti-ballistic missile systems and strategic armaments created opportunities for joint experiments in the peaceful exploration of space. Among the most notable was the historic Soviet-American "Soyuz-Apollo" mission, which involved docking and a joint manned flight of spacecraft from both superpowers. Another significant project was the Soviet-French (with USA participation) ARAKS experiment, dedicated to studying physical processes in the Earth's ionosphere, especially those associated with auroral phenomena [1–4].

The ARAKS experiment (Artificial Radiation and Aurora at Kergelen and Sogra) pursued both scientific and practical objectives. Scientifically, it aimed to investigate the interaction of high-energy particles with the Earth's magnetic field and atmosphere, test theoretical plasma physics models, and validate hypotheses. On the practical side, the experiment sought to refine the design of powerful energy sources, systems of control, automation, and data collection under extreme space conditions. Additionally, it enabled full scale studies of supersonic flow of the Earth's rarefied ionospheric plasma around a spacecraft and the electrification of spacecraft surfaces to high potentials, which could interfere with or even damage onboard electronic equipment. A particularly intriguing aspect of the experiment was its aesthetic component, as its name suggested — the artificial creation of auroras.

The core of the experiment involved injecting an electron beam, generated by an electron beam gun (betatron), into the Earth's magnetosphere to study the dynamics of electron movement within the Earth's magnetic field and their interactions with the ionosphere. Unlike passive methods, which observe natural phenomena independent of the researcher, this experiment represented an active space study. It entailed directed intervention in the research object with controlled parameters, followed by analysis of the results, similar to experiments conducted in terrestrial laboratories. Despite numerous laboratory and passive experiments in this field, active experiments remain relatively rare in global scientific practice. Since October 1974, a series of American active experiments, such as EXCEDE [5], Echo [6–8], Spacelab 1 (1983) [9], Atlas-1 (1992) [10, 11], and Beam-PIE (2023) [12], as well as the US-Japanese Charge-2 (1985) [13] and SEPAC [14] experiments et al., have been conducted.

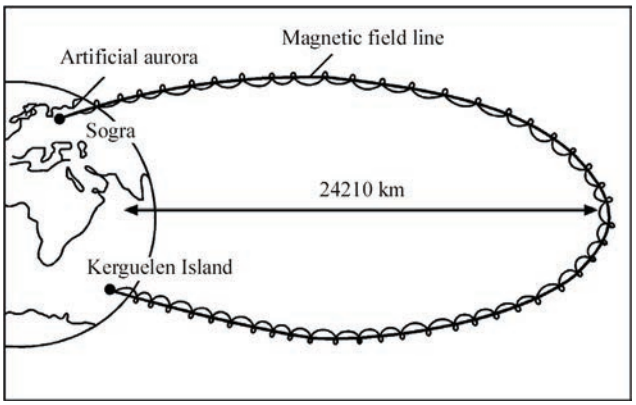

The active experiment ARAKS was, in fact, the first such successful study (January–February 1975) with technical characteristics of onboard equipment that were practically replicated only half a century later. The initiators of the project were Dr. I.O. Zhulyn (Institute of Terrestrial Magnetism and Atmospheric Wave Propagation, USSR) and Prof. F. Cambou (Center for the Study of Radiation in Space (CESR), Toulouse, France). The main scientific institutions involved in the project were: in France — the National Center for Space Studies (CNES), Toulouse; the Center for the Study of Radiation (CESR), Toulouse; the Ionosphere Research Group (GRI), Saint-Maurdes-Fossés; in the USSR — the Institute of Space Research, Moscow; the Institute of Terrestrial Magnetism and Atmospheric Wave Propagation, Moscow; the E.O. Paton Electric Welding Institute of the Academy of Sciences of the Ukrainian SSR, Kyiv;

the Institute of Electrodynamics of the Academy of Sciences of the Ukrainian SSR, Kyiv; the Kurchatov Institute of Atomic Energy, Moscow. The abbreviation ARAKS is phonetically similar to the name of the Araks River in Armenia, where the agreement to conduct this experiment was first reached.

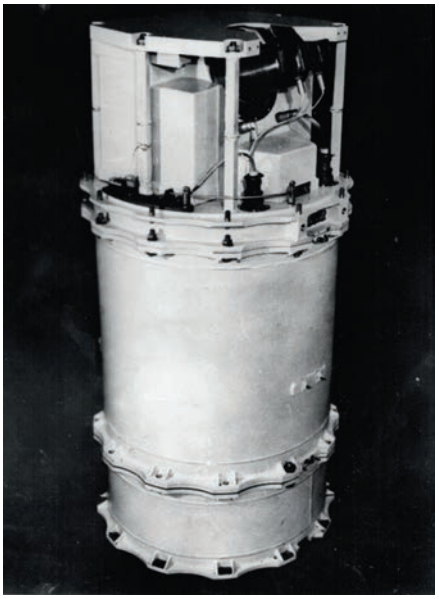

According to the experiment plan, it was necessary to select a pair of magnetically conjugate points, launch a rocket along a ballistic trajectory, generate a beta-particle (electron) beam at one of the points, and record the expected physical effects using ground-based, airborne, and space-based instruments.

As magnetically conjugate points on land, a unique pair was chosen — on Kerguelen Island (France, Southern part of the Indian Ocean) and near the settlement of Sogra (Arkhangelsk Region, USSR). Both points were located on land and positioned at high latitudes in different hemispheres, separated by a distance of more than 12600 km.

The electron beam, generated by an accelerator in the Kerguelen area, was expected to propagate along the magnetic field line northward, and upon entering the dense atmospheric layers in the Arkhangelsk region, act as a "disturbance" in the environment. Part of the plasma, reflected in the Northern Hemisphere, was supposed to return to the launch site, practically retracing its initial trajectory.

The launch of the experimental equipment was carried out using the French "Eridan" rocket, whose final stage contained two interacting experimental systems: an electron beam gun, devices for indirect potential change, particle flux detectors, and a detachable cone that was ejected at a speed of 40 m/s from the rocket's main body. This cone housed antennas designed to detect radio waves generated by the electron beam as it interacted with the ionosphere.

Ground-based measurement stations were established for the experiment. Optical and radar measurements in the Northern Hemisphere at the magnetically conjugate point to Kerguelen Island, as well as extremely low and extremely high-frequency measurements at both locations, were of particular importance. Additionally, just before the launch of the "Eridan" rocket, X-ray detectors were deployed by parachute at an altitude of ~80 km above Kerguelen Island. These detectors had been delivered there by the "Areas" rocket. The X-ray experiment was conducted by the University of Houston (USA).

The experience in developing electron beam equipment placed on rockets and satellites allowed the E.O. Paton Electric Welding Institute (PWI) and the Institute of Electrodynamics (IED) to create an electron accelerator for ARAKS with record-breaking characteristics. The project curator at PWI was D.A. Dudko. The main leadership for specific research directions was carried out by: O.K. Nazarenko — electron beam gun; V. D. Shelyagin — high-voltage power source; Yu.M. Lankin — electronics and automation; V.E. Paton — structural design.

According to its main technological parameters, the accelerator (betatron) of the ARAKS apparatus was analogous to one of the best industrial electron beam welding systems of that time — the U-250A with the U-530 gun. It provided a beam power of 15 kW, operated in a pulsed mode, and allowed electron beam deflection at angles of up to ±90°. The size and weight characteristics and reliability of the accelerator exceeded those of any known ground-based equipment at that time. For instance, the weight of the ARAKS accelerator, excluding the battery, was 120 kg, and its volume was 0.2 m^3, which was 17 times lighter and 20 times more compact than the U-250A, which was built using electron tubes.

This achievement was made possible thanks to the high level of expertise of the employees of the PWI and their experience in developing and practically utilizing high-power electron beam equipment and technologies in studies of vacuum welding, remelting, surfacing, and other processes [15, 16]. Notably, the "Vulkan" welding system was successfully tested in space during the world's first space welding experiment aboard the "Soyuz-6" spacecraft on October 16, 1969. In the ARAKS experiment, a specially developed high-power inverter transistor power supply for the electron beam gun was used, along with a high-voltage sectional rectifier on semiconductor diodes and control and automatic regulation systems based on transistors and integrated circuits, which had just begun to emerge at that time.

Moreover, the ARAKS accelerator met all the requirements for space equipment, including operational temperature range, vibration and shock resistance, level of generated radio interference, reliability, and more, as confirmed by numerous ground-based tests conducted in the USSR and France.

The ARAKS accelerator, created in the early 1970s, was far ahead of its time. Inverter power supplies on transistors with similar characteristics for electron beam welding only appeared at the very beginning of the new millennium. For space applications, however, accelerators with similar characteristics were successfully developed only in 2023, for example, within the Beam-PIE project.

After completing all ground tests in October 1974, part of the Soviet expedition under the ARAKS program departed by plane from Moscow, with stops in Dar es Salaam (Tanzania), Antananarivo (Madagascar), and Saint-Denis (Réunion, France). From there, together with members of the French expedition who joined them, they set sail on October 30 aboard the "Anichkov" motor ship, which carried all the scientific equipment. They arrived on Kerguelen Island on November 4.

The expedition team included employees of the PWI Yu.M. Lankin, Ye.M. Baishtruk, V.K. Mokhnach, and Yu.V. Neporozhniy, as well as employee IED, H.F. Pazeyev. It is important to note that the distance to Kerguelen Island from the nearest continental landmass (Antarctica) is about two thousand kilometers, while the distance from the African continent exceeds three thousand kilometers.

Such remoteness and the availability of only sea transportation imposed strict requirements on organizational aspects, equipment reliability, and demanded thorough and meticulously planned expedition logistics, along with well-coordinated actions of all team members.

Three months were spent on the installation, assembly, adjustment, and testing of the entire ARAKS equipment complex. Finally, on January 26, 1975, when favorable weather conditions simultaneously formed over Kerguelen Island and the Arkhangelsk region, the first launch of the "Eridan" rocket under the ARAKS program took place.

The responsibility for synchronizing all hardware components of the experiment, both onboard and ground-based, which were located in different hemispheres of our planet, as well as issuing the rocket launch command, was entrusted to Yu.M. Lankin. The rocket traveled north along the magnetic meridian in a ballistic trajectory, reaching an altitude of approximately 200 km. The electron beam gun injected a time-modulated by a complex program current (0.5 A) of high energy (15 and 27 kV) into the magnetosphere at various angles relative to the rocket's axis (–70°, 0°, +70°). The nose cone separated at a significant distance (~10 km) ahead of the rocket. It was equipped with radio receivers and frequency switches ranging from 0 to 5 MHz to study emissions resulting from the interaction of the electron beam with the ionosphere. Optical and radar observations of the electron beam were conducted at the magnetically conjugate point in the Arkhangelsk region.

The second launch took place on February 15, 1975. Unlike the first, this launch was conducted eastward, with the electron beam deflected at angles of –30°, 0°, and +70° relative to the rocket axis.

The electron injector functioned according to the full program and, as the primary scientific instrument on board, was largely responsible for the overall success of the experiment. The electron beam, injected from Kerguelen Island, traveled over 10000 km and induced an artificial aurora in the magnetically conjugate point in the Arkhangelsk region, which was recorded by radar. Microwave radio emissions were detected as a result of the interaction of the electron beam with the ionospheric plasma. Additionally, the beam was intercepted after being magnetically reflected from the conjugate point, as well as from the atmosphere when injected downward toward Earth.

The analysis of telemetry data confirmed that both launches of the "Eridan" rocket were successful. All Soviet and most French instruments operated normally and fulfilled their planned objectives.

The ARAKS project made an outstanding contribution to plasma physics (the emergence of plasma instability in an unbounded space induced by an electron beam) as well as to geophysics (geomagnetic field topography, etc.). Valuable scientific information was obtained regarding the injection processes, the interaction of the injected beam with the environment, and the behavior of a cesium plasma jet, which was intended to compensate for the positive charge of the

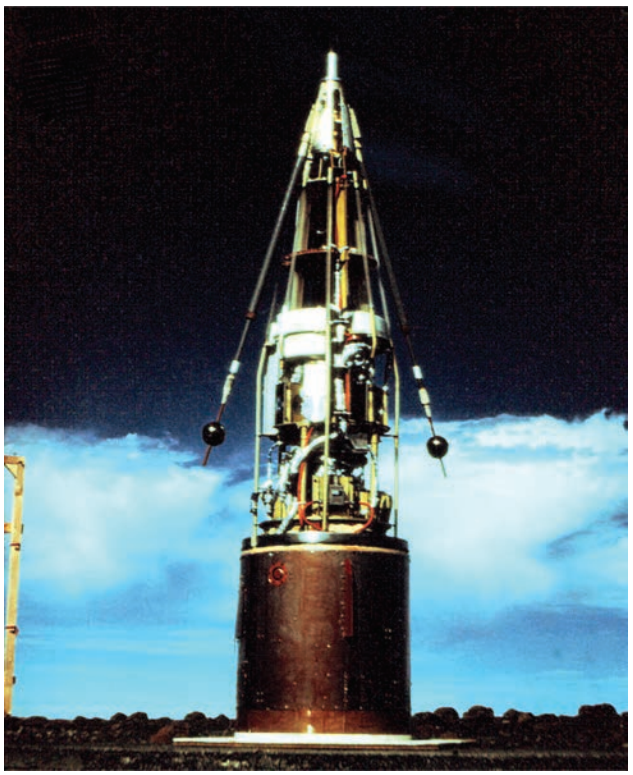

rocket body arising from the deflection of high-energy electrons from the accelerator.

Moreover, new effects were discovered that had not been previously anticipated. In particular, intriguing data were obtained on the occurrence and development of plasma instabilities — processes of fundamental interest for the study of controlled thermonuclear reactions.

From a practical standpoint, understanding the physics of wave-particle interactions may soon lead to highly significant, albeit somewhat unconventional, applications, such as earthquake prediction and the restoration of radiation belts for biosphere protection.

REFERENCES

1. (2003) *Space: Technologies, materials, structures*. Ed. by B.E. Paton. New York, Taylor & Francis Group.
2. Gendrin, R. (1974) The French-Soviet "ARAKS" experiment. *Space Sci. Rev.*, **15**, 905–931. DOI: https://doi.org/10.1007/BF00241068
3. Cambou, F., Lavergnat, J., Migulin, V.V. et al. (1978) ARAKS — Controlled or puzzling experiment? *Nature*, **271**, 723–726. DOI: https://doi.org/10.1038/271723a0
4. Cambou, F., Dokoukine, V.S., Lavergnat, J. et al. (1980) General description of the ARAKS experiments. *Ann. Geophys*., **36**, 271–284.
5. McNutt, R.L.Jr., Rieder, R.J., Keneshea, T.J. et al. (1995) Energy deposition in the upper atmosphere in the EXCEDE III experiment. *Advanced Space Research*, 15(**12**), 13–16. DOI: https://doi.org/10.1016/0273-1177(95)00002-V
6. Hendrickson, R.A., McEntire, R.W., Winckler, J.R. (1975) Echo 1: An experimental analysis of local effects and conjugate return echoes from an electron beam injected into the magnetosphere by a sounding rocket. *Planet. Space Sci.*, **23**, 1431. DOI: https://doi.org/10.1016/0032-0633(75)90039-2
7. Winckler, J.R., Arnoldy, R.L., Hendrickson, R.A. (1975) Echo II: A study of electron beams injected into a high-latitude ionosphere from a large sounding rocket. *J. Geophys. Res.*, **80**, 2083–2088. DOI: https://doi.org/10.1029/JA080i016p02083
8. Hendrickson, R.A., Winckler, J.R., Arnoldy, R.L. (1976) Echo III: The study of electric and magnetic fields with conjugate echoes from artificial electron beams injected into the auroral zone ionosphere. *Geophysical Research Letters*, **3**, 409–412. DOI: https://doi.org/10.1029/GL003i007p00409
9. Sasaki, S., Kawashima, N., Kuriki, K. et al. (1986) Vehicle charging observed in SEPAC Spacelab-1 experiment. *J. Spacecraft Rockets*, **23**, 194–199. DOI: https://doi.org/10.2514/3.25801
10. Burch, J.L., Mende, S.B. et al. (1993) Artificial Auroras in the upper atmosphere: 1. Electron beam injections. *Geophysical Research Letters,* 20(**6**)*,* 491–494. DOI: https://doi.org/10.1029/93GL00595
11. Mende, S.B., Burch, J.L. et al. (1993) Artificial Auroras in the upper atmosphere: 2. Imaging results. *Geophysical Research Letters,* 20(**6**)*,* 495–498. DOI: https://doi.org/10.1029/93GL00594
12. Reeves, G.D., Delzanno, G.L. et al. (2020) The beam plasma interactions experiment: An active experiment using pulsed electron beams. *Front. Astron. Space Sci.*, **7:23**. DOI: https://doi.org/10.3389/fspas.2020.00023
13. Sasaki, S., Oyama, K.I., Kawashima, N., Obayashi, T. et al. (1988) Tethered rocket experiment (CHARGE-2) initial results on electrodynamics. *Radio Sci.*, **23**, 975–988. DOI: https://doi.org/10.1029/RS023i006p00975
14. Obayashi, T. et al. (1982) Space Experiments with Particle Accelerators (SEPAC). Ed. by B. Grandal, In: Artificial Particle Beams in Space Plasma Studies. NATO Advanced Study Institutes Series, Vol. 79. Springer, Boston, MA. DOI: https://doi.org/10.1007/978-1-4684-4223-6_44.
15. Nazarenko, O.K. (1965) *Electron beam welding.* Kyiv, Naukova Dumka.
16. Paton, B.E., Nazarenko, O.K. et al. (1971) Specific features of the equipment and processes of electron beam welding and cutting under space conditions. *Avtomaticheskaya Svarka,* **3**, 3–8.

Dr. of Tech. Sci. Degr. Yurii Lankin,
Participant of the Experiment